THE EFFECT OF SURFACE ROUGHNESS ON EROSION YIELDS AND DISTRIBUTION OF IMPURITIES ON FUSION RELEVANT MATERIALS

Mitja Kelemen, mag. fiz.

Doctoral Dissertation
Jožef Stefan International Postgraduate School
Ljubljana, Slovenia

Supervisor: Asst. Prof. Dr. Sabina Markelj, IPS and Jožef Stefan Institute, Ljubljana, Slovenia
Co-Supervisor: Prof. Dr. Primož Pelicon, IPS and Jožef Stefan Institute, Ljubljana, Slovenia

Evaluation Board:
Assoc. Prof. Dr. Miha Čekada , Chair, IPS and Jožef Stefan Institute, Ljubljana, Slovenia
Prof. Dr. Janez Kovač, Member, IPS and Jožef Stefan Institute, Ljubljana, Slovenia
Dr. Ivančica Bogdanović Radović, Member, Laboratory for Ion Beam Interactions, Ruđer Bošković Institute, Zagreb, Croatia

MEDNARODNA PODIPLOMSKA ŠOLA JOŽEFA STEFANA
JOŽEF STEFAN INTERNATIONAL POSTGRADUATE SCHOOL

Mitja Kelemen, mag. fiz.

THE EFFECT OF SURFACE ROUGHNESS ON EROSION YIELDS AND DISTRIBUTION OF IMPURITIES ON FUSION RELEVANT MATERIALS

Doctoral Dissertation

VPLIV POVRŠINSKE HRAPAVOSTI NA EROZIJO IN PORAZDELITVE NEČISTOČ NA MATERIALIH, PRIMERNIH ZA FUZIJO

Doktorska disertacija

Supervisor: Asst. Prof. Dr. Sabina Markelj

Co-Supervisor: Prof. Dr. Primož Pelicon

Ljubljana, Slovenia, January 2023

To all the teachers . . .

Acknowledgments

This thesis would not have been possible without the help of many people. I would first like to thank my supervisors, Dr. Sabina Markelj and Dr. Primož Pelicon. I have always been able to count on their support, and their assistance with this work. Thanks also go to the other colleagues from Jožef Stefan Institute who helped in the creation of this work. To Dr. Rok Zaplotnik who helped with AFM analysis and Dr. Primož Vavpetič for his help with the ion beams.

Thanks also go to Thomas Schwartz-Selinge, Martin Balden and Karl Krieger from Max Planck Institute for Plasma Physic in Garching, Germany. Who helped with sample substrate preparation and analysis, and also with the communication and help with the ASDEX Upgrade experiment. Extended thanks goes also to the ASDEX Upgrade team for performing the experiment.

None of this would be possible without excellent substrate preparation and molybdenum coating manufacturing. Here the thanks goes to Espedito Vassallo from Istituto per la Scienza e Tecnologia dei Plasmi, Milano, Italy, and Matteo Passoni and David Dellasega from Politecnico di Milano.

Special thanks goes also to Andreas Mutzke, for his guidance in using SDTrimSP coad and also performing SDTrimSP 3D calculations.

I would also like to thank to Antti Hakola from VTT Technical Research Centre of Finland and Sebastian Brezinsek from Forschungszentrum Jülich, for their involvement in coordinating the sample analysis from different ASDEX Upgrade experiments used in this work.

This work has been carried out within the framework of the EUROfusion Consortium and has received funding from the Euroatom research and training programme 2014–2018 and 2019–2020 under grant agreement No 633053. Work was performed under EUROfusion WP PFC. In addition acknowledgement is given to the the Slovenian Research Agency (research core funding No. P2–0405).

Thanks also go to the three wizards in the background prof. dr. Alojzij Franc Kodre, Tamara Németh and Tjaša Knez who helped with the final appearance of this dissertation.

Lastly, I would like to thank my friends, family, and other colleagues for their unrelenting encouragement, support and patience for which I am incredibly grateful.

Abstract

Plasma facing components (PFC) in fusion devices are exposed to plasma. Plasma-wall interaction processes are important as they impose a series of constraints on the components. The lifetime of the PFCs is dominantly determined by two processes: erosion and fuel retention. At the first wall the erosion is caused by physical sputtering due to bombardment with energetic particles (in keV range) originating from the core plasma. In numerous studies in the past it was shown that surface roughness of the target and an angle of incidence of the particle affects the rate of sputtering or sputter yield. However, not many of studies have been done for fusion relevant conditions. To this end we built Low Energy Ion Sputtering Apparatus - LEISA at Jožef Stefan Institute. In LEISA we can produce particle fluxes up to 8×10^{18} $\mathrm{Dm^{-2}s^{-1}}$ with the energies up to 5 keV. The samples inside LEISA can be rotated from $0°$ to $90°$, to study the angular dependence of sputter yield. Graphite tiles with surface roughness ranging from $R_\mathrm{a} \approx 5$ nm up to $R_\mathrm{a} \approx 2$–3 µm with 115 nm thick molybdenum coating were exposed to 1 keV D ions in LEISA. They were exposed to D ion fluence ranging from 0.89 up to 3.19×10^{23} $\mathrm{Dm^{-2}s^{-1}}$ at the impact angles of $0°$, $40°$, $60°$ and $70°$. The surface roughneses were measured with atomic force microscope (AFM), confocal scanning laser microscope (CSLM) and scanning electron microscope (SEM). The Mo layer thickness was measured by Rutherford backscattering spectroscopy (RBS) before and after D ion exposure. From the measured eroded Mo thickness and applied the D ion fluence we calculated sputter yields for all angles and surface roughness. For all the surfaces a strong angular dependence of the sputter yield is observed. For smooth and intermediate surface roughnesses, up to $R_\mathrm{a} \approx 280$ nm, an increase of the sputter yield with the angle up to a factor of five compared to $0°$ is observed. In contrast, at the highest surface roughness in the 2–3 µm range the sputtering yield decreases with increasing impact angle.

Same types of samples were exposed in the divertor region of the ASDEX Upgrade-AUG tokamak, using the DIM-II manipulator. Samples were exposed to eight 6 s long L-MODE discharges in D plasma. The results obtained at the samples from AUG match well with the results obtained at the LEISA. At the AUG samples, we observed a similar trend, the decrease of the sputtering yield at high impact angles for the samples with higher surface roughness.

Sputter yields from LEISA experiment were compared with the simulations performed with the SDTrimSP 3D, a Monte Carlo simulation code taking as an input surface representation data. We achieved a good qualitative agreement with experimental results.

At the end we studied the effects of surface roughness on the fuel and impurities retention on the samples exposed in AUG. The investigation was performed with micro-beam utilising PIXE and NRA analytical techniques. The results show an intense retention in the samples with high surface rougness.

The lifetime of PFCs is an interplay of both the erosion and retention, and we demonstrated the important role of these two processes by the surface roughness. We are leaving the determination of the optimal surface roughness of the PFCs for the next studies.

Povzetek

Življenjski čas notranjih sten v fuzijskih reaktorjih omejuje intenzivna interakcija s plazmo. Pri tem sta še posebej pomembna procesa erozije in zadrževanja snovi iz plazme. Erozijo povzročajo ioni iz plazme s trki v steno, ki imajo energijo nekaj keV. Dosedanje študije so pokazale, da na razprševanje vplivata tako vpadni kot ionov iz plazme kot tudi površinska hrapavost. Žal so le nekaj študij razprševanja izvedli v fizikalnih razmerah, ki vladajo znotraj tokamakov. Da bi se poglobljeno posvetili procesu erozije v tokamakih, smo na Institutu »Jožef Stefan" zgradili nizkoenergijsko ionsko razprševalno napravo LEISA (Low Energy Ion Sputtering Apparatus). V tej napravi lahko dosežemo ionske tokove do 8×10^{18} $\mathrm{m}^{-2}\mathrm{s}^{-1}$ in energijo do 5 keV. Za študij kotne odvisnosti razprševalnega koeficienta lahko v aparaturi LEISA vrtimo vzorce z vpadnimi koti med 0° in 90°. Kot vzorce smo uporabili grafitne ploščice s površinskimi hrapavostmi od R_a 5 nm do $R_\mathrm{a} \approx 2$–3 µm, ki smo jih pokrili s 115 nm debelo plastjo molibdena ter jih izpostavili devterijevim ionom z energijo 1 keV. Vzorce smo izpostavili ionskim dozam od 0,89 do $3,19 \times 10^{23}$ $1/\mathrm{m}^2$ pri vpadnih kotih 0°, 40°, 60° in 70°. Hrapavost površin smo izmerili z mikroskopom na atomsko silo, konfokalnim laserskim mikroskopom in elektronskim vrstičnim mikroskopom. Debelino plasti molibdena smo izmerili s spektrometrijo povratno sipanih ionov (angl. Rutherford Backscattering Spectrometry, RBS). To nam je omogočilo izračun razprševalnih koeficientov za vse kombinacije površin in vpadnih kotov. Opazili smo močan vpliv hrapavosti na razprševanje. Pri majhnih vpadnih kotih smo opazili porast razprševanja z večanjem površinske hrapavosti. Pri večjih vpadnih kotih smo opazili nasprotno zvezo: velika površinska hrapavost je povzročila manjše razprševanje.

Vzorce enake strukture smo nadalje izpostavili plazmi v divertorskem delu fuzijske naprave ASDEX Upgrade (AUG), kjer smo uporabili manipulator DIM-II. Vzorci so bili izpostavljeni osmim razelektritvam devterijeve plazme s trajanjem po 6 sekund. Primerjava rezultatov iz naprav AUG in LEISA kaže na kvalitativno ujemanje opisanih pojavov. Tudi pri vzorcih iz naprave AUG smo namreč opazili manjšo erozijo na bolj hrapavih vzorcih pri velikih vpadnih kotih. Rezultate iz naprave LEISA smo primerjali s simulacijami, opravljenimi s programom SDTrimSP 3D, ki temelji na metodi Monte Carlo. Kot vhodni parameter lahko podamo meritve površinske strukture. S takim pristopom so uspeli dobiti dobro ujemanje med izračunanimi in izmerjenimi vrednostmi razpševalnega koeficienta za molibden.

Posvetili smo se tudi študiju vpliva površinske hrapavosti na zadrževanje nečistoč in fuzijskega goriva. Raziskava je bila izvedena na hrapavih vzorcih, izpostavljenih v napravi AUG. Za analizo smo uporabili fokusiran mikrožarek in metodi PIXE ter NRA. Rezultati so pokazali intenzivnejše zadrževanje na bolj hrapavih vzorcih.

Procesa erozije in zadrževanja sta najpomembnejša pri oceni življenjske dobe notranjih sten fuzijskih reaktorjev. Pokazali smo, da je intenzivnost obeh procesov močno odvisna od površinske hrapavosti. Ugotovitve so pomembne pri določanju optimalnih površin segmentov za notranje stene fuzijskih reaktorjev.

Contents

List of Figures

List of Tables

Chapter 1

Introduction

One of technological drives has been to harvest the energy of natural processes and use it to our advantage. Nowadays most of effort is directed to produce electrical energy. Conventional sources that can be converted into electricity are stretched to the limit. The need for new energy sources arises, among them fusion of light atomic nuclei. The process of nuclear fusion is an ongoing process in the core of stars and is one of the primary sources of energy in the universe [1], [2]. Inside the core of most stars the light nuclei of hydrogen, as the protons, are fused to form a heavier nucleus, schematically represented in Figure 1.1. With this process, stars similar to our Sun create heavier elements up to oxygen [3].

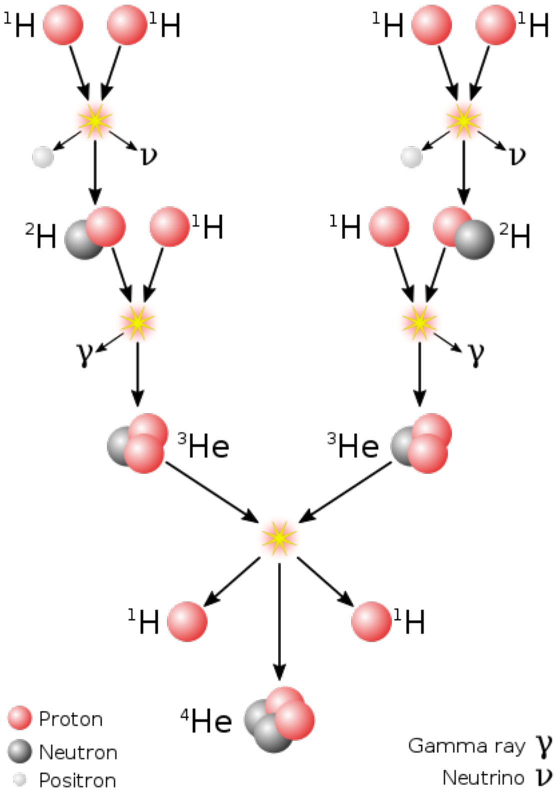

Figure 1.1: Scheme of proton-proton cycle of nuclear fusion taking place in the core of stars. Figure taken from Wikimedia Commons [4].

If the mass of the created nucleus is smaller than the sum of masses of original nuclei, the mass deficit (Δm) is transformed into energy, as predicted by Einstein famous formula:

$$E = \Delta mc^2. \tag{1.1}$$

For nuclear fusion to take place some conditions need to be met. As nuclei are positively charged, they are repelled by electrostatic Coulomb force. To be fused they need to be brought close enough so that the short range attractive nuclear forces can overpower the Coulomb repulsion. This can happen when nuclei have sufficient speed or energy [5]. In the core of the stars (similar to our Sun) temperature is above 1.5×10^7 K, and the density 150 g/cm^3 [5]. Recreating such conditions on Earth is an impossible task, at least in controlled conditions. Both criteria can be technologically met separately, currently we have no capabilities to achieve them simultaneously. To raise the efficiency of nuclear fusion on Earth, different mixtures of light isotopes are investigated. The fusion efficiency of some of those isotopes reactions is shown in Figure 1.2.

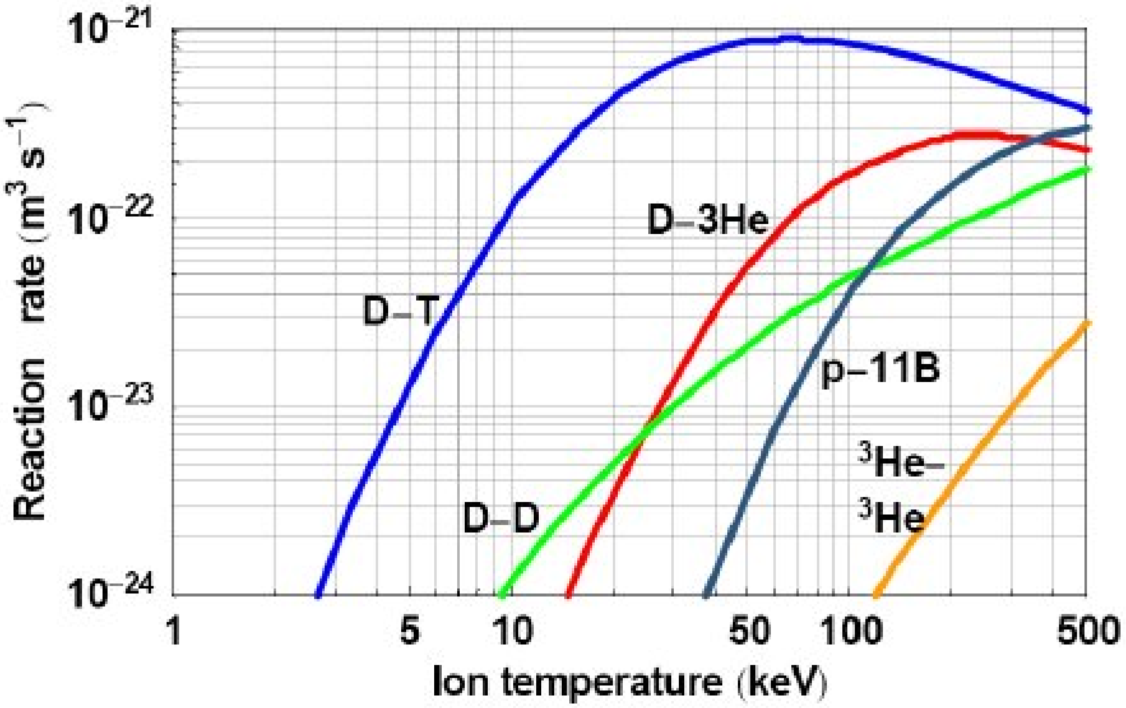

Figure 1.2: The fusion rate for some of light isotope reactions. D-deuterium, T-tritium. Figure taken from D. Petkow et.al [6].

The most favourable reaction is the fusion of deuterium (D) and tritium (T). It is known as the D-T reaction and can be achieved at relatively low temperatures. For a significant reaction rate the required temperature needs to be above 5×10^7 K, while the particle density is 10^{10} times lower than in the core of the stars [5]. The D-T reaction produces helium nuclei (^{4}He) and one additional neutron. The released energy of 17.6 MeV is transformed into kinetic energy of both products [5]. The D-T reaction is schematically shown in Figure 1.3.

To achieve suitable conditions for nuclear fusion on Earth, several concepts have been proposed. In the past 50 years, the most progress has be made in thermo-nuclear fusion devices with magnetic confinement. One of most developed designs in current age is the tokamak configuration [8].

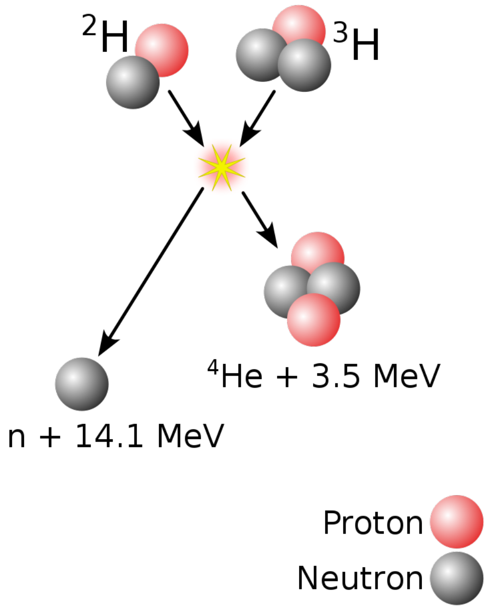

Figure 1.3: Schematic representation of D-T fusion reaction, which seems to be the most favourable for energy production on Earth. Image taken from Wikimedia Commons [7].

1.1 Tokamak

Tokamak is an abbreviation, which can be translated from Russian as "toroidal chamber with magnetic coils" [9]. Before the brief description of thermonuclear fusion device design and operation, we need to discuss the state of gasses inside the fusion device. The fusion fuel needs to be heated to 10^7 K. At this temperature, gasses are ionised and can be confined with magnetic fields in different geometries [10]. The most developed geometries currently are tokamak [9] and stelerator geometry [11]. The simplified cross section of the tokamak magnetic field geometry is shown in Figure 1.4.

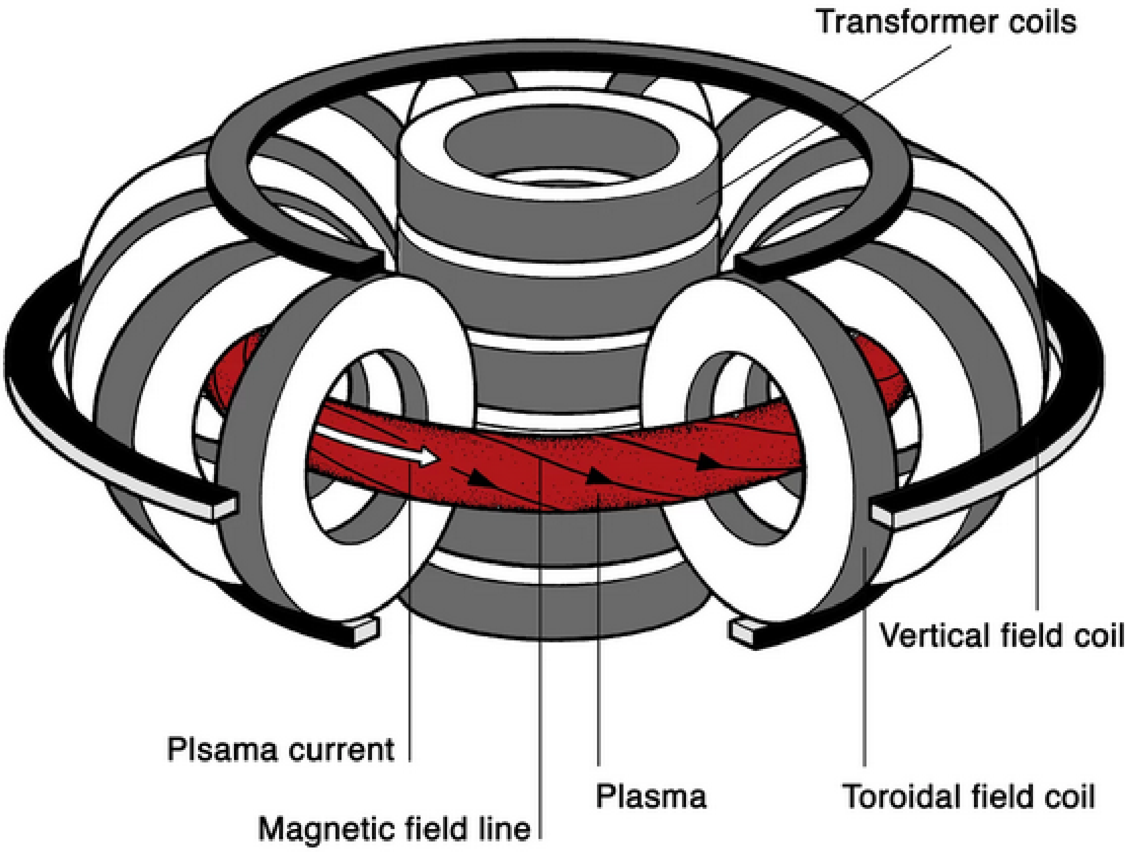

Figure 1.4: Schematic representation of tokamak design. Figure taken from IPP web page [12].

Deeper understanding of tokamak design and operation is not vital for understanding of this work. The short overview can still be helpful in understanding some conclusions. In Figure 1.4 we see the magnetic coils, which are used to create the strong magnetic fields to confine the plasma, which is in the shape of a torus. For future discussion we need to define a coordinate system used in the torus description and further used in discussion about tokamaks. One direction is called toroidal and the second is called poloidal direction. The poloidal direction follows a small circular ring perpendicular to the torus, while the toroidal direction follows a large circular ring around the torus, encircling the central void. Schematically both directions are shown in Figure 1.5.

For describing the size of the tokamak we use two main parameters, the major radius b and minor radius a. The radii are defined in Figure 1.6.

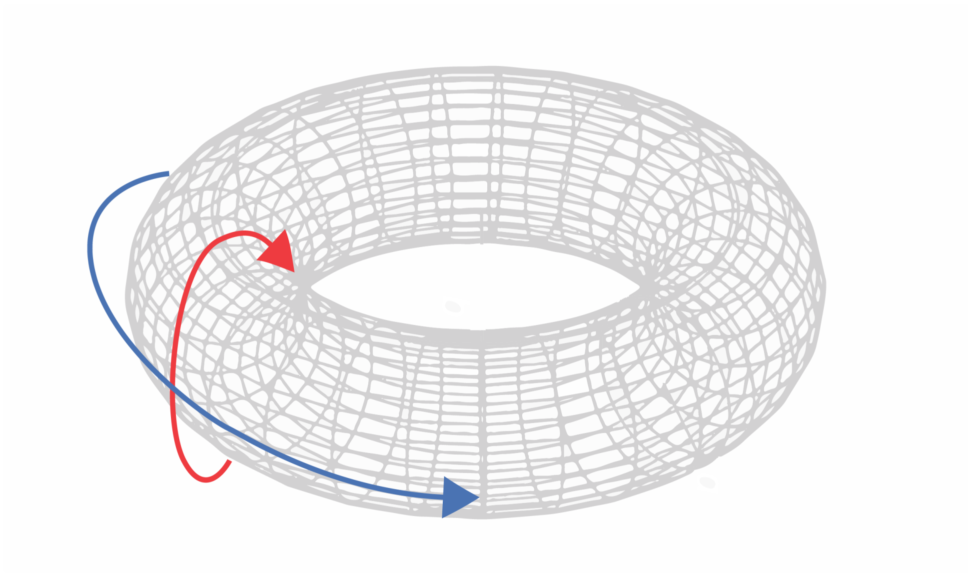

Figure 1.5: Coordinate system for describing the tokamak. Toroidal direction is marked with the blue arrow and poloidal direction with the red arrow.

The experiments on machines showed that circular cross-section of plasma chamber is not optimal for long time plasma confinement. So, a newer D-shape cross-section was invented and tested having better plasma confinement properties. In Figure 1.7 we show the schematic of such a D shaped tokamak. The presented scheme is for ASDEX Upgrade tokamak, which one is also used in this study.

Plasma inside the tokamak can be understood as a fluid in motion. The ions are moving in the toroidal direction and due to that they are experiencing a centrifugal force. This force is strong enough that particles in plasma are separated as in a centrifugal mass spectrometer. After a few journeys around the main torus the particles are pushed to the outside of plasma. After the last closed magnetic field line the scrap-off layer or SOL is formed, from where the particles are removed from plasma. On the inner side the SOL is separated from the core plasma by separatrix, which is the border magnetic field line that confines the core plasma. Most of tokamaks currently in use are designed with a special region of the main plasma chamber called divertor [14], with the main job to perform the removal of waste products from the burning plasma. In future reactors these are the heavier nuclei created during nuclear fusion. Divertor operates on a centrifugal principle of mass separation: when plasma is passing the divertor, the nuclei are pushed to the outer perimeter of plasma where they collide with divertor material and deposit their energy, which can be transformed into heat or carried away as kinetic energy of sputtered atoms. The modern D-shaped tokamak provides a natural positioning of divertor at the bottom [14] of the plasma chamber, outside the main plasma core. In such design the separatrix can be manipulated into x-point, in vicinity of which the magnetic field is significantly weaker, thus allowing an easier escape for particles towards the divertor [14]. Thus, the divertor is exposed to a large particle flux which leads also to a large heat load. The plasma regions and their position in modern D-shaped tokamaks are shown in Figure 1.8.

The parameter that controls thermal and particle loads exerted on the components is

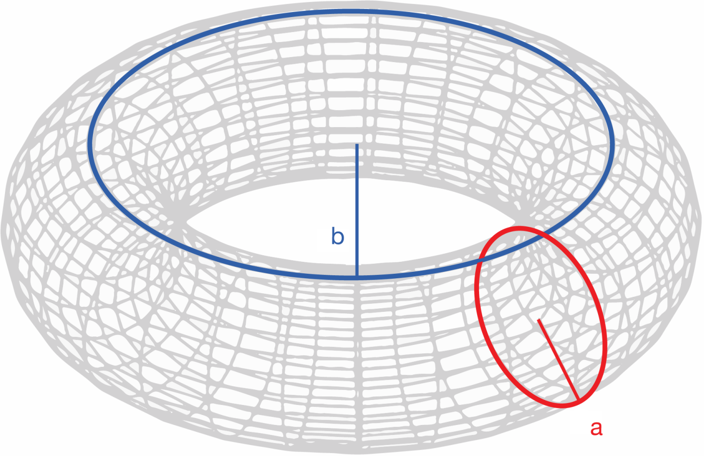

Figure 1.6: Schematic representation of the torus with the main radius denoted as b and the minor radius denoted as a.

the Q factor. It measures the ratio of the used heat for plasma heating and the energy released by nuclear fusion, where Q is defined as:

$$Q = \frac{\text{Relesed energy}}{\text{Used energy}}. \tag{1.2}$$

In current fusion devices the Q is close to 0, as the D-T mixture is only occasionally used as plasma gas. ITER [8], currently under construction, is the largest fusion device with predicted power plant performance, for which the maximum Q is expected be $Q \approx 10$ [8].

The divertor will be exposed to a particle flux peak value of 5×10^{23} $1/\mathrm{m}^2\mathrm{s}^1$, which corresponds to thermal loads up to 20 $\mathrm{MW/m}^2$, while normal operating thermal loads are expected to be 10 $\mathrm{MW/m}^2$ [16].

To handle these severe conditions the divertor can be made only from few materials. For now tungsten is one of the best options [14]. The material is not easy to machine, presenting problems in making a smooth divertor. Usually the divertor is split in castellated segments made out of flat tiles. However, the thermal and particle loads are a challenge for the material. The involved processes are described as plasma-wall interaction (PWI).

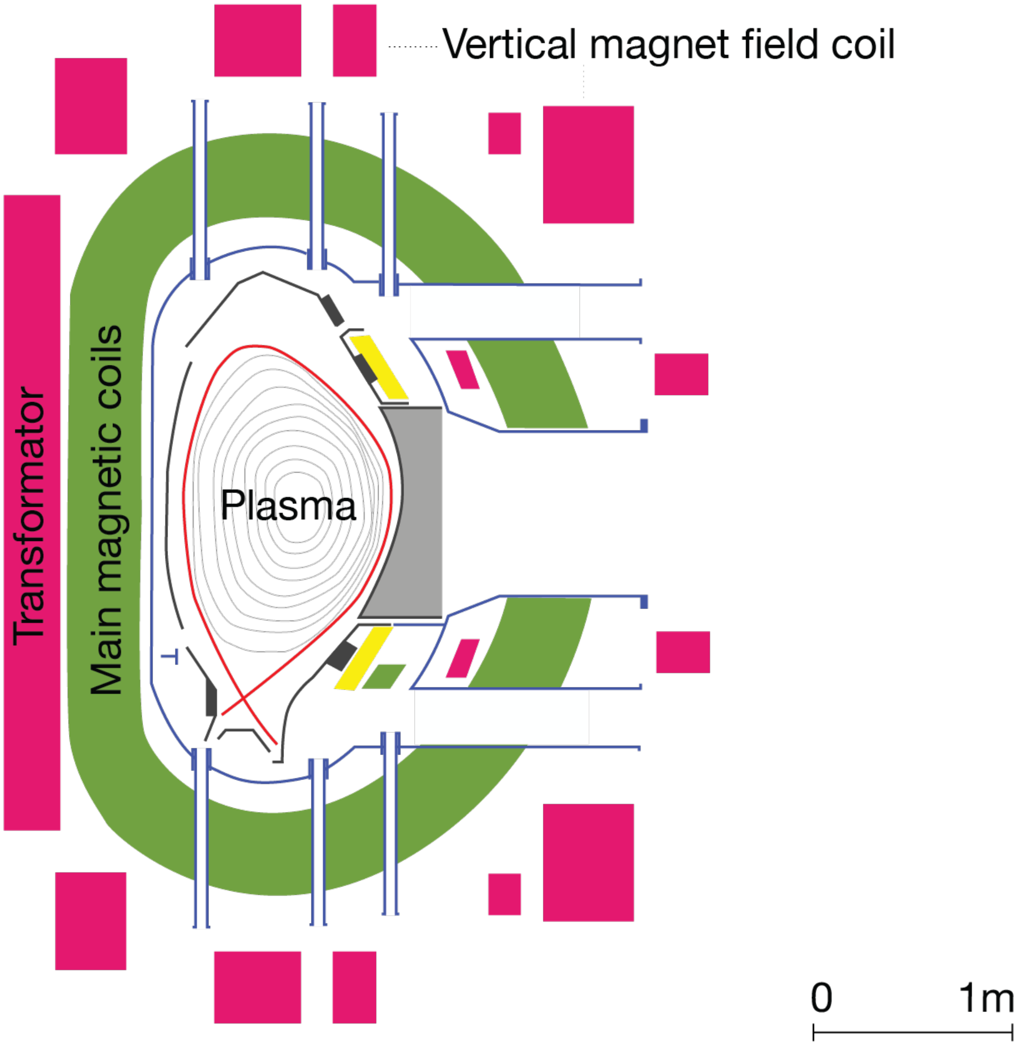

Figure 1.7: Cross section of the AUG vacuum vessel (blue), first wall with plasma facing components (grey), main magnetic coil (green) and vertical magnetic field coils (pink). Figure taken and modified from ASDEX Upgrade web page [13].

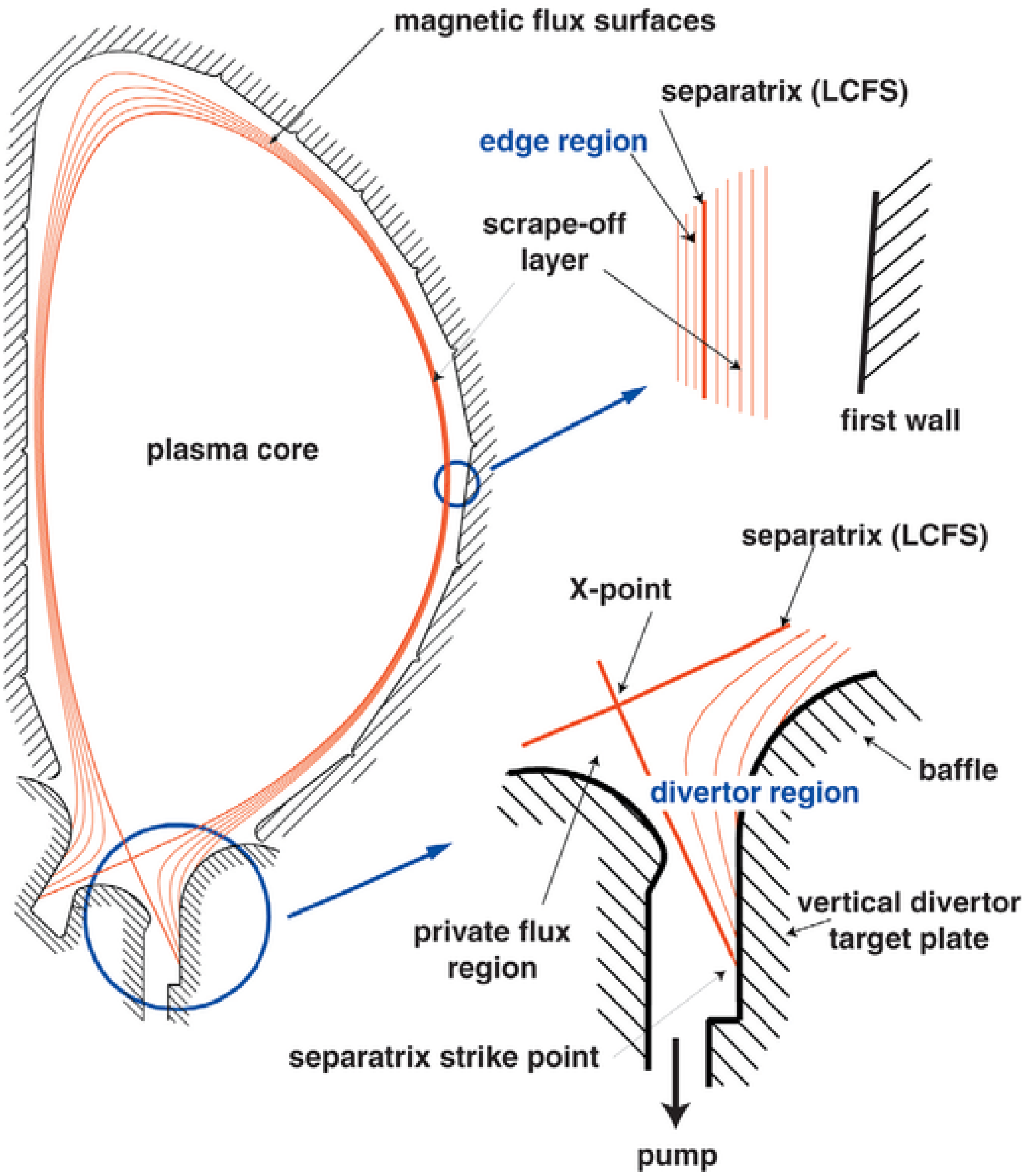

Figure 1.8: Schematic representation of main plasma regions in a modern D-shaped tokamak design. Figure taken from G. Federici et al. [15].

1.2 Plasma-Wall Interaction

Although the magnetic fields in tokamak confine the plasma to a sufficient level, there is still some interaction of plasma with the inner wall of fusion reactor. The study of plasma-wall interaction is an important topic in fusion related research. Numerous processes are going on between the plasma and the wall material [17]. These processes, schematically represented in Figure 1.9, can in general be divided into two groups, of which one is having direct impact to plasma stability and thus to the operation of a reactor. Main processes in this group are fuel trapping and recycling. This is when fusion fuel, hydrogen isotopes, is trapped in the first wall material. Trapped fuel can be released back into the main plasma. Thus causing the instabilities in plasma burning, and lowers the efficiency of fusion process.

The other processes have a direct impact to the life time of the inner wall: erosion, deposition and neutron bombardment of inner wall material. Where the erosion and deposition are going on in parallel. Some material is removed by energetic particle bombardment at the surface of the wall and redeposited on other components of the vacuum vessel. Meanwhile the neutron irradiation changes the physical properties of the first wall materials via the crystal lattice damage and elemental transmutation.

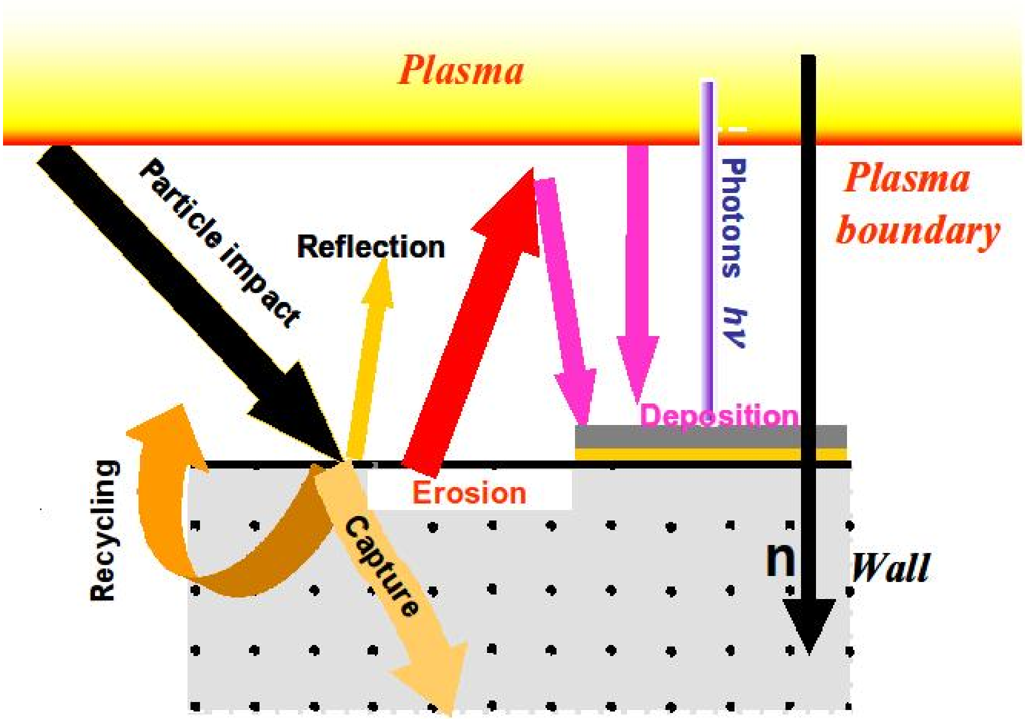

Figure 1.9: Scheme of plasma wall interactions inside of tokamak thermonuclear fusion reactor. Figure taken from the work of M. Rubel [18].

The process of erosion is the main topic of this work. Due to the low density of particles in the plasma, of the order of $10^4 - 10^5$ m^{-3} [5], the erosion is caused by energetic particles, originating in the plasma, colliding with surface atoms of the wall material. This process is called sputtering. The particles that cause sputtering are expected to have energies in the keV range. The sputtered material is mixed with plasma, which can lead to plasma contamination, disruption of plasma confinement and consequent to interruption in stability of the fusion reaction. The sputtered material can also be redeposited on other parts of the inner wall, increasing its active surface and increasing the fuel retention.

These processes are undesirable in operational state of the reactor [5]. Therefore, the knowledge of the behaviour and the effect of this process is needed for a safe and efficient operation of thermonuclear fusion reactors. As both of these processes have the same origin in sputtering of the wall material the study of sputtering process is essential for understanding the behaviour of the inner wall.

In the past comprehensive studies were done of the sputtering processes for an extensive combination of materials/targets and impinging ions, summarised in chapter 2 of [19]. Most of studies were done on polished targets and at normal incidence [19]. It is straightforward to compare the theoretical predictions with the measured data. However, the obtained data can only serve as an orientation in the use of fusion devices. The main limitations arise from the fact that inside the fusion reactor the angles of incidence are distributed over the entire 90° interval and in general far from perpendicular. In the future reactors or power plants large quantities of inner wall materials will be required [8]. Since it is costly to produce larger areas of mirror polished surfaces, surfaces with higher surface roughness will be used. For a wider interval of impinging angles and higher surface roughness the approaches developed in the past lack the power to predict the lifetime of specific surfaces inside the reactor.

The need for experimental data is even more pressing since the theoretical approaches for sputter yield calculation are only approximations, heavily dependent on input parameter from experiments. That is the subject of this study.

Plasma conditions can only be simulated in the laboratory to a certain extent, ultimately controlled experiments in real size tokamaks are needed. Work in this study was performed in the scope of EUROfusion program [17]. Experimental work was done in ASDEX Upgrade tokamak, description of which is in the following section.

1.3 ASDEX Upgrade Tokamak

ASDEX Upgrade is a fusion device of tokamak design located at Max Planck Institute for Plasma Physics in Garching, Germany [20]. AUG is designed to mimic plasma scenarios in ITER and its successor DEMO. The loads in the divertor can reach around one fifth of peak values in ITER.

ASDEX is abbreviation for Axially Symmetric Divertor Experiment. The original ASDEX was put in operation in 1980 [20], originally a torus with major radius of $b = 1.65$ m and minor radius of $a = 0.4$ m [20]. In 1991 the original ASDEX set-up was upgraded to ASDEX Upgrade (AUG) machine [21]. A new D-shape cross-section plasma vessel was installed, to replace the circular one, presented in Figure 1.7. The AUG uses 33 vertically and horizontally positioned coils around the plasma vessel to create the toroidal magnetic field of 3.9 T [13] in a special magnetic configuration. It allows controlling the interaction between the hot plasma and the surrounding walls. The control enables energy deposition of the main plasma in the divertor region of tokamak with great precision. The present set-up is constructed to mimic the conditions in future fusion power plants i.e. the essential plasma properties, primarily plasma density, plasma pressure and the wall load [22]. Complete inner wall of AUG (except the experimental samples) is made of pure tungsten [21], while in power plants the majority of the inner wall will be made of other materials. For ITER the main first wall will be made of beryllium and in future DEMO some components will be made of Eurofer steel. However, in all designs the divertor is still predicted to be made of W [8].

AUG is equipped with some tools that make the handling of experimental samples easier. Two out of 128 divertor tiles are coupled with AUG-DIM-II device [23], which is a manipulation device for a quick exchange of two divertor tiles without the need of breaking the vacuum in the main chamber of AUG. The time needed for tile installation and removal from the vacuum vessel is of the order of hours instead of weeks, when the main vacuum needs to be broken [23]. The overview of the entire AUG-DIM-II is shown in Figure 1.10.

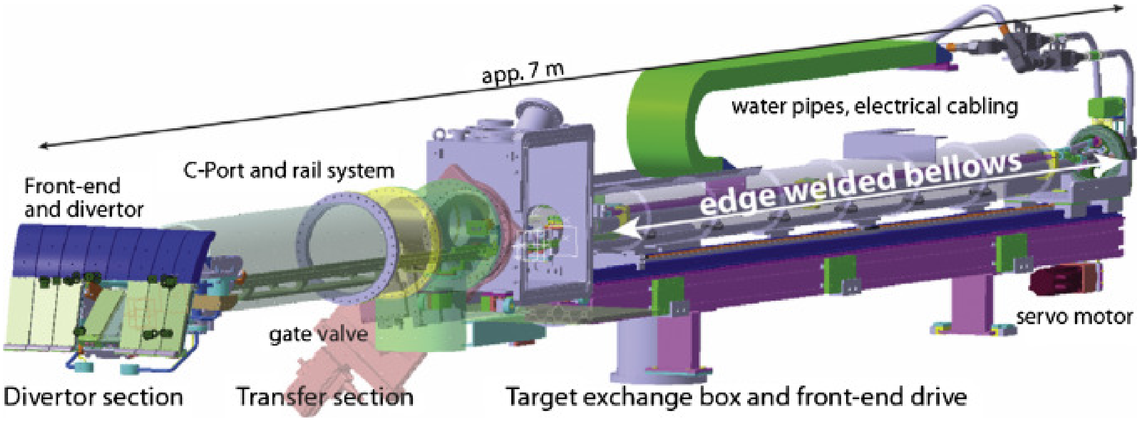

Figure 1.10: Schematic representation of the divertor manipulator AUG-DIM-II main components. Figure taken from A. Herrmann et al. [23].

The two removable divertor tiles are equipped with a cooling system. They are indistinguishable from other divertor tiles with regards to the plasma. The exchange tiles are made of pure W with two special grooves that can host six sample tiles each. To fit inside the groove the sample tiles have to have dimensions of $33 \times 15 \times 4$ mm with a special notch, discussed in detail in the sample preparation section. This set-up is useful in the scenarios where samples have to be exposed to a predefined number of controlled plasma discharges.

AUG is equipped with many plasma diagnostic probes that are connected with magnetic coils control loop. With this tool the position of the separatrix strike point on outer tiles (see Figure 1.8) of divertor is well defined and can even be manipulated during the plasma discharge. This outer strike point (OSP), is a line on the divertor where maximum particle and power loads are deposited [23]. The configuration of AUG with DIM-II is a tool for studying plasma surface interaction in the divertor region of thermonuclear reactors built in tokamak configuration. The experimental time for this research was carried out in ASDEX Upgrade tokamak, description of which is in the folowing section. experimental program of Medium Size tokamaks (MST1) group of EUROFusion project, where the special task T19, devoted to research in erosion process in tokamakas got approved. For this task eight discharges on 19.02.2019 were allocated.

Chapter 2

Theoretical Background

In the following section we describe the theoretical background important for understanding the process of sputtering and the analytical techniques used for quantification of obtained results. For the latter we will concentrate on ion beam analytical methods, as they present the main tool in our investigation of the effect of surfaces on sputtering and impurities retention. The chapter is divided into two parts, the first one dealing with the standard theoretical description of the sputtering process, and the second one with the theoretical background of ion beam analytical methods.

If observed on macroscopic scale it seems that two different physical descriptions are needed for sputtering and ion beam analytical methods. However, on micro scale both processes start with inter-atomic collisions. This can be theoretically described as binary collisions between solid objects. In general, even a classical description, without using a quantum dynamic approach, yields good agreement with experimental results. The relative simplicity of such a description is suitable for computer modelling with Monte Carlo calculations. We describe this in detail in the section 3.5 of this thesis.

2.1 Theoretical Background of Sputtering

In the last 50 years many theoretical and numerical approaches have been developed attempting to describe the processes of sputtering. The description with individual particle interaction is not directly applicable in the context of macroscopic objects used in fusion devices, therefore we use a quantity called sputter yield, or, in older literature, also called a sputtering yield. It is defined as:

$$Y = \frac{\text{average number of removed atoms}}{\text{number of incident particle}}. \tag{2.1}$$

The definition assumes that the average number of eroded atoms is proportional to the number of impinging ions. This is true in most combinations of target and projectile. Some deviation from linearity can be observed when the incident particle is a heavy molecule or atomic cluster at energies $E > 10$ keV [19]. For this we need to distinguish two cases.

If binding energy of the cluster E_c is $E_c \approx E$ or $E_c < E$ the whole cluster is taken as one impinging particle. If $E \gg E_c$, each atom or molecule in the cluster is counted as a separate impinging particle in the calculation of the sputter yield.

It is important to use the average number of removed atoms, as the number of removed particles per one single impinging particle can vary significantly. The impinging particle can be an atom, ion, molecular ion, atomic cluster, molecular cluster or a photon. From here on we will shall use "ion" or "ions" for all the above species of impinging particles. We will use "atom" or "atoms" for particles in the target, which can also be sputtered in the form of atoms, ions or atomic/ionic clusters. During the sputtering process also a secondary electrons are created, however their contribution to sputtering can be neglected. As their energy is in the range of few eV, which is below the threshold for sputtering of atoms.

The most elaborated theoretical approach to calculate the sputter yield is the application of the integral transport equations for amorphous solids in the linear cascade regime [19], [24]. Some approximate solutions utilising spherical potential of atom-atom collisions and neglecting the energy loss of electrons were derived by P. Sigmund in 1969 [24]. An asymptotic solution for a monoelemental amorphous solid target and a single species of impinging ions can be written as [24]:

$$Y(E_0, \Theta_0) = \Lambda F_D(E_0, \Theta_0, 0). \tag{2.2}$$

Here E_0 is the incident energy and Θ_0 is the angle of incidence of the impinging ions [19], [25]. The physics of interaction is hidden is the so-called nuclear energy deposition function in an infinite medium, evaluated at the surface of medium, x=0. In the above equation this is denoted with $F_D(E_0,\Theta_0, 0)$, proportional to the nuclear stopping power $S_N(E_0)$ for ions in the target medium [19], while Λ is a material factor which for planar surfaces is approximated as [19], [24]:

$$\Lambda = \frac{\Gamma_m}{8(1-2m)NC_mE_s(1-2m)}. \tag{2.3}$$

Here Γ_m is a numerical factor ≈ 0.4 and C_m is the nuclear cross section. The number m is power exponent in the power interaction potential, $0 \leq m \leq 0.5$ and N is an atomic density. The Λ can be simplified to

$$\Lambda = 0.04/NE_S, \tag{2.4}$$

as a good enough approximation [26]. Here E_S is the surface binding energy of the target atom, usually the heat of sublimation ΔH_s for the specific element is adopted. Finally, the sputter yield can be approximated as:

$$Y(E_o, \Theta_0) \sim \frac{0.4}{NE_S} S_N(E_0). \tag{2.5}$$

In Eq. (2.5) both main parameters E_S and S_N need to be taken from the experimental data. E_S can be measured with different independent experiments with sufficient precision, while nuclear stopping power S_N is hard to measure and some theoretical models have been proposed. However, it turned out that computer simulations in binary collision approximation yield good results. So nowadays the analytical approach to calculate sputter yield is more or less obsolete, while the Monte Carlo code utilising binary collision approximation is growing raise in popularity, yielding good results.

2.1.1 Binary Collision Approximation

As seen from the theoretical approaches one of the main quantities in calculating the sputter yield is the stopping power of the impinging particle. As an ion impinges onto the target, it undergoes a series of collisions with a target atoms until it finally stops at some depth. For further discussion we assume the initial energy of the ion is higher than the binding energy of atoms in the target but still low enough not to penetrate the target to significant depth. This condition is satisfied for the energy range from 100 eV up to 10 keV. Then, the stopping power can be divided into two contributions, and written as:

$$S = S_n + S_e, \tag{2.6}$$

where S_N represents the nuclear stopping power (collision of ions with nuclei of target atoms) and S_e the electron stopping power (electrostatic interactions between ions and electrons).

Both interactions, nuclear and electronic, can be treated as a binary collisions. However, usually the electronic stopping power is further simplified and described in the viscous fluid approximation model. This is briefly described in section 2.1.2. As one of the simplifications the target atom is taken at rest. Even at room temperature the thermal energy can be neglected as the energy of the ion is usually above 100 eV, while the kinetic energy of an atom at room temperature is about 1/40 eV. The ion-atom collision is an elastic process, with energy and momentum conserved in the collision. Even in an elastic collision some transfer of energy to surrounding electrons can occur [27]. This is the classical approximation of a binary atomic collision, where quantum mechanical effects are ignored. The classical approximation of the binary collisions is still used in most Monte Carlo codes, TRIM and its descendants SRIM or SDTrimSP [28], [29]. In the classical picture we can treat the collision of charged particles as in Figure 2.1, where LS stands for laboratory system, and CMS is centre-of-mass scattering system.

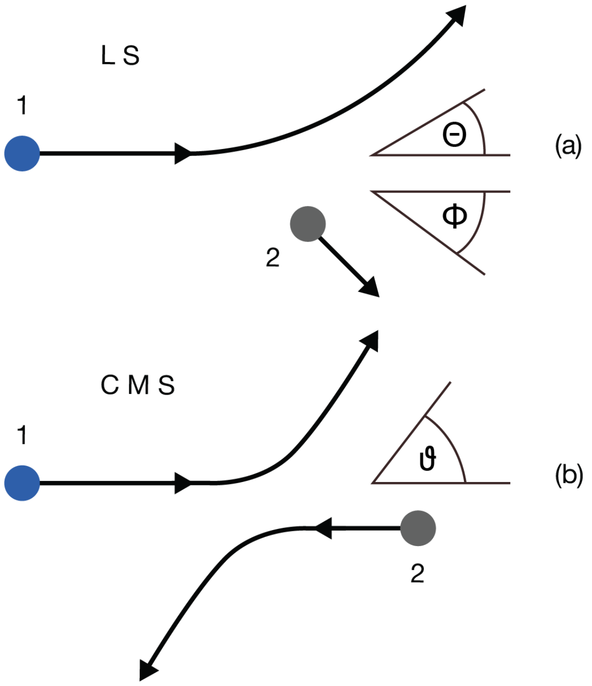

Figure 2.1: Schematic representation of the scattering coordinate systems: a) Laboratory system and b) centre of mass system. Based on figures in W. Möller [27].

In LS the particles can be characterised by scattering angles Θ and $\varPhi$. Due to the conservation of total system momentum in CMS entire collision system can be reduced to deflection angle ϑ and particle with reduced mass

$$\mu = \frac{m_1 m_2}{m_1 + m_2}. \tag{2.7}$$

Here m_1 and m_2 are masses of the projectile and the target particle, respectively. From momentum conservation the transformation equations between LS and CMS can be expressed as [27]:

$$\tan\Theta = \frac{\sin\vartheta}{\frac{m_1}{m_2} + \cos\vartheta}, \quad \Phi = \frac{\pi - \vartheta}{2}, \tag{2.8}$$

and for the reverse transformation from LS to CMS as [27]:

$$\vartheta = \Theta + \arcsin(\frac{m_1}{m_2}\sin\Theta). \tag{2.9}$$

In the CMS not all the kinetic energy of projectile is available for scattering, it is reduced for a factor [27]:

$$E_{\mathrm{CMS}} = \frac{m_2}{m_1 + m_2} E, \tag{2.10}$$

where E is projectile kinetic energy in LS.

In collision the energy transfer between the projectile and the target takes place. Energy transfer from the projectile to the target atom in the LS is [27]:

$$T = \gamma E \sin^2(\Theta/2), \tag{2.11}$$

where γ stands for energy transfer factor

$$\gamma = \frac{4 m_1 m_2}{(m_1 + m_2)^2}. \tag{2.12}$$

Summarily, taking into account that $E' = E - T$, the equation for projectile energy after the collision E' in LS is [27]:

$$E' = \frac{m_1^2}{(m_1 + m_2)^2} \left(\cos\theta \pm \sqrt{\left(\frac{m_2}{m_1}\right)^2 - \sin^2\theta} \right) E. \tag{2.13}$$

This relation of energy transfer can be applied in variety of the different regimes. One is a collision of the high energy (MeV) He nuclei with a heavy target atoms. This process is called Rutherford scattering and its analytical application is termed Rutherford backscattering (RBS) [30]. The detailed description of RBS is in section 3.1, where theoretical concepts of ion beam analysis (IBA) methods are presented.

In the above description of the model we had an isolated target atom and one impinging ion. In reality the targets are macroscopic, and target atoms are interacting with each other. After the first ion-atom collision the recoiled atom collides with neighbour atoms. The masses of the projectile and the target are the same $m_1 = m_2$, therefore the expected energy transfer is quite high, as seen from Eq. (2.13). Thus, the recoiled atom creates a collision cascade in the target. The general case is schematically represented in Figure 2.2, where gray circles represent target atoms and the impinging ion is shown in blue.

Both the ion and the recoiled atoms come to rest when their kinetic energy drops to the thermal energy of the target substrate, as the typical binding energy of atoms in the lattice is in the range 3 –10 eV.

In the definition of sputtering the target atoms are supposed to leave the target surface. For this to happen the component of the momentum of the recoiled atoms in the direction of the surface normal has to be sufficiently large. This can be achieved either in direct collision with primary ion or in collision with recoiled atoms in the collision cascade. As is easy seen from the kinematics of binary collision the sputtering in a direct collision is more likely after the primary ion has gone through some collisions in the collision cascade. This is schematically represented in Figure 2.3 a, while the recoiled cascade is represented in Figure 2.3 b.

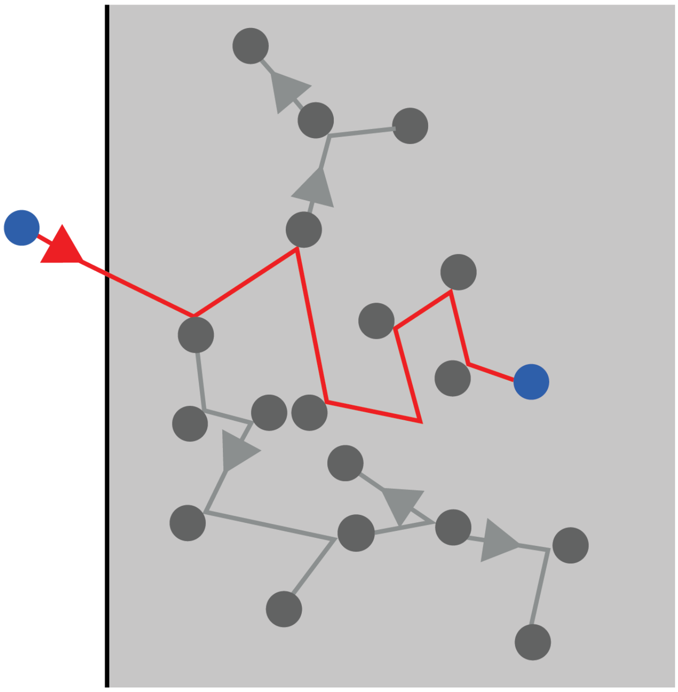

Figure 2.2: Generalised schematic representation of the cascade collision process in solid amorphous target, where the blue circles represent the impinging particle and the gray ones the atoms in the target. With the red line the path of impinging particle is traced and with the gray line the path of recoiled target atoms. Based on figures in W. Möller [27].

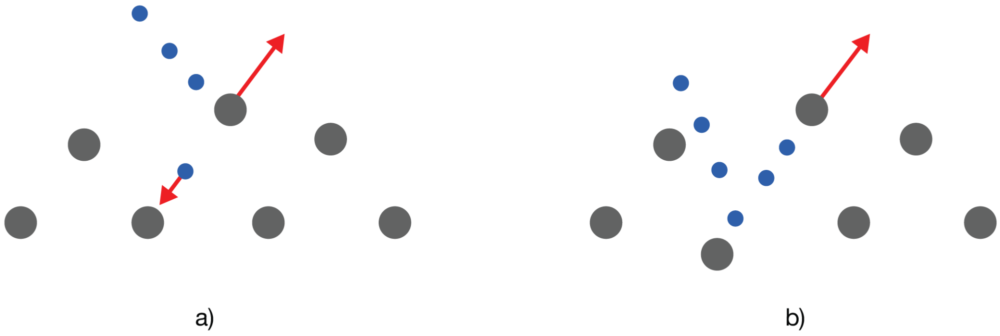

Figure 2.3: Schematic representation of the sputtering process. a) direct sputtering of an atom, b) indirect sputtering via the collision cascade.

Intuitively speaking there should be some effect of the impact angle of the primary ion beam on the sputtering of target atoms. Significant work has been done on this topic in the past, to be described in some details in section 2.2; in addition a significant effect of surface roughness on sputter yield has been observed, to be discussed in section 2.3.

2.1.2 Electron Stopping Power

The target atoms are not just a bare nuclei ordered in a lattice. They are surrounded by an electron cloud. The interaction with ions or recoiled atoms can still be treated as a binary collision. Taking into account that the mass of an electron is roughly 2000 times smaller than the mass of an ion, we can neglect the change of momentum in collision. Thus, for low energy ions, within previously stated energy range, the electronic stopping power can be treated only as an energy loss. In the target solid we can imagine electrons as an electronic cloud between nuclei of target atoms. This cloud interacts with low energy ions as a viscous liquid and hence the electronic stopping power can be approximately described as [31], [32]:

$$S_e = \left(\frac{z_1^{7/6} z_2}{(z_1^{2/3} + z_2^{2/3})3/2} \right) 4a_0 N v, \tag{2.14}$$

where z_1 is the ion atomic number, z_2 is the lattice atom atomic number, a_o is the Bohr radius, N is the target atomic density, and v is the ion velocity. Electronic stopping is inelastic process, the energy loss is dissipated through the electron cloud into the thermal vibrations of the target.

2.2 Angular Dependence of the Sputter Yield

Experimental data show that the sputter yield depends on the angle of incidence of ion beam. Here the angle of incidence is defined as the angle between the sample surface normal $\vec{n}$ and the ion beam direction or ion momentum $\vec{p_i}$. It can be defined as:

$$\alpha = \arccos\left(\vec{p_i} \cdot \vec{n}\right) - \frac{\pi}{2},\ 0 \leq \alpha \leq \frac{\pi}{2}, \tag{2.15}$$

where we assume $\vec{p_i}$ and $\vec{n}$ are unit vectors, schematically presented in Figure 2.4.

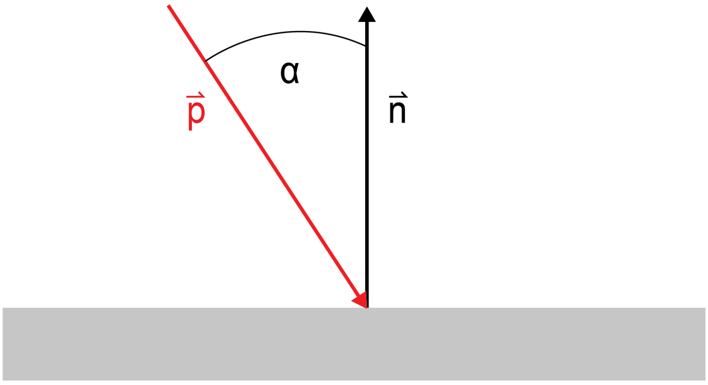

Figure 2.4: Schematic representation of angle of incidence.

Theoretical approaches to describe the angular dependence of the sputter yields, have proven as hard. However, even the basic computer simulations, such as TRIM.SP [33], predict an angular dependence. An algebraic fit formula has been developed by Eckstein et al. [34], to describe angular dependence of sputtering yield with as few free parameters, for arbitrary combination of the target atom and the impinging ion. A short summary of this work is presented. If the formula is evaluated as a relative change of sputter yield $Y(E_0, \alpha)$ compared to the sputter yield at 0° impact angle $Y(E_0, 0)$, with E_0 is a energy of impinging ion (mono-energetic), this fraction can be written as [34]:

$$\frac{Y(E_0,\alpha)}{Y(E_0,0)} = \left\{\cos\left[\left(\frac{\alpha}{\alpha_0^*}\frac{\pi}{2}\right)^c\right]\right\}^{-f} \exp\left(b\left\{1 - 1/\cos\left[\left(\frac{\alpha}{\alpha_0^*}\frac{\pi}{2}\right)^c\right]\right\}\right), \tag{2.16}$$

parameter α_0^* is introduced, defined as [34]:

$$\alpha_0^* = \pi - \arccos\sqrt{\frac{1}{1 + E_0/E_{\mathrm{sp}}}} \geq \frac{\pi}{2}. \tag{2.17}$$

With this parameter we take care for the fact that the angle of incidence of 90° cannot be reached. E_{sp} is the binding energy of the target atom. In the case of self bombardment $E_{\mathrm{sp}} = E_{\mathrm{sb}}$, the surface binding energy or heat of sublimation, while for hydrogen isotopes and nitrogen $E_{\mathrm{sp}} = 1$ eV is assumed and $E_{\mathrm{sp}} = 0$ eV for noble gasses [19], [34]. If $E_{\mathrm{sp}} > 0$ the projectile experiences an acceleration and a reflection close to the bombarded surface whereby the angle of incidence is effectively decreased [19], [34]. The parameters f, c, b are usually obtained from fitting the calculated sputter yields, with codes like TRIMS.SP [33] or the derived codes. The fit to experimental data is usually avoided as surface roughness can significantly affect the values and trends of sputter yield, and the formula is derived for an ideally smooth surface and only valid for this case. Although it is not explicitly specified the parameters f, c, b have some energy dependence which also needs to be taken into account when using fit formula: for fast calculations tabulated values of parameters are used [19].

The angular and energy dependence of sputter yield is presented in Figure 2.5 where nickel sputtering with He is presented, and the case of copper self bombardment.

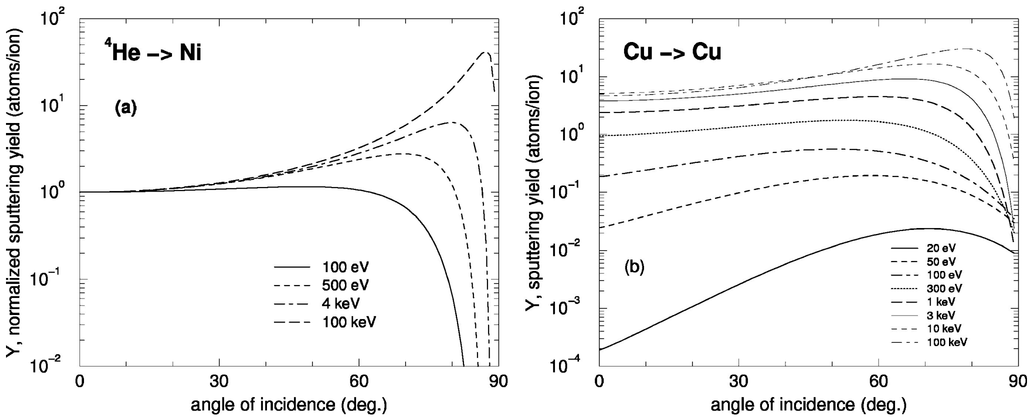

Figure 2.5: Fits to the calculated angular dependence of sputter yield at different incident ion energies, for sputtering of nickel with helium (normalised to sputter yield at $\alpha = 0$) and self sputtering of copper. The plots are taken from Eckstein et. al. [19].

With such a formulation of Eq. (2.16) Eckstein et al. also defined the angle α_{0m}, where sputter yield reaches its maximum: [19], [34]

$$\alpha_{0m} = \frac{2}{\pi} \alpha_0^* \left[\arccos(b/f)\right]^{1/c} . \tag{2.18}$$

The energy dependence of α_{0m} for D ion and Mo target is shown in Figure 2.6, where the increase of α_{0m} with the increasing energy is viable.

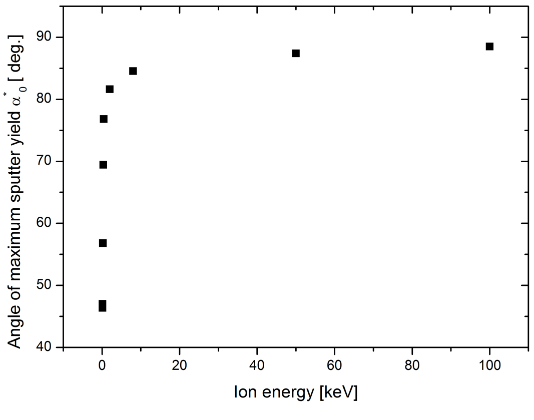

Figure 2.6: Energy dependence of α_{0m} for D ion and Mo target. The data are taken from Eckstein et.al. [19].

2.3 Effects of Surface Roughness on Sputter Yield

There are several definitions of surfaces roughness. In this work we have chosen the simplest definition defined as the arithmetical mean deviation of an assessed profile. For 1D case (a line) it can be calculated as:

$$R_\mathrm{a} = \frac{1}{l_r} \int_0^{l_r} |z(x)| dx. \tag{2.19}$$

Here the $z(x)$ represents the height deviation of point from the average height on the line, while l_r is the linear dimension of the analysed part. For 2D case (real surfaces) the definition can be extended simply as:

$$Ra = \frac{1}{l_x \cdot l_y} \int_0^{l_x} \int_0^{l_y} |z(x,y)| dxdy. \tag{2.20}$$

With l_x, l_y the linear dimensions of the analysed area are denoted. We assume that there is no macroscopic inclination of sample surface, which can be removed as a linear function from the height measurements data [35]. The formula describes surface roughness in the continuum case. As the characterization of 2D is usually done in mapping mode, in just some points of analysed surface, we need to extend Eq. (2.20) to the discrete case. Thus the output data of the measurements are in the form of $z(i,j)$, where $z(i,j)$ denoting the measured height in the given pixel (i,j). In addition, real measurements are made with some offset, compared to an average height of analysed surface. The integral form can then be rewritten in discrete form as:

$$R_\mathrm{a} = \frac{1}{N_i * N_j} \sum_{i,j} |z(i,j) - \overline{z}|, \tag{2.21}$$

where $\overline{z}$ is average measured height and N_i, N_j are pixel dimensions of map. An example of atomic force microscope (AFM) [36] measurement of real surface is shown in Figure 2.7.

The surface roughness affects the sputtering via different processes. The foremost is the effect of the local impact angle of ions. The ions hitting the rough surface, in case of perpendicular impact to the sample surface, do not have the same impact direction as the local normal of the surface. They can be oriented differently than the normal of the whole sample. This is schematically shown in Figure 2.8. The angle of incidence is not a single fixed value, it should be treated as a distribution $\rho(\alpha)$, where α is angle between the surface normal and the ion beam. This distribution is hard to calculate from surface input parameters, but can be easily modelled in the Monte Carlo codes. The effect of angle of incidence on sputter yield is discussed in subsection 2.2.

The second, more important, contribution of roughness to the sputter yield is its effect on redepositon of sputtered atoms. One of the assumptions for atoms leaving the surface is that their momenta are distributed by the spherical cosine distribution. This was shown by M. Küstner et al. [37], where an excellent agreement for beryllium was obtained. At point P where the atom leaves the surface in Figure 2.9, we can construct cosine sphere from the geometrical conditions define a cut-off sphere, as shown on Figure 2.9. This is the part of the sphere which contains the momentum directions not leaving the surface from point P. Ratio of the volume of this sphere divided by the volume of the whole sphere is called redeposition fraction defined as [37]:

$$R'_P(\sigma_P(\alpha), \alpha). \tag{2.22}$$

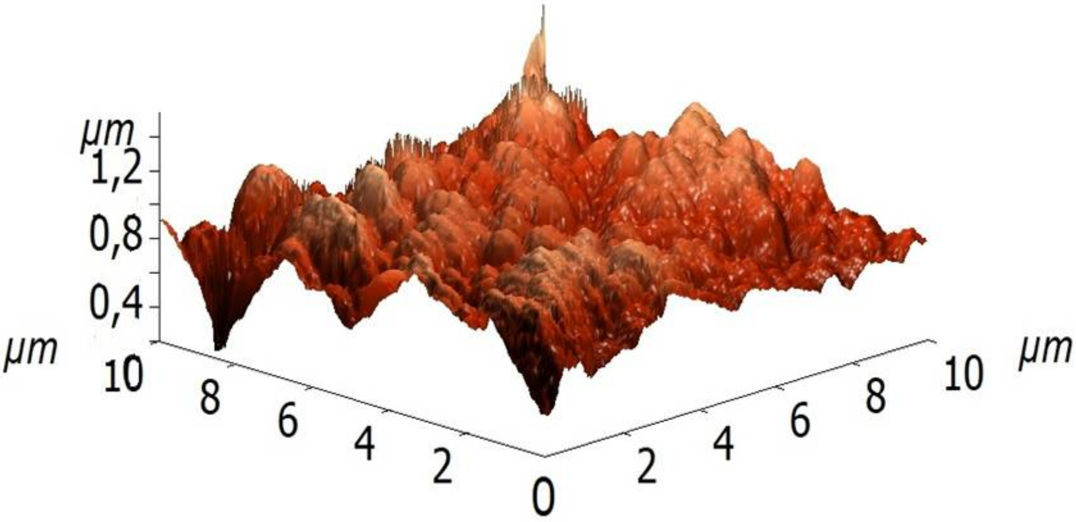

Figure 2.7: Atomic force microscope measurement of surface with $R_a \approx 110$ nm used in our studies. Figure provided by Rok Zaplotnik, JSI.

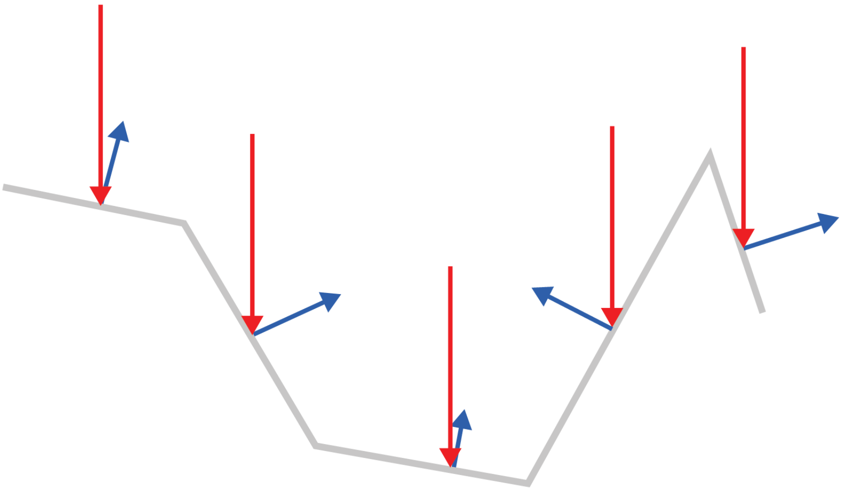

Figure 2.8: Schematic representation of the dependence of the impact angle with varying surface roughness. The red arrows represent the direction of ion beam and the blue ones the surface normal at the collision point.

Here the σ_P represents the local angle of incidence at point P.

By summing over all points on the surface and normalising over the sample surface A, M. Küstner et al. defined the redeposition factor as [37]:

$$R(\alpha) = \frac{1}{A} \sum_P R'_P(\sigma_P(\alpha), \alpha). \tag{2.23}$$

From definition we see that $R(\alpha)$ has a value between 0 and 1 and reduces the sputter

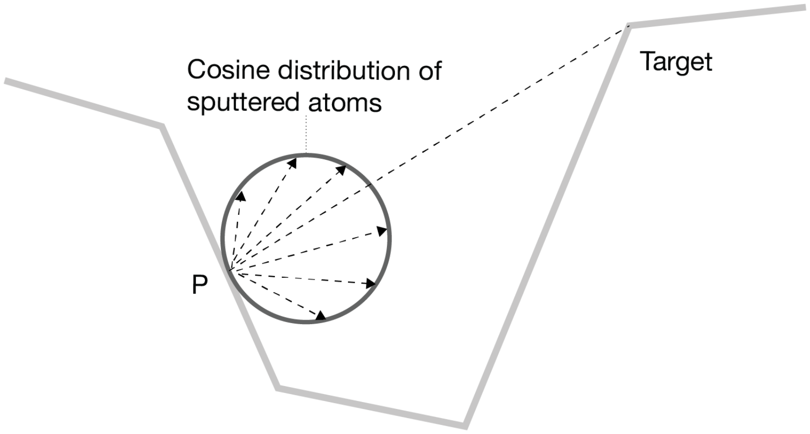

Figure 2.9: Schematical representation of sputtered cosine sphere on rough surface. Figure taken from M. Küstner et. al. [37].

yield as:

$$Y_{th}(\alpha) = Y'(\alpha)(1 - R(\alpha)), \tag{2.24}$$

where Y' is the calculated sputter yield for smooth surface. M. Küstner et al. showed for Be surfaces that $R(\alpha)$ can vary significantly for small variations of surface roughness, as shown in Figure 2.10 [37].

It is hard to directly link the samples used in the study of Küstner et al. [37] to surface roughness values, as they used for maximum height difference, measured on the analysed surface, instead of surface roughness, defined above. Yet it can be assumed that the maximum height divided by 2 is close to true value of Ra. With this assumption we can assign Ra values as, for Be polished $R_\mathrm{a} \approx 250$ nm, Be roughened $R_\mathrm{a} \approx 600$ nm and Be unpolished $R_\mathrm{a} \approx 600$ nm–750 nm [37].

In the study Küstner et al. went a step further, they measured the actual sputter yields for Be and compared them with the calculated value from TRIM.SP code [33], [38]. In more detail the process of calculating the sputter yield will be explained in the simulation section in Methodology chapter. The results in Figure 2.11 show the angular dependence of the sputter yield, predominantly for mirror polished surfaces, used in TRIM.SP calculation. At low impact angles an increase of the sputter yield for realistic samples is observed. Due to the surface roughness the angular dependence of the sputter yield is superseded compare to the prediction of TRIM.SP.

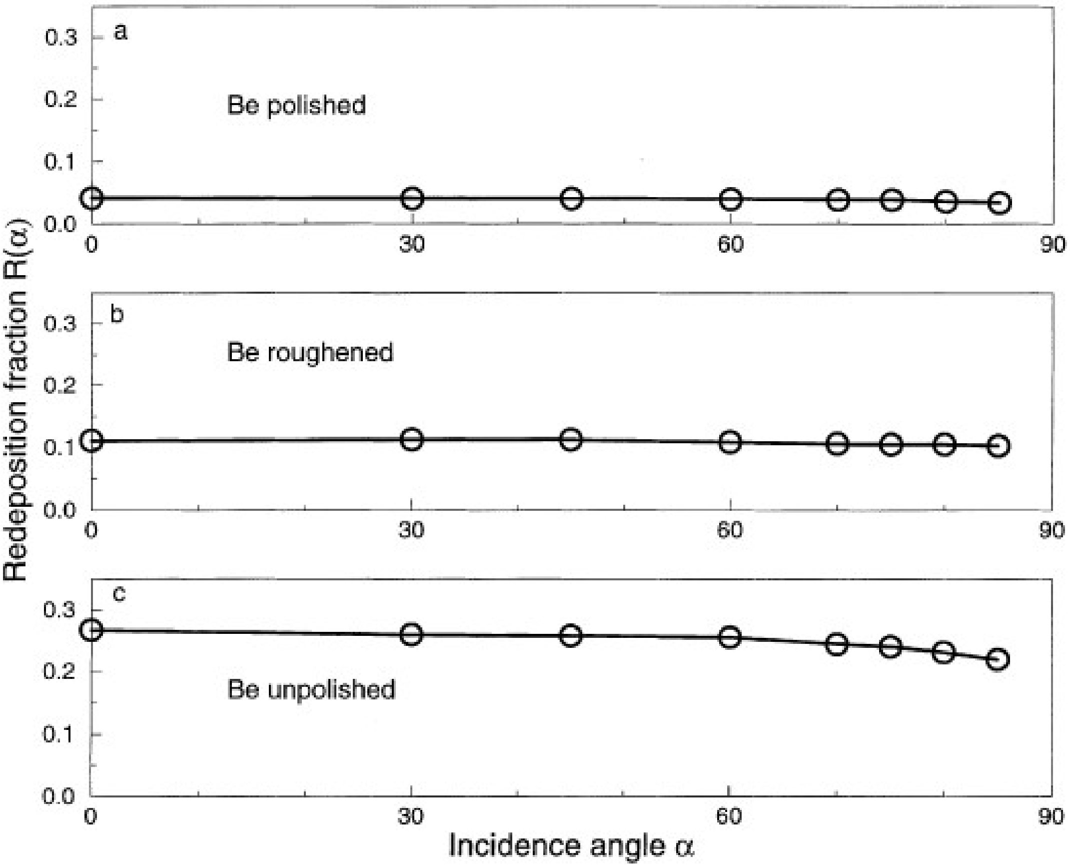

Figure 2.10: Redeposition fraction $R(\alpha)$ for Be samples used in the study by M. Küstner et al. $R(\alpha)$ are plotted against the angle of incidence. Where a) is polished Be $R_\mathrm{a} \approx 250$ nm, b) is roughened Be $R_\mathrm{a} \approx 600$ nm and c) is unpolished Be $R_\mathrm{a} \approx 600$–750 nm Figure taken from M. Küstner et al. [37].

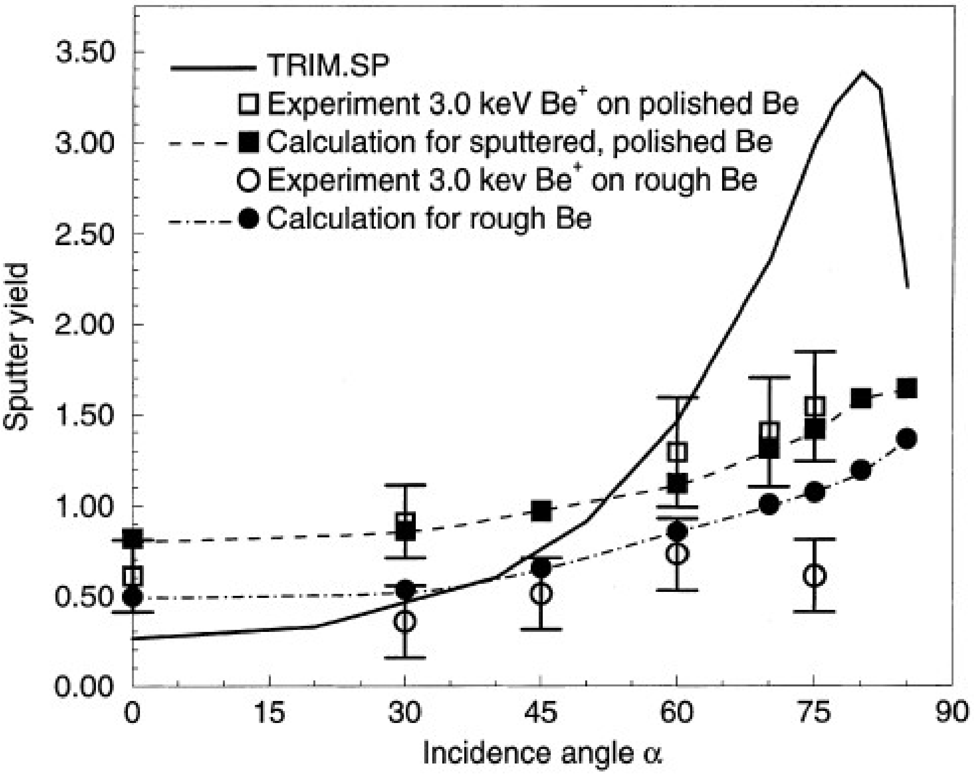

Figure 2.11: Angular dependence of sputter yield (measured and calculated) plotted for various surfaces used in the study of M. Küstner et al., and the calculated value of sputter yield for mirror polished surface (TRIM.SP). Figure taken from M. Küstner et al. [37].

2.4 Specifics of Sputtering in Fusion Relative Conditions

The above theoretical approaches are valid for all cases of sputtering. In the context of fusion, however, some specific assumptions can be made. To simplify the discussion, the focus will be only on the currently proposed and/or operational devices in tokamak geometry.

First we can see that ions that cause sputtering are hydrogen isotopes [39], deuterium and tritium, with atomic masses 2 and 3, respectively. In the plasma there are also ^{4}He nuclei and neutrons, the products of nuclear fusion [2]. Their contribution to sputtering can be neglected, despite a being products of nuclear fusion reaction and having energy in the MeV range. Neutrons, by their nature are weakly interacting particles and pass through the material with only weak interactions. Nuclei of ^{4}He interact and collide with other particles in the plasma and lose their energy. So when they reach the plasma-facing surfaces their energy will be in eV range, too low to cause sputtering.

In tokamak geometry the components, that are subjected to the highest particle fluxes, are made of heavy metallic elements. In the divertor region, where most of the sputtering in tokamak take place, tungsten is planned as the main material for components [14]. Tungsten has an atomic mass of 184 u. The maximum energy transfer in the collision with D or T is around 4 %, as calculated by Eq. (2.11). Since the surface binding energies for metals are in the order of few eV obviously there is some threshold energy, above which the sputtering will take place. For W and D combination this threshold energy is in the range of 200 eV for D, as found in the literature [19]. The ions impacting the wall of tokamak are not mono-energetic. They have some energy distribution, depending on specific plasma conditions during discharge.

Secondly, we need consider the impact angle of particles. Charged particles, ions, are moving along the magnetic field lines in a spiral pattern. Those hitting the surfaces arrive at similar angles as the angle between magnetic field lines and the surface. In the main plasma chamber this angle is close to 90°, but in this region the particle fluxes are rather low. In the divertor, being hit by a larger particle flux, the magnetic field lines intersect the surface roughly at angles of an 60°. Giration of particles and the sheet potential cause the true impact angle of particle to deviate from this specific angle of magnetic field lines [40]. Therefore we need to treat the angle of incidence in tokamaks only as a guide and be aware of an angular distribution of particles hitting the surface. This distribution depends on plasma configuration during the discharge, and can only be roughly modelled with specialised software. So this can only be done in post mortem modelling of the plasma.

All the above constrains are taken into consideration while designing our experiment and more importantly in the interpretation of the obtained results.

Chapter 3

Methodology

In this section we will describe the main points of experimental design and work flow intended to find an answer to the main hypotheses of this work:

1. Well defined laboratory measurements can predict erosion behaviour of first wall materials inside of thermonuclear fusion reactors in tokamak configuration.

2. Ion beam analysis methods can provide useful information in post-mortem analysis of erosion in materials exposed to plasma in tokamak reactors.

In addition to the hypotheses a question naturally arises as how well can the modelling tools predict the sputter yields for rough samples. To find the answers the work was divided into three sections. The first one was the laboratory experiment in which we exposed samples of four different surface roughnesses in well defined conditions to 1 keV/D ions under different angles of incidence: 0°, 40°, 60° and 70°. The goal was to obtain the data on the sputter yield behaviour with respect to angle of incidence of the ion beam. The second part was the exposure of the same type of samples inside the ASDEX Upgrade tokamak. The aim was to test the prediction from the laboratory experiment for a real tokamak under operating conditions. The collection of data obtained in these two sections is a contribution to the design in future plasma-facing surfaces inside tokamaks. For the analysis and the consequent determining of the sputter yields the main tool was Rutherford backscattering spectroscopy- RBS. RBS is one of the techniques in the Ion beam analytical (IBA) family. In addition to RBS we also use particle induced x-ray emission (PIXE) and nuclear reaction analysis (NRA) for additional analysis of samples, mainly the ones exposed in tokamaks. In the third section the validation of calculations with SDTrimSP code was performed and compared with experimental data. With this comparison an evaluation we prepare guidelines for modelling complex surfaces in the code and improve the accuracy of calculations.

In the following sections a detailed description of each experimental or modelling step is given.

An important part of the study was production of consistent and well-defined sample surfaces. Samples were prepared and provided by co-workers from Max-Planck-Institut für Plasmaphysik, Garching, Germany (IPP), Istituto per la Scienza e Tecnologia dei Plasmi, Milano, Italy (ISTP) and Politecnico di Milano [41]. The sample preparation is briefly described in section 3.2.

3.1 Ion Beam Analytical Method

Ion beam analytical (IBA) techniques have proved a valuable tool in less destructive chemical analysis studies of materials. In the past decades we observe a wide application of IBA in in-situ and post-mortem analysis of materials used in fusion devices [17], [42]. One of the oldest and most widely used IBA techniques is RBS [43], [44]. It is based on detection of charged particles in MeV energy range with good energy resolution. From scattering energies we can deduce quantitatively the chemical composition of the sample. In most cases particles from a second order process in the medium ion beam current regime are measured, which with combination with MeV energy regime of primary ions makes RBS a very suitable technique for small and middle sized electrostatic accelerators. In parallel with RBS, nuclear reaction analysis (NRA) was developed. There the probing ion beam is used to induce nuclear reactions in target atoms and we rely on detection of reaction products. Complementary to both techniques the particle induced x-ray emission spectroscopy (PIXE) was developed, where the x-ray photons emitted during de-excitation of exited electron states are detected. These three techniques represent the core and most widely used IBA techniques [30].

3.1.1 Rutherford Backscattering -RBS

The operation principle of RBS method is relatively simple. An ion beam, in energy range of MeV, is directed to the target, and the ions back-scattered in some spatial angle with the respect to the direction of impinging ion beam are measured. However, to use RBS as an analytical tool, it needs to be made quantitative. The general scattering geometry, incident beam geometry (IBM), shown in Figure 3.1. In this geometry the exit beam and surface normal are in the same plan. In most analytical cases the geometry is even further simplified. Usually we assume perpendicular incidence of the analysing ion beam with respect to the sample surface, $\alpha = 0°$ [45]. The scattering angle θ is defined with respect to the direction of the incoming beam as shown in Figure 3.1.

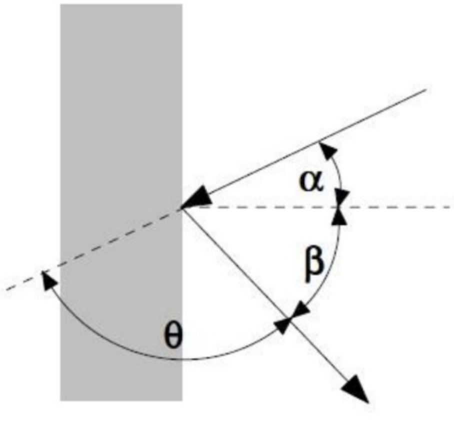

Figure 3.1: IBM geometry of ion beam scattering. Incident angle α, exit angle β and scattering angle θ. Figure taken from M. Mayer [45].

We can treat the scattering process as a binary collision of the probing ion and the target atom in a non-cascade regime. A part of the energy of the ion is transferred to the atom and the energy E_1 of the scattered ion is reduced. The energy reduction is a function of ion mass M_1 and target atom mass M_2. The energy loss in the laboratory system can be written as:

$$E_1 = KE_0, \tag{3.1}$$

where E_0 is the initial energy of the ion and the kinematic factor K is given by [43]

$$K = \frac{M_1^2}{(M_1 + M_2)^2} \left\{ \cos\theta \pm \left[\left(\frac{M_2}{M_1} \right)^2 - \sin^2\theta \right]^{\frac{1}{2}} \right\}. \tag{3.2}$$

In most cases the targets are not mono-elemental. We need to take into account that target is composed of two elements with mass difference of ΔM_2. Then we can calculate the difference in backscattering ion energy ΔE_1 given as:

$$\Delta E_1 = E_0 \frac{dK}{dM_2} \Delta M_2. \tag{3.3}$$

We can see that the best energy separation is achieved for low Z material in the target. We can partially increase the energy separation by using heavier ions. However, the energy resolution of semiconductor detectors (used in most of RBS set-ups) is deteriorated for higher Z ions so that the gain of resolution via the K factor is usualy negligible [45].

In the laboratory system the Rutherford cross-section for backscattered ions can be written as:

$$\sigma_R \left[\frac{mb}{sr} \right] = 5.1837436 \times 10^6 \left(\frac{Z_1 Z_2}{E\ [keV]} \right)^2 \frac{\left\{ (M_2^2 - M_1^2 \sin^2\theta)^{1/2} + M_2 \cos\theta \right\}^2}{M_2 \sin^4\theta (M_2^2 - M_1^2 \sin^2\theta)^{1/2}}. \tag{3.4}$$

In this notation σ_R is the differential cross-section in the laboratory system, and θ is the scattering angle, Z_1 and M_1 are the charge and mass of the probing ions and Z_2 and M_2 are the charge and mass of the target nucleus [44], [45]. Where the numerical factor at the beginning is taken from the average of experimental data.

Experimental results show the cross-section deviates from theoretical values of eq. (3.4) at low and high ion energies for all arbitrary projectile-target pairs.

Deviation at low energies is caused by partial screening of the nuclear charge by the electron shell surrounding the nucleus. This effect can be easily taken into account by introducing a correction factor F as:

$$\sigma = F\sigma_R, \tag{3.5}$$

where descriptions for F are provided by different authors [46]–[48].

The deviation at high energies, on the other hand, cannot be solved as easily, since this deviation originates from nuclear forces. There is no general theoretical approach to calculate this non-Rutherford scattering cross-sections. Since 1950 many authors have measured cross-section for different projectile-target combinations at different scattering angles. These results are used instead of theoretical predictions. One of the most used libraries is hosted by International Atomic Energy Agency (IAEA) and is called IBANDL. Library of the cross-sections is openly available [49].

It is not easy to recognise when the actual cross-sections will deviate from Rutherford theory. M. Bozoian et al. [50]–[52] have provided a criterion when we need to use experimental cross sections instead of theoretical as a guideline. They define the critical energy E_{NR}, in laboratory system, at which deviation of cross-section is > 4 % [50]–[52]:

$$E_{\mathrm{NR}}[\mathrm{MeV}] = \frac{M_1 + M_2}{M_2} \frac{Z_1 Z_2}{8}. \tag{3.6}$$

For Mo thin film measurements in this work we used ^{4}He ion beam of 2 MeV or 2.5 MeV, depending on the samples, explain in section about RBS measurement. For this combination the $E_{\mathrm{NR}} = 10.9$ MeV and the correction factor $F \approx 1$. From this we can conclude that these measurements were carried out in the Rutherford regime.

In the experimental set-up a detector covering a solid angle of $\Delta\Omega$ is active for time t. With the approximation of thin target (neglecting the stopping power of ions) of thickness d we can write the ion yield in the detector as [43] :

$$Y_i = \sigma_R(E_{\mathrm{ion}})\Delta\Omega j_{\mathrm{ion}} t n_i \frac{Ad}{\cos\alpha}. \tag{3.7}$$

Here j_{ion} denotes the ion density of the probing beam, of an area A. n_i is the number density of target atoms. A standard approach in RBS analysis is to use areal density of target ions

$$q_i = n_i d \left[\frac{\mathrm{atom}}{\mathrm{cm}^2}\right] \tag{3.8}$$

and ion dose

$$D = e_0 Z_{\mathrm{ion}} j_{\mathrm{ion}} A t, \tag{3.9}$$

were Z_{ion} represents the charge state of the probing beam. In this notation we can write areal density of target as [43]:

$$q_i = \frac{Y_i e_0 Z_{\mathrm{ion}} \cos\alpha}{D\Delta\Omega\sigma_{R_i}(E_0)} \tag{3.10}$$

In the designed experiment with monoenergetic beam and a thin target a typical spectrum is shown in Figure 3.2. In this spectrum the element peak is quite broad, as the sample layer of Mo was around 100 nm thick, which is equivalent to 640 $\frac{\mathrm{atom}}{\mathrm{cm}^2}$. The Mo was deposited on carbon substrate, but in Figure 3.2 we only show the high energy part of the spectrum, for clarity. If the thickness of the layer is decreased the width and height of the peak is reduced. Thus, the integral of the peak is a good measure for layer thickness.

The proportionality between peak integral and layer thickness is valid while the thickness of the layer does not cause a significant loss of the primary ion energy due to the stopping power. For thicker targets we need to take into account the stopping power of ions in material. Most widely used approach for calculating the energy loss, produced as a drag force of the electron cloud, for the ions in the target is Bethe-Bloch formula, which can be written as [44]:

$$-\frac{dE}{dx} = 0.1535 \left[\frac{\mathrm{MeV\ cm}^2}{\mathrm{g}}\right] \rho_2 \frac{Z_2}{A_2}\frac{Z_1^2}{\beta^2}\left[\ln\left(\frac{2m_e\gamma^2 v^2 W_{\mathrm{max}}}{I^2}\right) - 2\beta^2 - \delta - 2\frac{C}{Z_2}\right]. \tag{3.11}$$

The parameters δ and C are corrections to the Bethe-Bloch formula, with main effect at high and low energies, respectively. The main parameters of the Bethe-Bloch formula are W_{max} and I. W_{max} is the maximum energy transfer which is produced by a head-on collision between the ion and an electron and can be simplified as [44]

$$W_{\mathrm{max}} \approxeq 2m_e(v_{\mathrm{ion}}\gamma)^2. \tag{3.12}$$

The I is the mean excitation potential: it is essentially the average orbital frequency of the electron in Bohr formula times the Planck constant. In practice this parameter is hard to calculate, but many of semi-empirical formulas have been proposed to describe it. One such formula is [44]:

$$\begin{aligned} \tfrac{I}{Z_2} &= 12 + \tfrac{7}{Z_2}\ \mathrm{eV} & \qquad Z_2 &< 13, \\ \tfrac{I}{Z_2} &= 9.76 + 58.8{Z_2}^{-1.19}\ \mathrm{eV} & \qquad Z_2 &\geqq 13. \end{aligned} \tag{3.13}$$

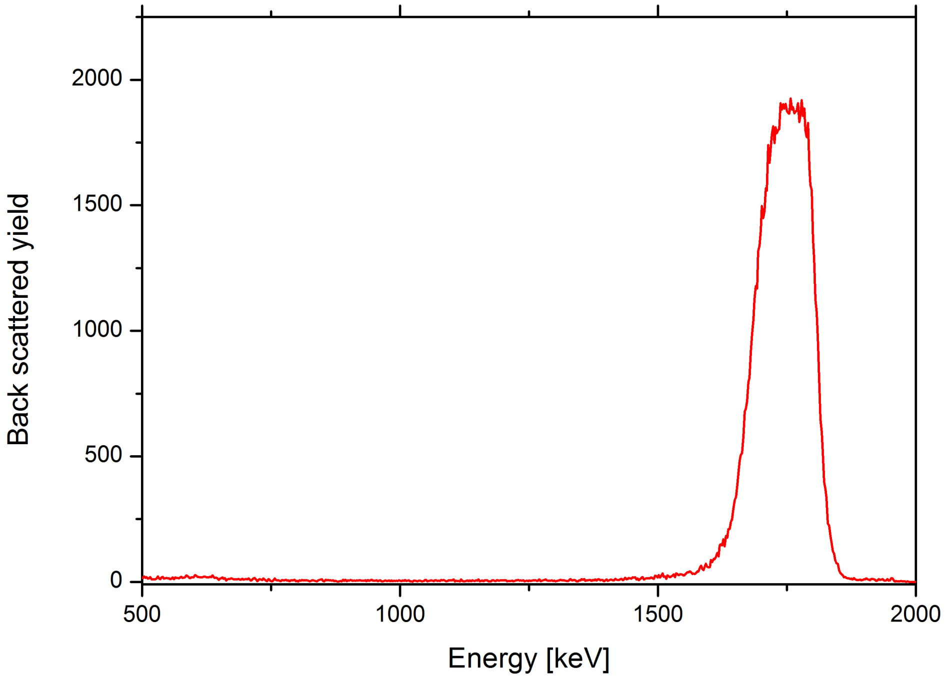

Figure 3.2: Measured spectra of backscatter ions on 100 nm thick Mo layer deposited on carbon substrate, using a 2 MeV ^{4}He beam and the detector positioned at scattering angle of 165°.

When measuring thick or bulk targets an example is presented in Figure 3.3: the spectrum of bulk rhodium metal measured with 2 MeV ^{4}He beam. On this spectrum we observe that the peak is transformed into a step, with an additional low energy tail, caused by multiple scattering of the primary ions.

When the thickness of the layer is greater than the range of the ions, the height of the step is proportional to the ion dose during the measurement. The edge of the step is well defined and corresponds to the ions backscattered from the sample surface. Thus, the RBS of bulk targets is mainly used for energy calibration of the detector system and ion dose measurement calibration. In principle RBS can be applied for bulk target composition analysis, but the main drawback is that it is only sensitive to the matrix elements, and is blind for the trace elements. So, supplementary ion beam analytical techniques are used. One of those is PIXE, described in the next section.

In most cases when RBS is used as an analytical technique, the targets are composed as a mixture of thin layers of several elements on some substrate. Thus, the quantification of obtained results cannot be simply done with peak integration or step height method, as described above. In those cases the software such as SIMNRA is used [53]. There we can model the layer composition and then the proper stopping powers are applied to account for energy shifts of the peaks, due to the energy loss of the scattered ions.

3.1.2 Particle Induced x-ray Emission

The particle-induced X-ray emission (PIXE) is a method in which emission of the characteristic X-rays is excited with fast ions. This is schematically represented in Figure 3.4. In

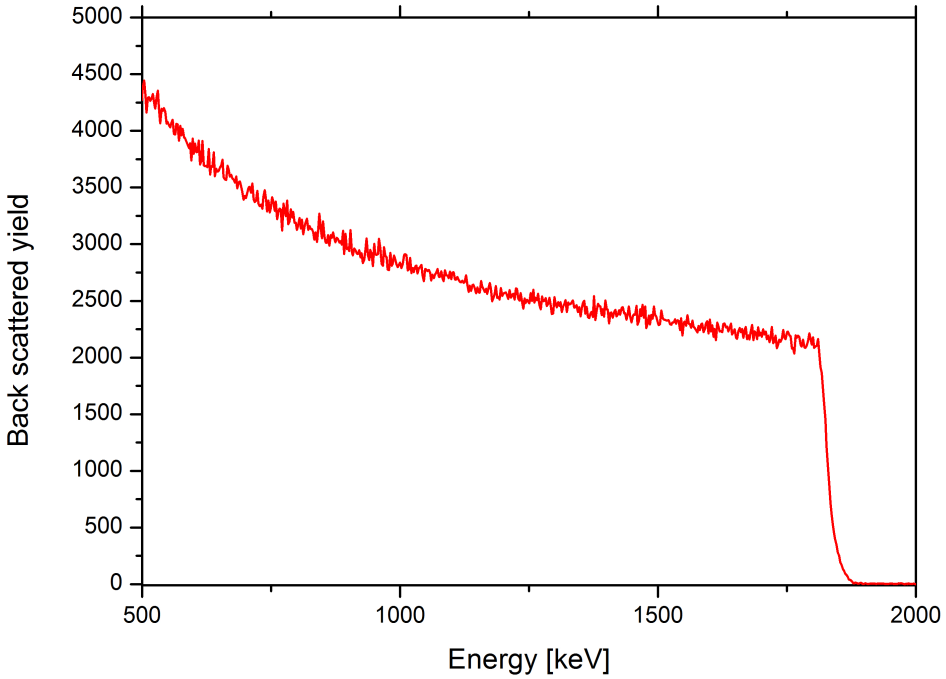

Figure 3.3: Measured spectrum of bulk Rh metal, using a 2 MeV ^{4}He beam and detector positioned at the scattering angle of 165°.

theory the excitation can be induced by any kind of fast ions. The depth of the analysed layer is dependent on the ion energy and ion species. Lighter ions, mostly protons, are used in practice. Characteristic rays can also be induced by the electrons with energies of some tens of keV, but a strong background is formed, due to breaking radiation of electrons in matter (bremsstrahlung). For this method the term energy-dispersive spectroscopy (EDS) was established. The main advantage of PIXE method is much lower bremsstrahlung than in EDS, allowing for a hundred or thousand times higher sensitivity for trace elements.

From the basic description we can see that PIXE signal is a side product of any kind of IBA analysis, as x-rays are always produced. For use only the installation of a suitable semiconductor detector is required at the experimental set-up to collect the spectra. An example of PIXE spectrum is shown in Figure 3.5. The characteristic peak yield integrals can be easily transformed into elemental concentrations in the sample.

Quantification for a thin sample can be easily derived by considering the impact of MeV ion beam on a thin layer of our sample. The resulting x-rays are measured with detector covering some solid angle. A further simplification can be made: for PIXE the derivation can be performed within the Bohr image of atomic structure. To avoid the complication of electron shadowing only a description for ionization of the K shell of an atom will be described [43].

For K lines we can write the x-ray production cross section σ_i^x simply as [43]:

$$\sigma_i^x = \frac{\sigma_i \omega_i}{1 + \frac{K_\beta}{K_\alpha}}, \tag{3.14}$$

with σ_i denoting the ionisation cross section for K shell of an atom. The ω_i is the probability of relaxation of the atom through radiative transition i.e. emission of x-ray.

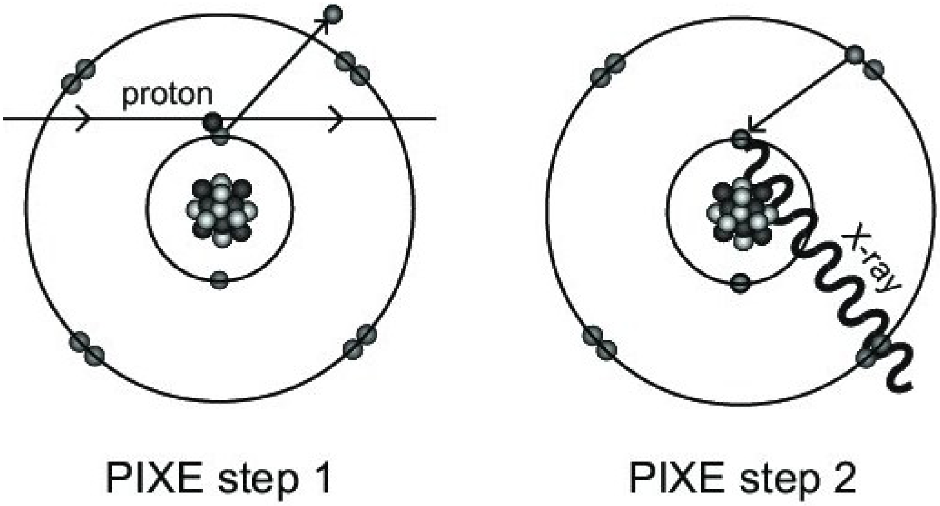

Figure 3.4: Schematic representation of particle induced x-ray emission - PIXE. Figure taken from T. Calligaro et al. [54].

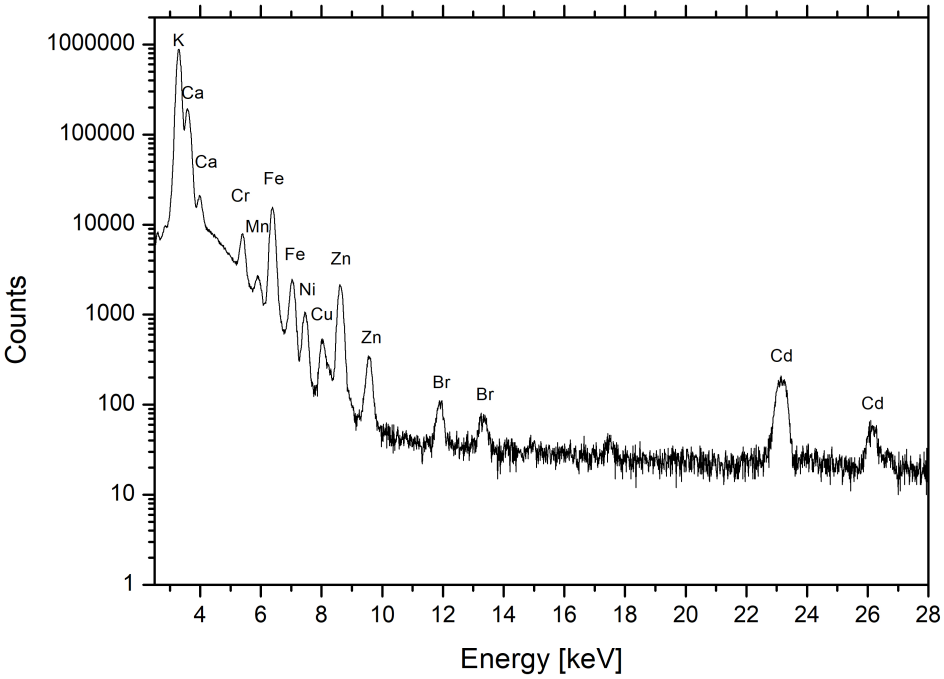

Figure 3.5: PIXE spectrum of a biological sample obtained by germanium x-ray detector. The peaks correspond to corresponding chemical elements.

The value of ω_i is function of Z, and it is almost negligible for elements with $Z < 9$. So, in practice PIXE is used only for elements with $Z > 9$ i.e. from fluorine on [55]. The term in the denominator gives the relative intensities of x-ray lines α and β.

As the sample is exposed to ion beam with fluence $j_p = N_p/At$, where N_p represents the number of protons impacting the target inside an area A in time t. If we take into account the N_i number of atoms inside the target, we can write the total x-ray yield Y_i^{tot} as [43]:

$$Y_i^{\mathrm{tot}} = \sigma_i^x j_p t N_i. \tag{3.15}$$

In a real experiment we do not have an ideal detector, covering the total solid angle of 4π. To take into account the solid angle of the detector, we add a factor $\frac{\Delta\Omega}{4\pi}$. For a good description we also need to take into account the detector efficiency ϵ_i, which is not 1. Moreover, the detector is not built just from active material, which detects x-rays: there are layers of absorbing material, such as beryllium windows, gold electrical contacts, etc. All this absorbers can be described with a single parameter η_i.

If we express the number N_i of atoms in interest in a chemical notation as $N_i = \frac{N_a \rho_i V_i}{M_i}$, and take into account the possibility of non-perpendicular impact of ion beam on the target, the analytical volume V_i can be written as $V_i = Ad/\cos\alpha$. Represented with d the range of the analytical ions. As a shorthand we introduce q_i as $q_i = \rho_i d$ and N_P as $N_P = j_P A t$. The final equation for PIXE yield can be written as [43]:

$$Y_i = \frac{\Delta\Omega}{4\pi} N_a N_p \frac{\epsilon_i \eta_i \sigma_i^x}{M_i} \frac{q_i}{\cos\alpha}. \tag{3.16}$$

The Eq. (3.16), shows that for the deduction of areal density q_i of an element, one must only know the characteristics of the detector and the number of ions deposited on the target.

All written above is only valid for thin targets as we neglected the absorption of x-ray photons in the target. We have also neglected the loss of the energy of the ion, while it penetrates the target. This is most important for characterization of ionising cross section σ_i^x, as it is dependent on the energy of the incoming ions [43].

Not to go into too much detail the equation for thick target can be constructed by considering the ion stopping power, which can be calculated or better yet measured for different combinations of ion/target. The absorption of x-rays in the target is given by [56]:

$$N_x = N_{x0} e^{-\mu z}. \tag{3.17}$$

With N_{x0} we denoted the number of emitted ions from some small volume at depth z inside the target, while μ represents absorption coefficient for x-rays in the target material. Analysed target can then be represented as a series of thin targets. By this a recursive solving of equations (3.16) for specific layer is allowed with deriving the total concentration. This approach is widely used in software used for PIXE spectra analysis. Nowadays GUPIX [57] inside GULEPH [58] Software package and GeoPIXE [59] are the most developed codes for fitting and analysis of PIXE spectra.

3.1.3 Nuclear Reaction Analysis

Nuclear reaction analysis (NRA) is an IBA technique of detecting products of the reaction between the target nucleus and primary ion beam. In general when ion from the primary beam hits the nucleus of the target atom an unstable nucleus is created, which soon decays, usually into two fragments. With a careful selection of incoming ion beam for specific analysing element, the unstable nucleus can be made to decay in one heavy and one light fragment. The light fragment takes most of the excess energy and can therefore escape from the target depth to be detected by the detector. Here is a short overlook on quantification of NRA results. The advantage of NRA is it is high selectivity and sensitivity for specific elements or isotopes. Instead of discussing the principles of NRA in general, it is easier to consider a specific nuclear reaction. In fusion application we mainly use the reaction D(^{3}He,p)α [60]. The analytical beam of ^{3} He ions in MeV energy range is directed onto a sample containing deuterium. The goal is to determine the quantity of deuterium accumulated in the sample and its depth distribution. Incident helium ions are elastically scattered in the sample, and inducing nuclear reactions on deuterium nuclei [49]:

$$\begin{aligned}
&{}^3_2\mathrm{He} +^2_1 \mathrm{D} \longmapsto^4_2 \mathrm{He} +^1_1 \mathrm{p} && Q = 18,35\ MeV\\
&{}^3_2\mathrm{He} +^2_1 \mathrm{D} \longmapsto^1_1 \mathrm{p} +^1_0 \mathrm{n} +^3_2 \mathrm{He} && Q = -2,73\ \mathrm{MeV}\\
&{}^3_2\mathrm{He} +^2_1 \mathrm{D} \longmapsto^2_1 \mathrm{D} +^2_1 \mathrm{D} +^1_1 \mathrm{p} && Q = -6,52\ \mathrm{MeV}\\
&{}^3_2\mathrm{He} +^2_1 \mathrm{D} \longmapsto^3_1 \mathrm{T} +^1_1 \mathrm{p} +^1_1 \mathrm{p} && Q = -1,95\ \mathrm{MeV}.
\end{aligned} \tag{3.18}$$

With Q the released energy in the reaction is denoted, readily transformed into kinetic energy of the reaction products. The first of above reactions is one of the most widely used fusion related IBA application. However, it is not the only nuclear reaction that can occur. Ions of ^{3}He can interact also with other target elements in the sample such as carbon, oxygen which also produce protons in the MeV energy range. For detection of carbon the reactions are [49]:

$$\begin{aligned}
&{}^3_2\mathrm{He} +^{12}_6 \mathrm{C} \longmapsto^{14}_7 \mathrm{N} +^1_1 \mathrm{p} && Q = 3,96\ \mathrm{MeV}\\
&{}^3_2\mathrm{He} +^{13}_6 \mathrm{C} \longmapsto^1_1 \mathrm{p} +^{15}_7 \mathrm{N} && Q = 9,85\ \mathrm{MeV}.
\end{aligned} \tag{3.19}$$

and for oxygen the reactions are [49]:

$$\begin{aligned}
&{}^3_2\mathrm{He} +^{16}_8 \mathrm{O} \longmapsto^{18}_9 \mathrm{F} +^1_1 \mathrm{p} && Q = 2.03\ \mathrm{MeV}\\
&{}^3_2\mathrm{He} +^{16}_8 \mathrm{O} \longmapsto^4_2 \mathrm{He} +^{15}_8 \mathrm{O} && Q = 4,91\ \mathrm{MeV}.
\end{aligned} \tag{3.20}$$

These reactions produce various products, which can be detected by the detection set-up. High-energy protons as the product of nuclear reactions are detected as they lose small amount of energy when passing through the sample material. From the measured data and properties of these nuclear reactions (kinematic relations and scatter cross-section) it is possible to estimate the depth profile of deuterium in the analysed layer [61] and profiles of other light elements, such as C, O and B when nuclear reaction is induced with ^{3}He ion beam.

The ^{3}He ions with their nuclear structure provide an excellent probe for performing the NRA. However, the use of other types of ions is more suitable. In the present work we also used proton beam for detecting ^{11}B and ^{15}N. Yet the principle of collecting and processing of the data to obtain quantitative informations is the same in all the cases.

The released energy for a specific reaction can be easy calculated in the center of mass system as a difference of kinetic energy of the initial and final state. For D(^{3}He,p)α reaction this is [62]:

$$\begin{aligned}
Q = T_f - T_i = c^2(M_i - M_f) = c^2(m_{\mathrm{He}} + m_{\mathrm{D}} - (m_a + m_{\mathrm{p}} + 2m_{\mathrm{e}^-})) =\\
= (2808.9 + 1876.1246 - 3727.38 - 938.27 - 2 \times 0.511)\ \mathrm{MeV} = 18.3526\ \mathrm{MeV}.
\end{aligned} \tag{3.21}$$

From the result $Q = 18.4$ MeV we see that the reaction is exothermic ($Q > 0$), which means that the initial state will always yield the selected final state, regardless of the initial kinetic energy of the incident helium ion. The released energy Q is completely converted into kinetic energy of the newly created particles (in our case the proton and α particle), observed in the CMS.

In the experiment we are detecting the nuclear reaction products, usually protons. They are scattered at a scattering angle $\theta = \pi - (\alpha + \psi)$. Here α represents the incident angle of ^{3}He and ψ recoiled angle of ^{4}He. Dividing the sample into a series of thin layers we can ask, how many particles are generated in a given layer and enter the detector. The number of detected particles from the selected layer is denoted by target yield dY. It is dependant on the cross-section $\frac{d\sigma_i}{d\Omega}$ of the selected nuclear reaction in the core layer selected, the solid angle $\Delta\Omega$ of the detector. We write the analytical beam particles flux as j_p. Also the chemical composition of the individual layers (density, atomic mass and mass elements in layers) affects the target yield. Since the treated layer consists of several types of atoms (which can produce protons), we measure the yield of each element in the layer separately [62]:

$$dY_i = \frac{d\sigma_i(E(E_0, z))}{d\Omega} \Delta\Omega j_0 t \frac{\rho N_A}{M_i} C_i(z) A dz. \tag{3.22}$$

Here we denoted by C_i the concentration of the selected element in the layers and i runs through all the elements in the layer which we are interested in. Introducing $Q_i^{^3\mathrm{He}} = j_0 t \frac{\rho N_A}{M_i} A$ and considering that $dz = \frac{dx}{\cos\alpha}$ we can write yield of a thin layer as:

$$dY_i = \frac{Q_i^{^3\mathrm{He}}}{\cos\alpha} C_i(x) \frac{d\sigma_i(E(E_0, z))}{d\Omega} d\Omega_{\mathrm{det}} dx \tag{3.23}$$

where $d\Omega_{\mathrm{det}}$ is the fraction of the solid angle of the detector, which accepts the particles flying from the sample at an angle $\approx \psi$.

Total yield per unit of time in the sample under investigation is computed by integrating expression (3.23) over the entire thickness of the layers L and the entire solid angle of the detector. The end result is:

$$Y_i(E_0, L) = \frac{Q_i^{^3\mathrm{He}}}{\cos\alpha} \Delta\Omega_{\mathrm{det}} \int_0^L C_i(X) \frac{d\sigma_i(E(E_0, z))}{d\Omega} dx. \tag{3.24}$$

The important factor is differential cross section $\frac{d\sigma_i}{d\Omega}$ for the specific reaction. Due to the nature of nuclear reactions, i.e. the complex structure of the matter and the forces which are in play in this reaction, the derivation of the scatter cross section is very complicated. To this end we always use the measured cross section for a specific nuclear reaction , for D(^{3}He,p)α [60], [63], [64], with the cross section presented in Figure 3.6.

If the cross section exhibits a resonance-like shape, as in the case of D(^{3}He,p)α, this can be used also for depth profiling. The measurements with varying energy of the analytical beam are required. We obtain the proton yield that predominates the depth at which primary ^{3}He ions achieve the resonant energy. NRA can then provide additional information on the distribution of a certain isotope distribution in the sample.

As seen from the equations (3.18), (3.19) and (3.20) the emitted protons from reactions have different energies. Thus, by measuring energy of the protons we can distinguish the nuclear reaction from which they are originated, and hence the element. A spectrum, obtained on a thin layer of amorphous deuterated hydrocarbon a-C:D, is presented in Figure 3.7. The 275 nm thick a-C:D was deposited on silicon and measured with 4.2 MeV ^{3}He ion beam.

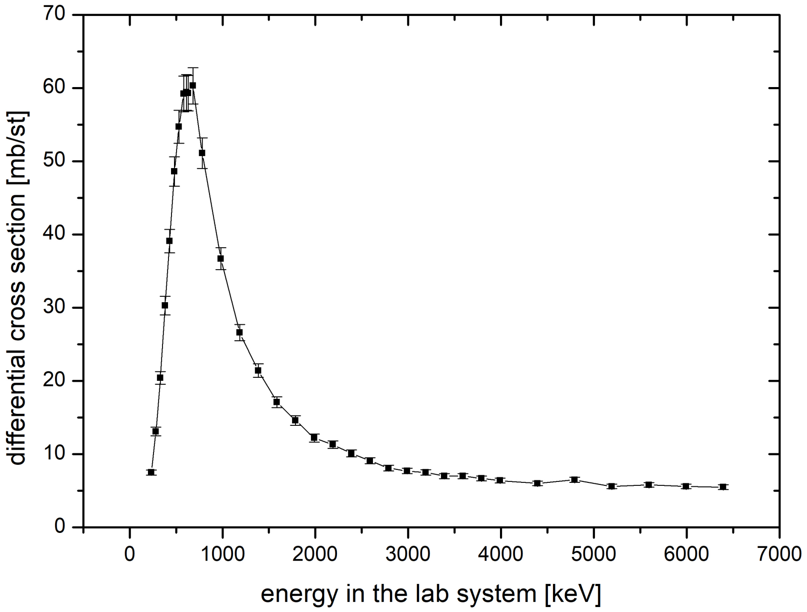

Figure 3.6: Differential cross section for D(^{3}He,p)α nuclear reaction at scattering angle of 135°. Data are taken from B. Wielunska et al. [64]

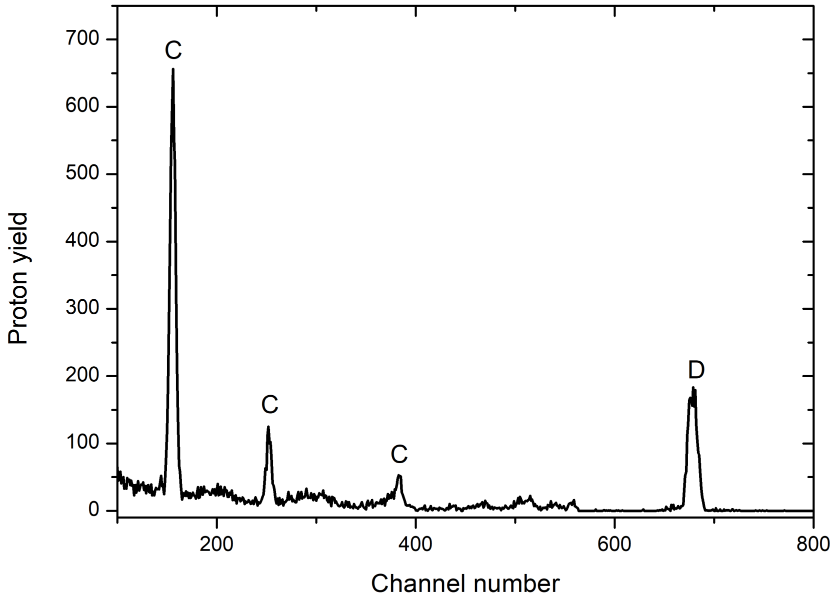

Figure 3.7: Spectrum of fast protons originating from nuclear reactions D(^{3}He,p)α, ^{12}C(^{3}He,p)^{14}N and ^{13}C(^{3}He,p)^{15}N, measured with 4.2 MeV ^{3}He ion beam on 275 nm thick a-C:D layer on silicon. Peaks are attributed to corresponding elements.

3.2 Sample Preparation

The sample preparation started at the IPP [65] where a block of fine-grain graphite was cut into sample size pieces. For laboratory experiments we decided on simple square blocks 15×16 mm^2 and 4 mm thick. For AUG they were cut into 12×33 mm^2 and 4 mm thick pieces with a special notch at the bottom. The notch, shown in Figure 3.8, enabled a secure mounting of samples into DIM-II manipulator plate inside the AUG [23]. All samples were polished to $R_\mathrm{a} \approx 5$ nm surface roughness.

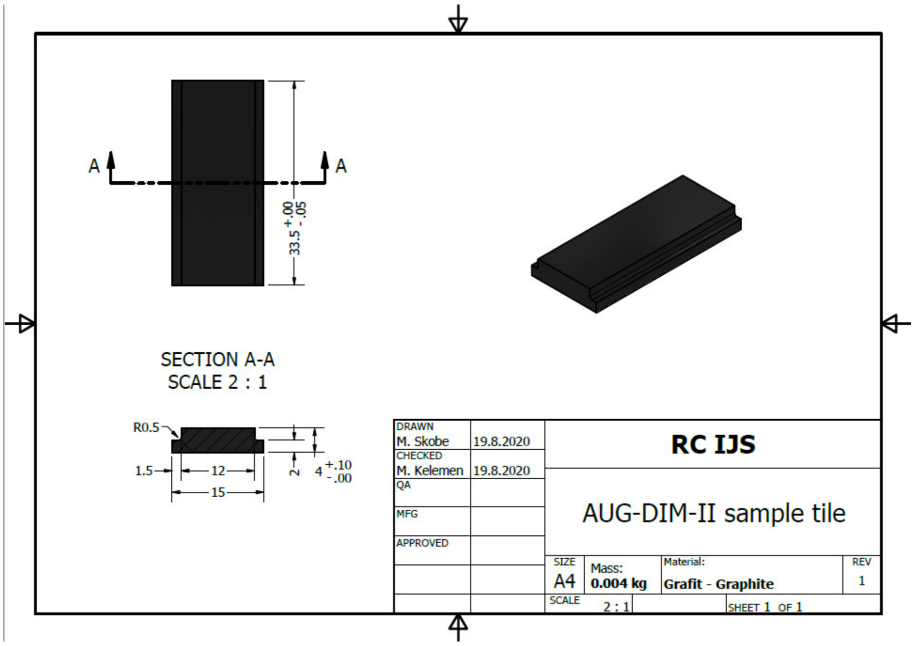

Figure 3.8: Technical drawing of graphite tile, to fit into the AUG-DIM-II manipulator. Drawing done by Matevž Skobe, JSI.

In future fusion devices the components which will suffer the highest particle loads will be made from tungsten. Molybdenum is not predicted as plasma facing components material, but it was used in our study for a specific reason: namely is the complexity of proposed study, in which we wanted to expose similar samples in controlled laboratory conditions as well to the real conditions in a tokamak, in our case in ASDEX Upgrade. As AUG is a full W machine, the deposition of W from other plasma-facing components is unavoidable. To be able to observe the sputtering in AUG, molybdenum as a proxy material for W was chosen. Both materials show similar behaviour for sputter yield under keV D ion bombardment, at least for smooth surfaces at 0° impact angle [19]. The main difference is in absolute values of the sputter yields and the sputter threshold energy. As absolute values are properties of material they are less important and we expect that they won't significantly affect results obtained with regard to roughness. The threshold sputtering energy can present a problem in tokamak experiment for quantifying results, yet the effect of the surface roughness should still be dominant in governing the sputtering behaviour.

Polished tiles were divided in three groups that underwent different surface treatments to produce different surface roughness before applying the Mo coating. Some tiles were further treated at IPP with sand blasting to produce surfaces with higher surface roughness > 1 µm. The sand blasting was performed with glass spheres and driving air pressure of 3 bar for short time. The short time was necessary not to introduce significant changes in substrate thickness. The achieved surface roughness was estimated to be 2–3 µm. The second group of substrate tiles was sent to ISTP [66] to be treated with plasma etching to increase the surface roughness. To produce samples with intermediate roughness the substrates were exposed to plasma consisting of mixture of CF_4 and H_2 gases at 9 Pa, driven with 13.56 MHz RF power supply. Samples were biased to 750–850 V and exposed to plasma up to 90 minutes: with longer exposure time the surface roughness is increased. A sketch of plasma etching apparatus is shown in Figure 3.9. The CF_4 and H_2 gases in the plasma generate F* and H* radicals. In reaction with graphite, volatile compounds are formed (C_xH_y, C_xF_y....), resulting in surface etching. At the same time a passivation layer (C_xF_y) can be deposited randomly on the substrate, obtaining an auto-masking effect against the etching. The passivation layer, however, can be (almost entirely) removed by the simultaneous ion bombardment (and the etching can proceed). The competition between passivation layer deposition and its removal by energetic ion bombardment results in a local variation of etching rate on the surface (over the process time) with a different local erosion [67].

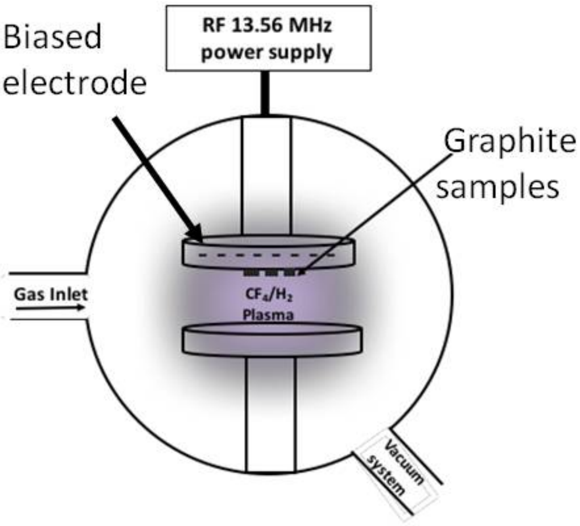

Figure 3.9: Schematic representation of plasma etching apparatus. Figure provided by E. Vassalo, Istituto per la Scienza e Tecnologia dei Plasmi CNR.

With this procedure we produced two sets of samples with $R_\mathrm{a} \approx 110$ nm and $R_\mathrm{a} \approx 280$ nm, as determined in AFM measurements. In figure 3.10 we see a graphite substrate before and after the plasma exposure. In AFM images the increase of surface roughness is clearly visible. The data from AFM were used to determine the surface roughness of samples. However, the AFM is limited with the maximum height that it can measure, usually around 1 µm. Thus, for the roughest samples we had to use confocal laser scaning microscope - CLSM to determine the surface roughness. The one example of CLSM measurement is in Figure 3.11, with the light image on the left and the height map on the right. Some of the graphite tiles, however, were left untreated, with only the initial polishing: they remain at the initial surface roughness of ≈ 5 nm.

After the surface treatment all the substrate tiles were send to Politecnico di Milano [41] where they were coated with thin film of Mo, around 115 nm in thickness. The tiles were inserted in a vacuum chamber together with Mo target. The chamber is coupled to a pulse laser, with fluence up to 15 J/cm^2 and wavelength $\lambda = 1064$ nm as shown in Figure 3.12.

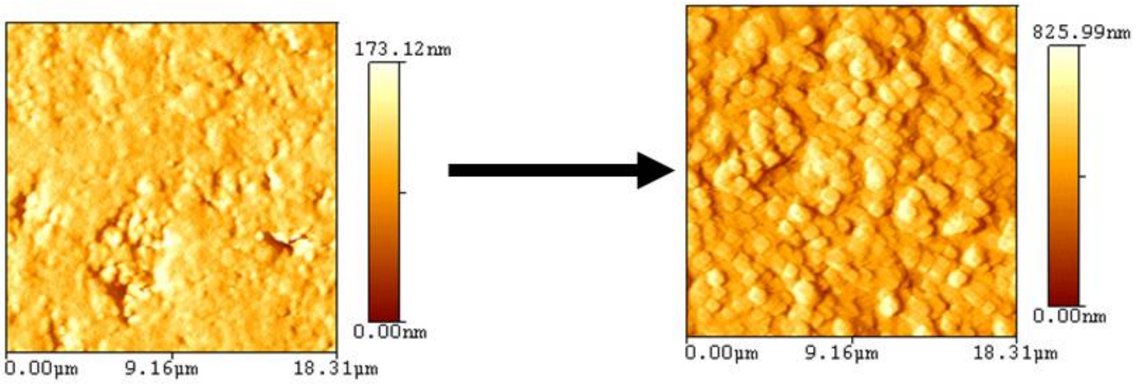

Figure 3.10: AFM images of graphite tiles before (left) and after plasma treatment (right). The increase of surface roughness can be easily observed. AFM images are provided from Espedito Vassalo from Istituto per la Scienza e Tecnologia dei Plasmi CNR, Milano, Italy.

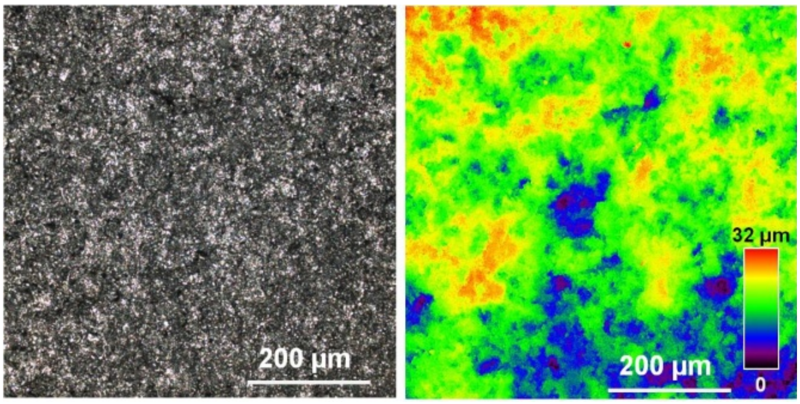

Figure 3.11: CLSM images of a sample with a surface roughness of $R_a \approx 2$–3 µm, already coated with Mo. Left is the composite light image of z scan, right is the height distribution of the surface.

The laser pulses ablate the surface of Mo target creating highly energetic Mo atoms that impinge on the surfaces of the substrate tiles. The deposition technique does not significantly change the surface morphology of the treated substrate while ensuring a good and uniform coverage of Mo over the entire sample surface even in the case of high roughness substrate [68]. Mo is deposited even in the deepest valleys on the surface, as seen in Figure 3.13. By optimising the number of laser pulses we were able to create an uniform coverage over the substrate tiles with Mo film thickness of 115–120 nm.

The prepared sample tiles were than analysed with scanning electron microscope (SEM) [69] and RBS to confirm the uniformity of Mo coating and provide base line data for sputtering study.

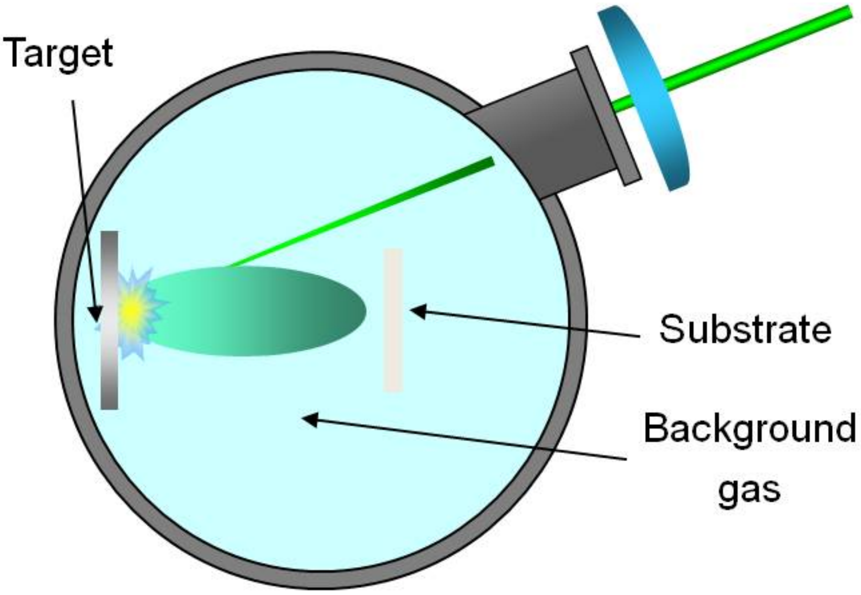

Figure 3.12: Schematic representation of pulsed laser deposition chamber, located at Politecnico di Milano, Italy. Figure provided by M. Passonni, Politecnico di Milano.

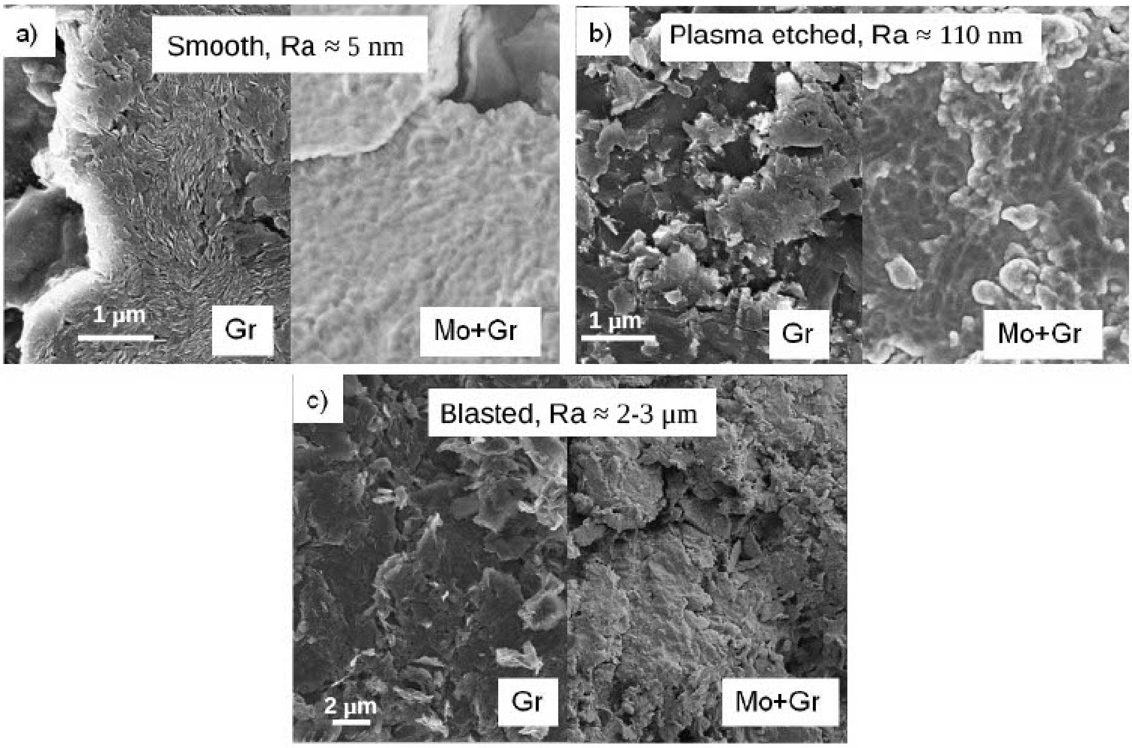

Figure 3.13: Scanning Electron Microscopy (SEM) images of secondary electrons from graphite sample tiles after surface treatment, to produce desired surface roughness (left) on graphite substrate (Gr) and after the deposition of ≈ 115 nm Mo coating (right). Figure a) samples with $R_\mathrm{a} \approx 5$ nm, b) samples with $R_\mathrm{a} \approx 110$ nm and c) samples with $R_\mathrm{a} \approx 2$–3 µm. Figure provided by M. Passonni, Politecnico di Milano.

3.3 Laboratory experiment

In the following section we will describe the laboratory experiment which was part of the study. There the focus will be on describing the Low Energy Ion Sputtering Apparatus - LEISA that was build at Jožef Stefan Institute, Ljubljana, Slovenia. A description of RBS measuring set-up and procedure for laboratory samples in given in this section.

3.3.1 Experimental Set-up

The whole experimental apparatus for D ion exposure is divided into three distinct parts. The first is the source for low energy D ions, the second is the holder for the sample mounting and monitoring of the ion current during the D ion exposure. The last is the supporting vacuum chamber. Together all three units are combined in Low Energy Ion Sputtering Apparatus - LEISA.

The in situ IBA - INSIBA vacuum chamber was used for LEISA. INSIBA is experimental end station located at Jožef Stefan Institute tandem accelerator laboratory [70]. And is usually used for in situ studies of hydrogen isotope migration in material. Photography of INSIBA chamber is shown in Figure 3.14.

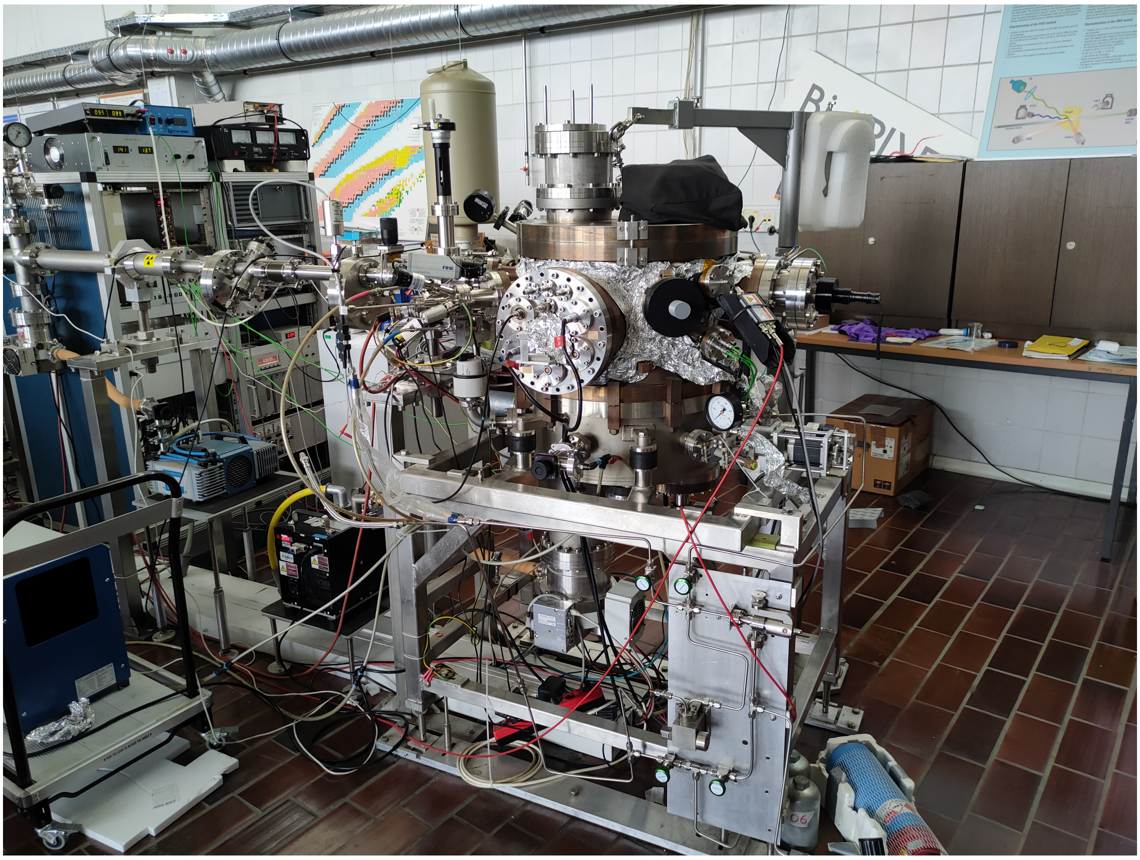

Figure 3.14: Image of INSIBA vacuum chamber with supporting vacuum system.

For LEISA set-up we used supporting vacuum system of INSIBA chamber, to evacuate the chamber and provide suitable conditions for D ion source operation. The vacuum system consists of Pfeiffer TMU 521 turbomolecular pump with pumping spead of 520 l/s [71] and NeoDry 15E Kashiama dry scroll prepump [72]. This vacuum system enables vacuum down to 10^{-8} hPa in INSIBA chamber. In addition, it can support the pressure increase during the active gas introduction into the ion source. We used a commercial Electron Cyclotron Resonance (ECR) ion gun IonEtch Gen II made by Tectra GmbH [73], equipped with ion beam collimator, discussed in detail in section 3.3.2. It was mounted on the side flange of INSIBA chamber with linear translator, shown in Figure 3.15.

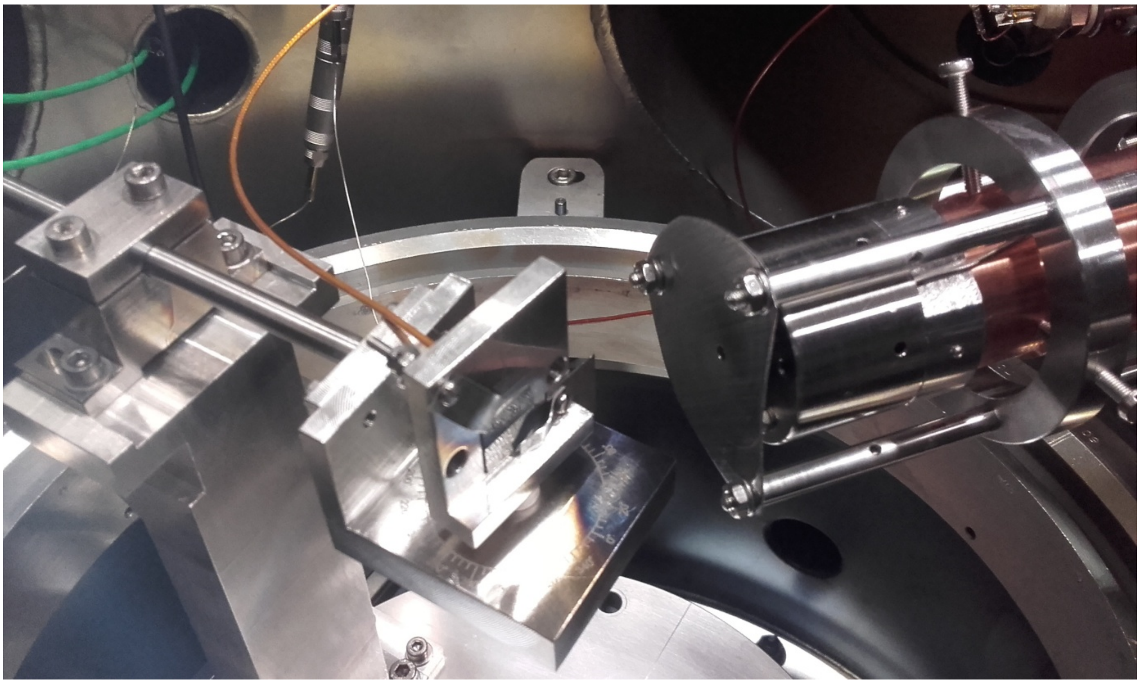

Figure 3.15: LEISA apparatus installed in INSIBA chamber.

For mounting the samples during the D ion exposure we constructed a rotating table that was fixed on an existing goniometer inside the INSIBA chamber. The technical drawing of the table is presented in Figure 3.16. This kind of construction was adopted to insure that the samples could be rotated for full ±90° with regards to the D ion beam direction. Special care was taken to design the table in such a way that the axis of rotation is on the surface of the sample. In addition, samples should be galvanicaly isolated from the ground of the experimental chamber. This isolation is important as samples were connected with the Keithley 2000 multimeter [74] to measure the D ion current on the sample. To reduce the emission of secondary electrons from the sample, it was biased by +100 V, as seen in Figure 3.17. The Keithley 2000 multimeter was connected to the computer and the current measurement was saved as a file with time stamps using custom written software in Labview [75]. Samples were held in place with two pieces of tantalum metal screwed in the supporting table. To prevent the sputtering of carbon substrate at higher angles and redeposition of carbon on the surfaces, a shield was designed to cover sides of the sample. The shield is presented in Figure 3.18 and is made of stainless steel.

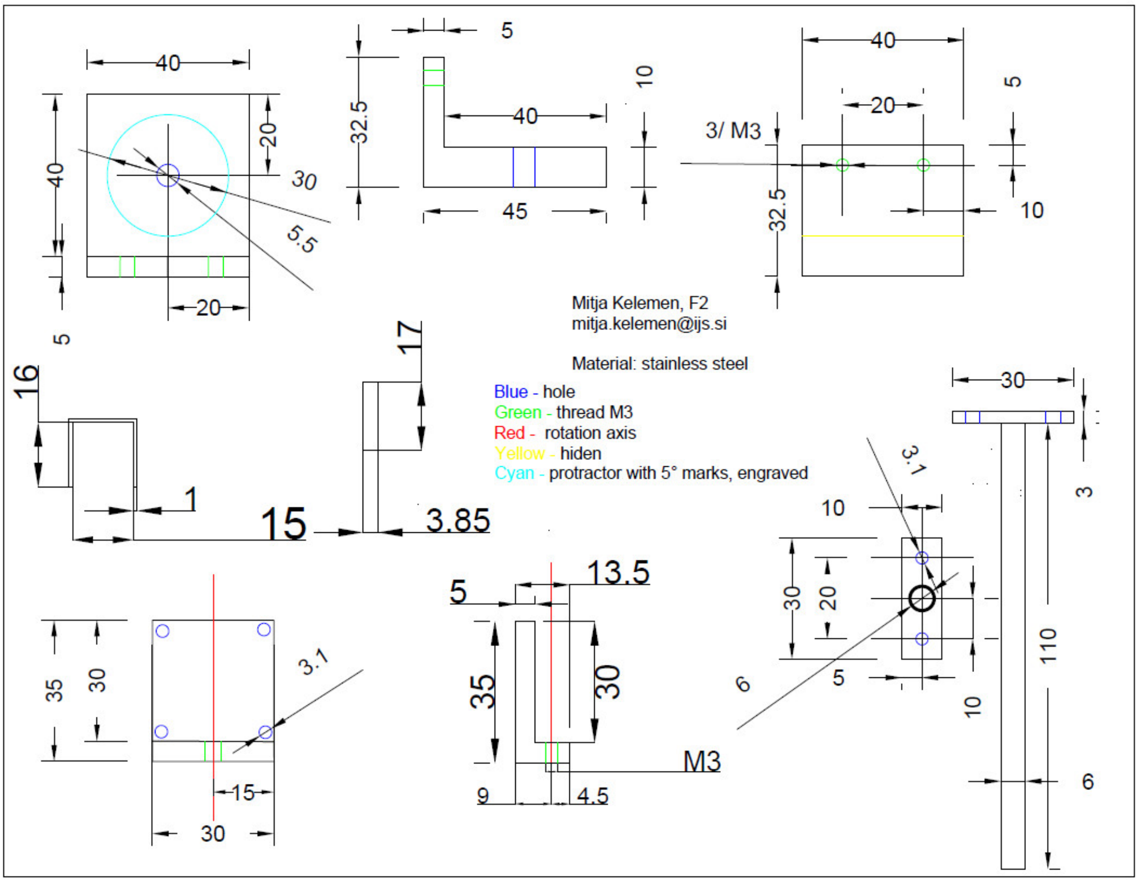

Figure 3.16: Technical drawing of rotating table and sample shield used in LEISA set-up.

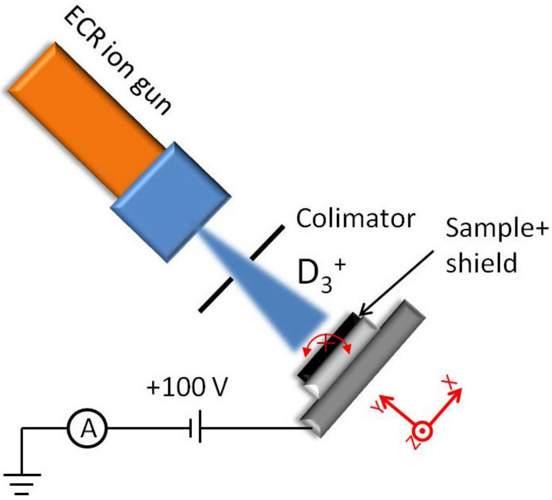

Figure 3.17: Schematic representation of LEISA set-up. Red arrows mark the coordinate system used in study and the red cross the axis of rotation for samples mounted inside LEISA set-up.

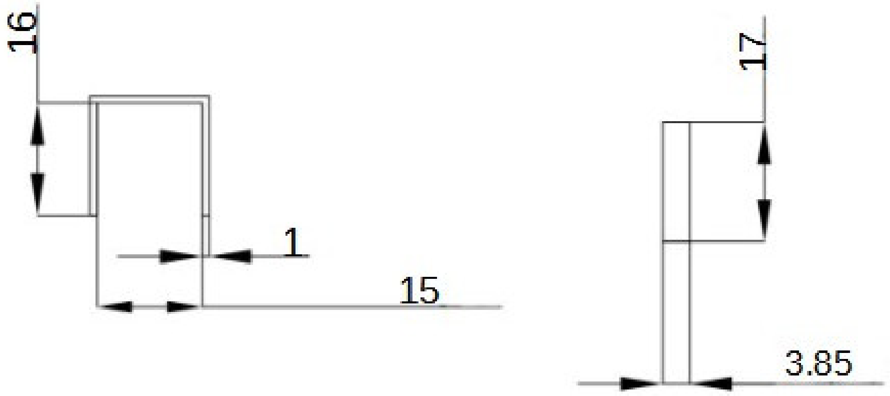

Figure 3.18: Technical drawing of sample cover shield.

3.3.2 Electron Cyclotron Resonance Ion Gun

Source of D ions in LEISA set-up is the commercial Electron Cyclotron Resonance (ECR) ion gun (IonEtch Gen II made by Tectra GmbH). The ECR consists of a microwave klystron operating at 2,45 GHz and power around 180 W. The klystron is coupled with a plasma chamber via wave guide. The plasma chamber is made of alumina surrounded with strong rare earth magnets. The magnets create a strong hexagonal magnetic field in which electrons are excited with microwaves. Mo extraction aperture of diameter 2.9 mm can be biased with 20–5000 V, which enables extraction of positive ion species from plasma. With such a construction the ion source can operate with highly reactive gasses as the operating temperature of plasma is low, in comparison with sources using filaments for electron emission to sustain the plasma. The gas supply to sustain the plasma should be from 0.01 to 100 sccm and is controlled by a leak valve [76].

ECR ion gun with such a construction has a large beam divergence, typically around 30°, full angle. It is slightly dependent on the extraction voltage, decreasing to 20°at 5 kV, according to the manufacturer specifications [76]. In order to provide high flux on the sample and not to miss it with part of the beam, two solutions are possible. One is to focus the ion beam with an einzel lens and the second one is to reduce the plasma chamber-sample distance.

First we installed an ordinary IonEtch Gen II ion gun to the INSIBA chamber. The short snout design, of 175 mm length [76], allowed mounting of the einzel lens. In this set-up the multicusp design of magnetic field in the plasma chamber is projected to the sample with einzel lens. In the first design of LEISA with a home made einzel lens install, a high flux could be obtained on the sample. The triangular shape of the focused beam is seen in Figure 3.19, of ellipsometry data on a-C:H thin film.

An a-C:H is a thin film of amorphous hydro-carbons deposited on silicon. This thin layer is easily eroded by low energy ions or atoms. In this way an erosion imprint of ion beam could be created in short time of exposure. In our set-up the D ion beam could be focused to a triangular shape of roughly 1 mm dimension.

As such small ion beam profile would complicate the analysis of samples we had to redesign the apparatus. A specially designed IonEtch Gen II ion gun with an elongated snout was procured. In this new design of IonEtch Gen II the snout length is 375 mm. Thus the sample to extraction electrode distance is reduced. In this configuration of the LEISA the extraction electrode is 33 mm away from the sample surface. This would create a beam of 18 mm in diameter on the sample position, taking into account the specified

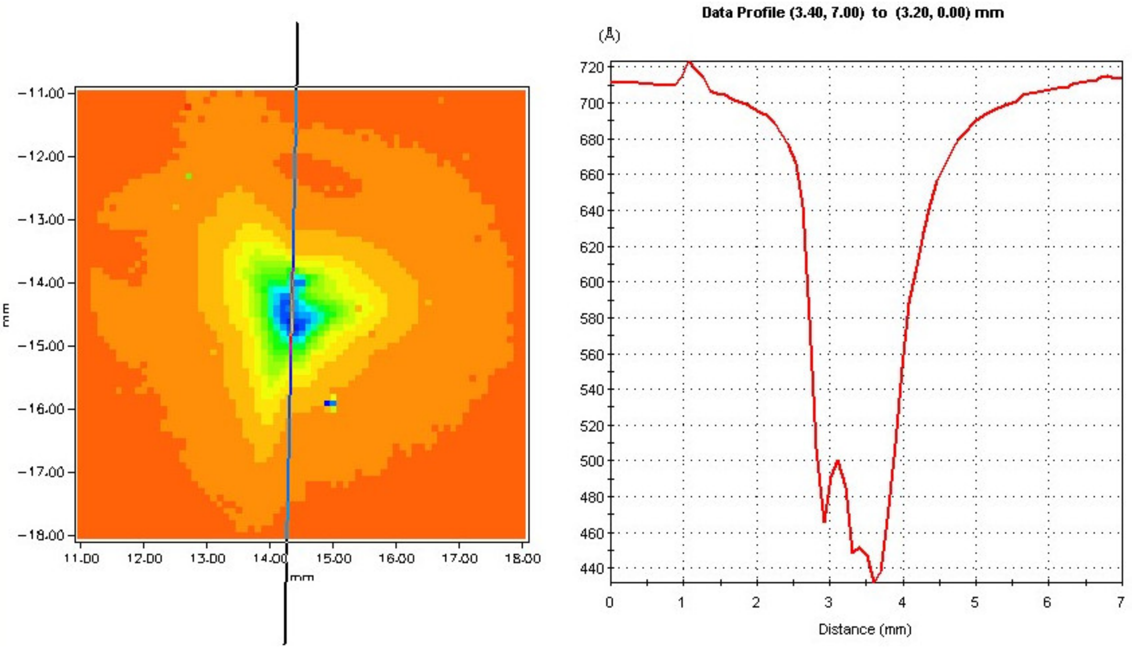

Figure 3.19: A 72 nm thick a-C:H sample after exposure to 1 keV Ar ion beam in LEISA at 0° for 15 min using an einzel lens for ion beam focusing. Left is the 2D map of a-C:H film thickness, on right the vertical cross-section of a-C:H thickness, along the line on the left image. Figure provided by Thomas Schwartz-Selinger, IPP.

beam divergence. This would mean, when tilting the samples, part of the beam would miss the sample and we would not have the complete reading of the ion current emitted from ECR. To avoid this we designed and installed the collimating aperture, made of Mo. It was mounted between the extraction aperture and the sample. The collimating aperture has the diameter of 2.7 mm and is positioned 28.2 mm away from sample surface. In this configuration we produce a beam of 9 mm in diameter on the sample surface. To position the aperture in front of the ECR ion gun we designed special aperture holder that can be positioned onto the snout of ECR ion gun and align it with the extraction aperture of ECR ion gun. In Figure 3.20 there are the technical specifications of aperture holder parts, and in Figure 3.21 the picture of assembly holder.

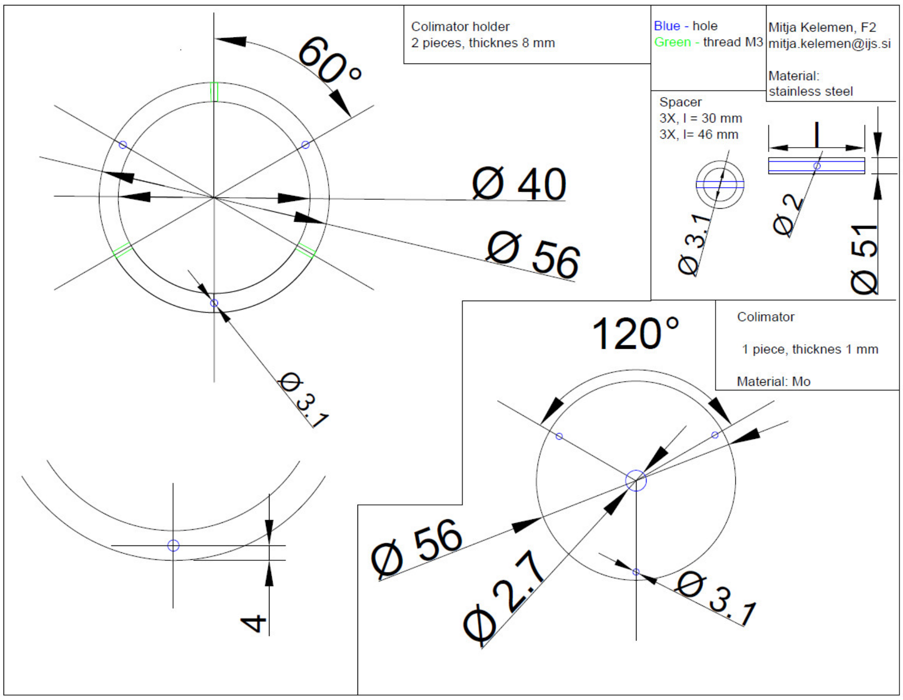

Figure 3.20: Technical drawing of collimating aperture and holder for ECR ion gun.

Figure 3.21: Image of assembled collimator and holder.

3.3.3 Ion Beam Characterisation

Characterization of ion beam exiting from ECR consist of two steps. The first step is characterization of extracted ion species. The second step is measuring the profile of the ion beam inside the vacuum chamber where the sample exposure takes place.

The ion species characterization was performed with help of colleagues from IPP. There we exchanged a duoplasmatron ion source at Bombardino experimental chamber with our ECR ion gun [77]. Bombardino chamber is equip with ion optics, which was used in the ion beam characterization. The ion beam from ECR ion gun was then focused with einzel lens and steered with x/y steers through a 60° magnet to a Faraday cup, measuring the total ion current. To perform the mass analysis, the exiting ion beam was steered into 60° bending electro magnet, to place the beam on a sample position inside of Bombardino chamber where ion current was measured. As charged particles feel Lorentzian force inside the magnet they are bended in radius:

$$r = mv/qB. \tag{3.25}$$

with m the mass of particle, v its velocity perpendicular to magnetic field B and q the particle charge. In the set-up the magnetic field inside the bending magnet is induced by electrical current running through coils. For the analysis 3 keV extraction voltage is applied. With changing the current in the coils mass analysis of the ion beam is performed. Ion beam current signal appeared at magnet currents corresponding to m/z values of 2, 4 and 6 amu/q, which corresponds to D^+ ion and D_2^+ and D_3^+ molecular ions, respectively.

The ion species distribution was measured in relation to chamber pressure and is shown in Figure 3.22. One can observe that all three ion species are present in the ion beam. The dominant is D_3^+, yielding 93 % of the total current on average. The contribution of D^+ remains fairly constant, around 3 % throughout the investigated pressure interval, we observe a decrease of D_2^+ species in proportion with increasing pressure. Maximum of ion current was observed at 1.5×10^{-4} mbar, where ion distribution consist of 93 % D_3^+, 4.6 % of D_2^+ and 2 % of D^+. We believe that the ion distribution depends mainly on the pressure inside the plasma chamber and is representative also for other applied acceleration voltages.

From the observed D ion beam behaviour we decided on the parameters to operate ECR for Mo sample exposure: pressure 3.0×10^{-4} mbar and extraction voltage 3.1 kV. With this parameters the dominant species was D_3^+, yielding 1 keV/D ion energy as we use +100 V biasing voltage on the samples.

Equipped with this knowledge we were able to perform the characterization of the ion beam inside the INSIBA experimental chamber. The geometry of the set-up is described in the section 3.3.1. For ion beam profile measurements the rotating sample holder was replaced with Faraday cup with 2 mm opening. Details of its construction can be seen in Figure 3.23. The Faraday cup was home designed to mimic the position of Mo samples during the D ion exposure at 0° on the mounting support. However the total mimicking was not possible, due to mounting issues. We ended up with reduced distance between the collimating aperture and opening of the Faraday cup. The distance was reduced from 28.2 mm to 20.2 mm. The full Faraday cup set-up was mounted on a linear vacuum manipulator with which the position dependent measurements of the ion current were performed. We measured the ion beam profile in z axis direction, as defined in Figure 3.17, without breaking the vacuum.

Ion current was measured with Keithley 2000 multimeter [74]. The obtained ion beam profile is presented in Figure 3.24. The measured profile can be sufficiently well described by a truncated Gaussian profile, as seen in Figure 3.24. The scattering of the measured ion current can be attributed to some backlash in the linear translator set-up. The fit is

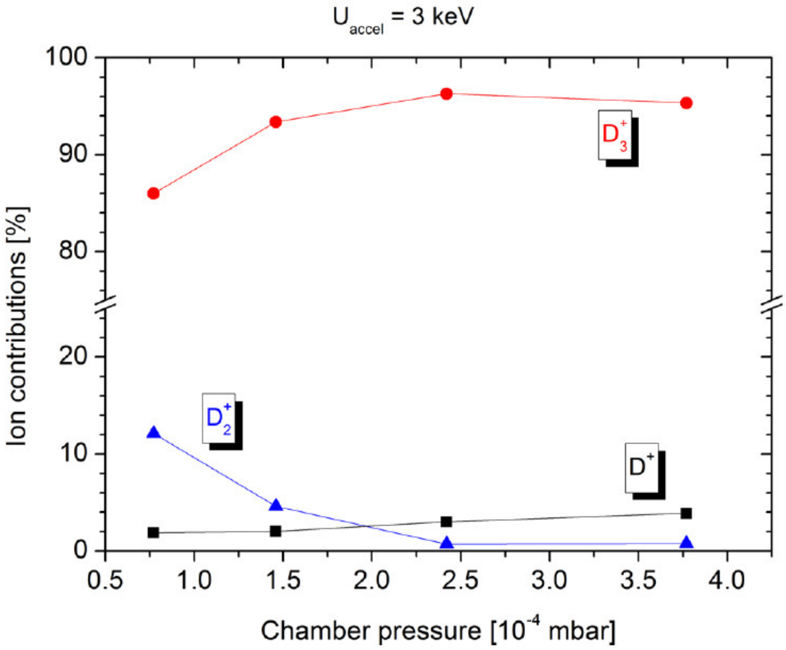

Figure 3.22: The distribution of D ion species versus chamber pressure for the ECR ion gun.

not of the whole Gaussian as the collimating aperture cuts the tails of the profile. Yet we measured 90 %, of the total measured ion current inside the beam diameter of 6.7 mm of the scanning interval. Taking into account the reduced distance between the collimating aperture and the Faraday cup aperture, the ion beam size on the position of the sample is calculated to 9.4 mm in diameter. If the Gaussian is fitted to the measured data we get the value of FWHM$= 7.3 \pm 3$ mm. The error is expected due to scattering of the current measurement, but the value of FWHM is still in the range of other estimations of ion beam spot size. The central beam flux of D ions was 8×10^{18} m^{-2}s^{-1}, as measured with the Faraday cup. By averaging the ion flux as measured by the Faraday cup over the entire irradiated area, the average D ion flux was around 3×10^{18} m^{-2}s^{-1}.

In Figure 3.24 we observe a drastic drop of the ion current at the position of +4 mm. The drop is an artefact: the linear translator reached its maximum position a slight rotation of the Faraday cup away from the ion beam direction caused a misalignment of the ion beam and the Faraday cup opening.

To check the actual size of the beam at sample position we exposed a thin film of amorphous hydrogenated carbon on silicon, a-C:H . The film was mounted in the same position as Mo samples. A 2-hour exposure to D ions was sufficient to erode the a-C:H layer to a significant degree leaving an imprint of the shape of the ion beam. Figure 3.25 is an image of the exposed a-C:H thin film, with beam imprint visible to the naked eye allowing the beam diameter to be measured. We estimated the diameter of the beam to ≈ 9 mm. The estimate is expected to be undershot, as the outer edge of erosion makes a smooth transition to non-eroded part and is hard to determine.

Both methods give a good agreement of D ion beam size, which we estimate to be 9 mm in diameter. This value was used to calculate the exposure fluence for all the exposed Mo samples in further experiments as we believe there is no significant change in beam shape during the exposures of different samples.

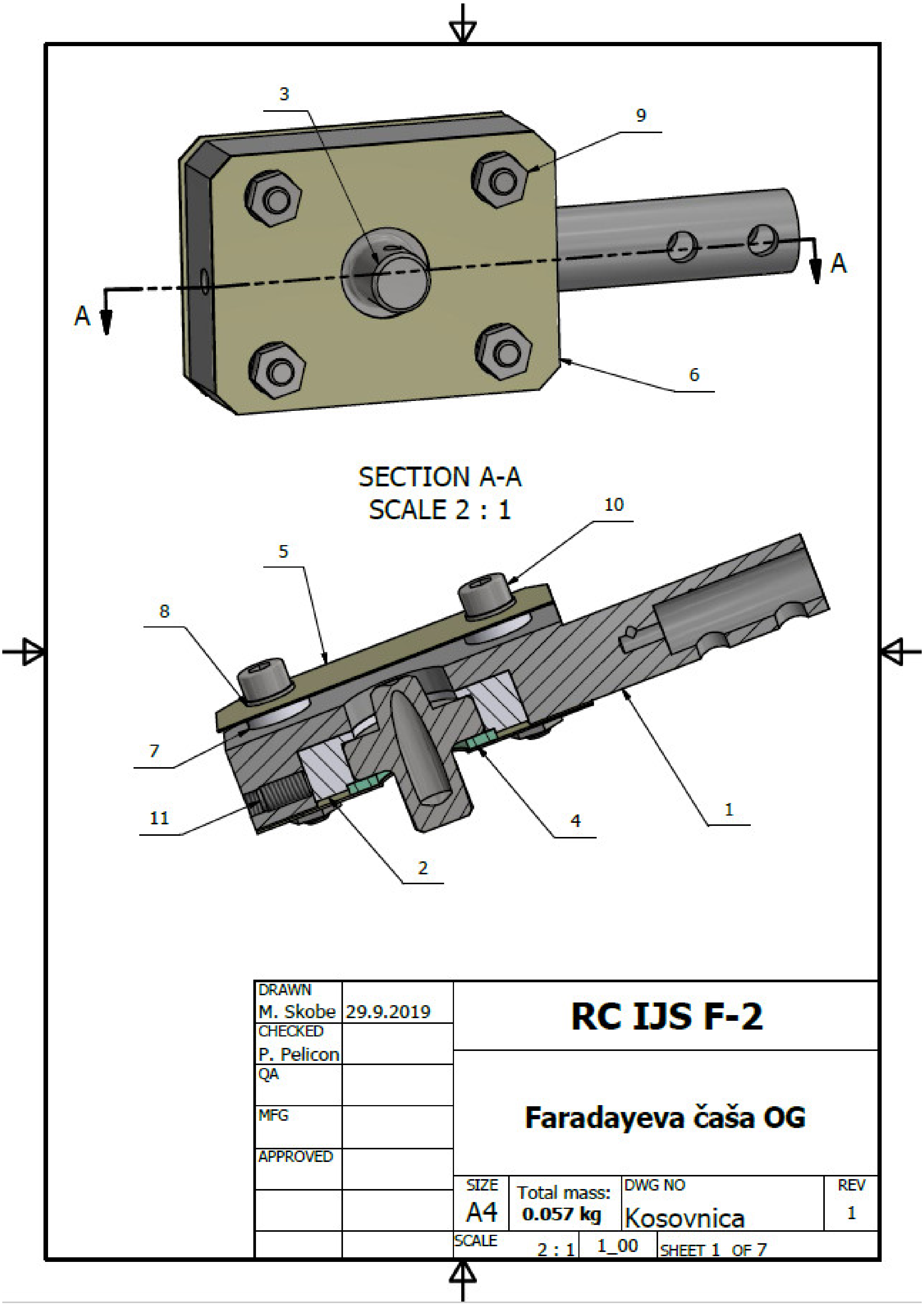

Figure 3.23: Design of the Faraday cup used for ion beam profile measurements. Drawing was provided by Matevž Skobe, IJS.

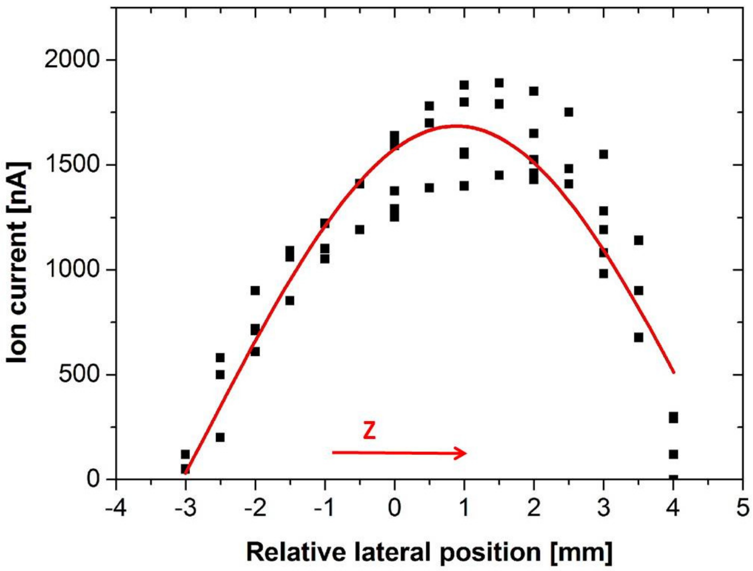

Figure 3.24: Vertical scan of ion beam current performed with Faraday cup.

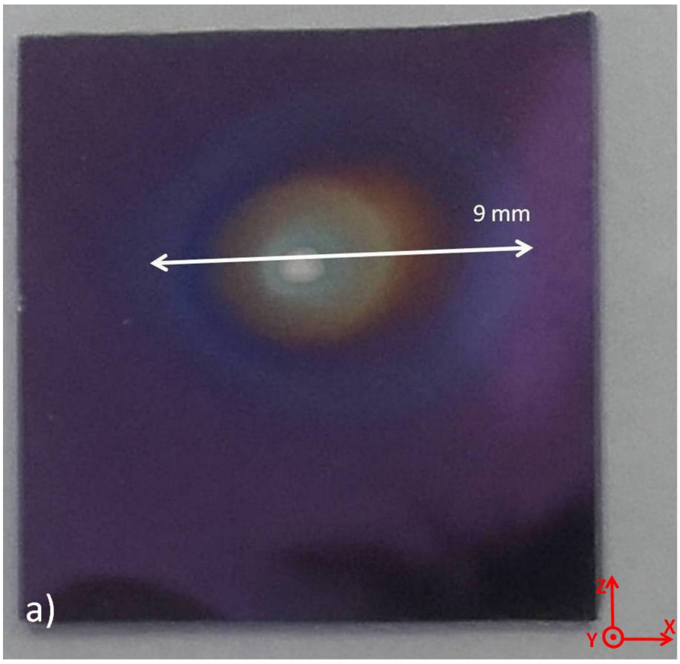

Figure 3.25: Photography of a-C:H after 2 h exposure to 1 keV/D ion beam. The erosion crater is visible.

3.3.4 Experimental Parameters for Laboratory Exposure

The total D ion current impinging on the samples was measured during the irradiation with Keithlly 2000 multimeter. The average fluence was calculated as:

$$F_{\text{average}} = \frac{3 \cdot I_{\text{D}} \cdot t}{S} \tag{3.26}$$

here I_{D} is ion current measured at the biased sample, t is the time of exposition and S the area of deuterium ion beam on the sample. The factor of 3 is due to the fact that predominant ion specie is D_3^+, neglecting the contribution of other two ion species. This is valid for the impact angle $\varphi = 0°$, where φ is defined as the angle between surface normal and the ion beam direction, schematically represented in Figure 3.26. The definition of the angle is similar to the angle α in the theoretical part of the study. Here φ is chosen to distinguish it from the angle of impact on the given point of the sample, which is α and is presented in the 1D theoretical model of sputtering.

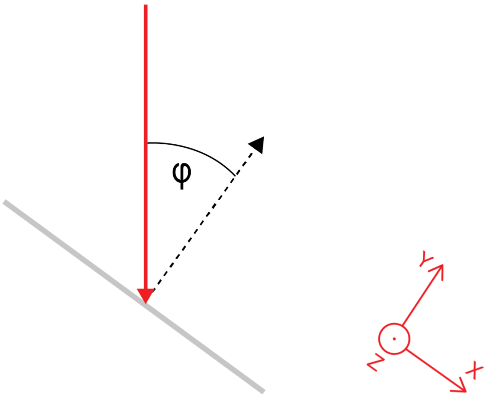

Figure 3.26: Schematic representation and definition of the angle of incidence φ in the laboratory system of the experiment.

If the surface of the sample is tilted, the circle is distorted to a shape of an ellipse, perpendicular to the axis of rotation. In our experiment the tilt was only on one axis of rotation. Thus the angular dependence of the beam area can be written as:

$$S(\varphi) = \pi r \cdot \left(\frac{r}{\cos\varphi}\right). \tag{3.27}$$

The $\cos\varphi$ comes from the projection of the ion beam on the surface of the sample in one dimension. Thus F_{average} can be written as:

$$F_{\mathrm{average}} = \frac{3 \cdot I_{\mathrm{D}} \cdot t}{S} \cos\varphi. \tag{3.28}$$

With the measured D ion currents the estimated time for each sample would be around 12 h to reach the desired average fluence. As we wanted to expose 16 samples and taking into account time needed for sample exchange we were forced to reduce exposure time for some samples due to limited availability of the INSIBA chamber for LEISA set-up. Furthermore, after obtaining the sputter data for the first few samples, the erosion was in the order of $1/3$ of the original thickness of the Mo layer. A concern was raised that for the intermediate roughness the amount of sputtered material could change surface morphology of the sample. So we reduced the exposure time to the level to achieve roughly $1/10$ erosion of the original Mo layer thickness.

Average fluence is a good measure when discussing the condition to which samples are subjected. However, from the shape of D ion beam and in combination with the lateral resolution of RBS measurement, discussed in the next section, the average fluence is not practical for calculation of sputter yield. Therefore we define maximal fluence on the sample: F_{max} is the fluence in the centre of D ion beam on the circular area with 1 mm in diameter. F_{max} can be calculated from F_{average}, for our set-up we obtained relation:

$$F_{\text{max}} = 2.7 \times F_{\text{average}}. \tag{3.29}$$

Here the factor 2.7 is obtained from the ratio of the above obtained maximum and average D fluence as measured by the Faraday cup. F_{max} and the point with the highest measured erosion by RBS then serve as inputs for sputter yield calculation.

3.3.5 RBS Measurments Set-up

For RBS analysis of laboratory samples we used INSIBA experimental chamber, coupled to 2 MV tandem accelerator at Jožef Stefan Institute [70]. For RBS measurements we used Passivated Implanted Planar Silicon (PIPS) detector [56] with circular aperture $\Phi = 5.7$ mm yielding the solid angle of 0.689 msrad positioned at $\Theta = 165°$ scattering angle. The schematic representation of the RBS measurement set-up is shown in Figure 3.27, while the top view with an installed carousel for batch sample analysis is presented in Figure 3.28.

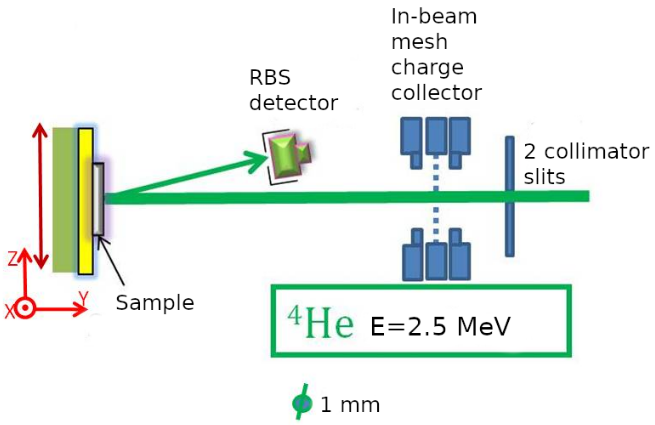

Figure 3.27: RBS set-up used in INSIBA end station at Jožef Stefan Institute.

The deposited dose of ^{4}He ions was controlled by integrating the charge on a mesh charge collector mounted between the collimating slits and the sample. With the ^{4}He probing beam we performed lateral scan in the middle of the sample in direction of the rotation axis, to avoid geometric effects of the D beam projection on the sample at different impact angles. For the analysis we used a probing beam with a diameter of $\Phi = 1$ mm and E=2.5 MeV ^{4}He ions. The RBS measurements were performed in 2 mm lateral steps.

To find the spot of maximum erosion on the sample, to be correlated with maximum flux in the D ion beam profile, a series of 5–6 measuring points, along the rotation axis of the sample was made. The exact number of spots depended on exact positioning of the sample to the sample holder, due to limited lateral movements of vacuum goniometer. The schematic layout of measuring points is shown in Figure 3.29.

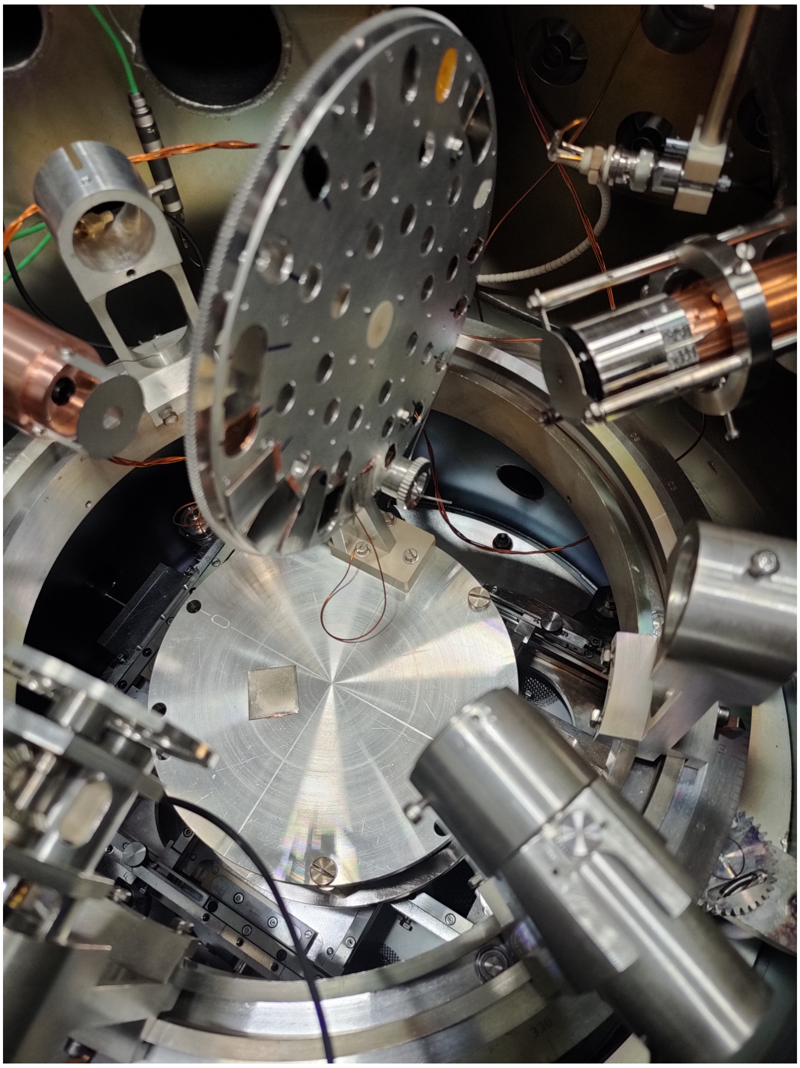

Figure 3.28: Top view of INSIBA chamber as used for RBS analysis of samples used in the laboratory experiment with sample mounting carousel.

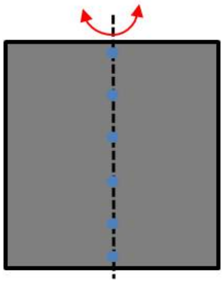

Figure 3.29: Schematic representation of RBS measuring points on samples used in laboratory experiment.

3.4 ASDEX Upgrade Experiment

Samples with different surface roughness were exposed in ASDEX Upgrade - AUG tokamak by use of DIM-II manipulator. The experiment was performed under the task T19 of MST1 (medium size tokamak 1) group of EUROFUSION, plasma facing components work package. For this experiment we got granted eight deuterium L-mode plasma discharges in AUG tokamak [21]. The experiment took place during the discharges 35609 to 35617. The discharges were carried out in low confinement mode (L-mode) in deuterium. Each discharge lasted for 6 s. During the session we experienced one misfired discharge, without plasma ignition. In Figure 3.30, the essential tokamak parameters are presented, for two different discharges, namely from top to bottom the time dependences of electron density, plasma power, electron temperature and position of OSP.

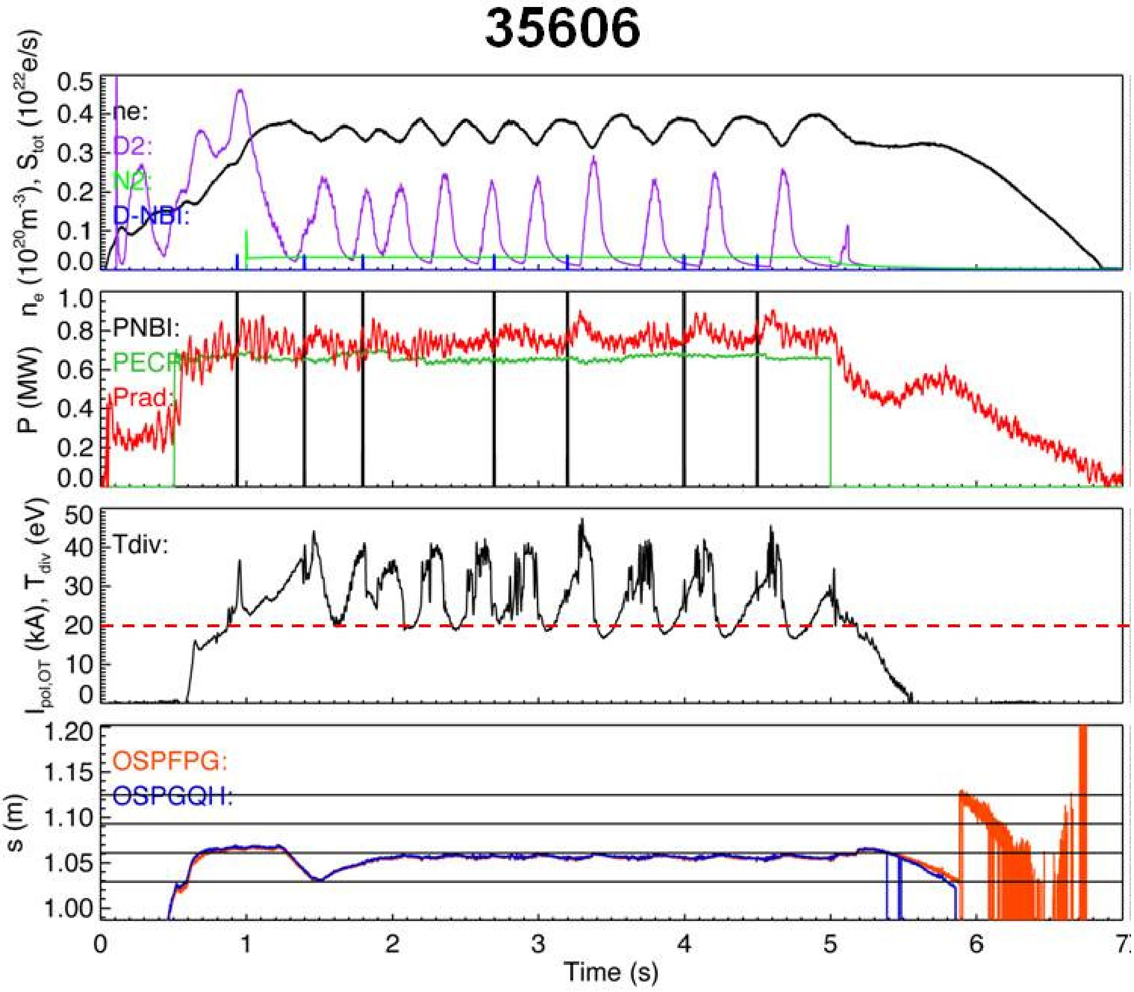

Figure 3.30: Parameters of plasma during the discharges no. 35606.From top to bottom: electron density, plasma power, plasma current and position of OSP. Plot was provided by Karl Krieger, IPP.

AUG is a large scientific equipment, and parallel running of several experiments is encouraged. Together with surface roughness erosion experiment several others were carried out. During our discharges plasma was seeded with ^{15}N. Nitrogen is introduced in tokamaks, to enhance radiative cooling of plasma in the separatrix region of tokamak [78] thus changing the heat flux in outer divertor. Usually ^{15}N is used, as it allows post-mortem analysis of its interactions with plasma facing materials by use of IBA via the nuclear reaction analysis. In addition to ^{15}N seeding we mounted a set of marker samples with gold spots on the DIM-II tiles to study the material transport after the erosion.

Comparing the AUG to the laboratory experiment, one additional complication is the ion flux distribution at OSP. In Figure 3.31 the distribution of particle flux is shown for the entire DIM-II tile in poloidal direction. The first observation is that average flux exponentially decays with increasing distance from OSP. On top of this, individual measuring points of the ion flux have quite large spread. In the same figure the position of individual sample tiles against the ion flux is also visible.

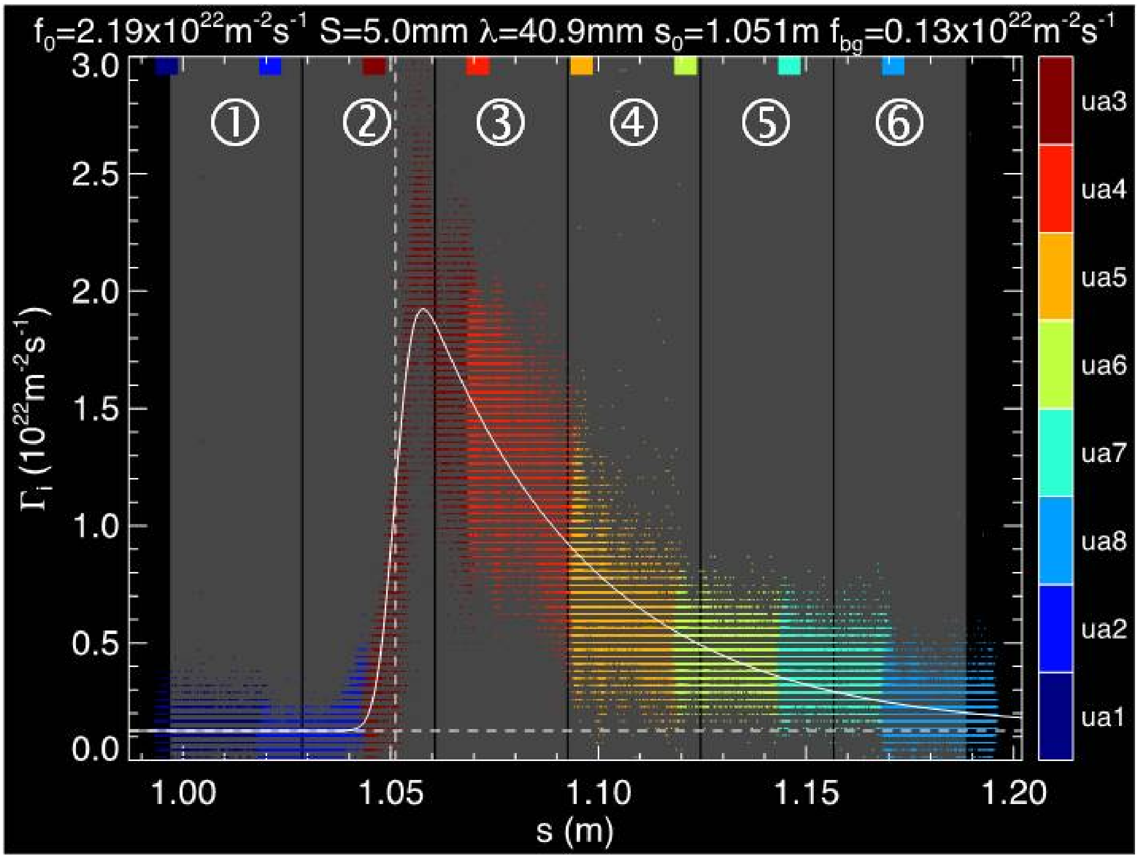

Figure 3.31: Particle flux distribution during a plasma discharge in AUG. The vertical dashed line indicates position of OSP. Plot was provided by Karl Krieger, IPP.

Together with high particle flux the samples in AUG also experienced high heat flux, measured during the experiment. The distribution of heat flux can be seen in Figure 3.32. Heat flux distribution at two times in one discharge is shown. We can observe the decrease of heat flux with time, despite the constant electron density and plasma power. This is due to the significant energy loss through the radiation, the effect of N seeding of plasma.

Although the cooling effect of N is significant, the samples exposed in OSP have been heated up for around 500 K, which meant that sputtering took place at 800 K, as the samples were at room temperature before discharges. The exact temperature during sputtering is just an estimate, as we were not able to measure the temperature in-situ. This heating represents a significant difference compared to laboratory experiment, where the samples were heated only a few tens of K above room temperature. Important characteristic for erosion studies in tokamaks is the angle of incidence of particle in the divertor region. The

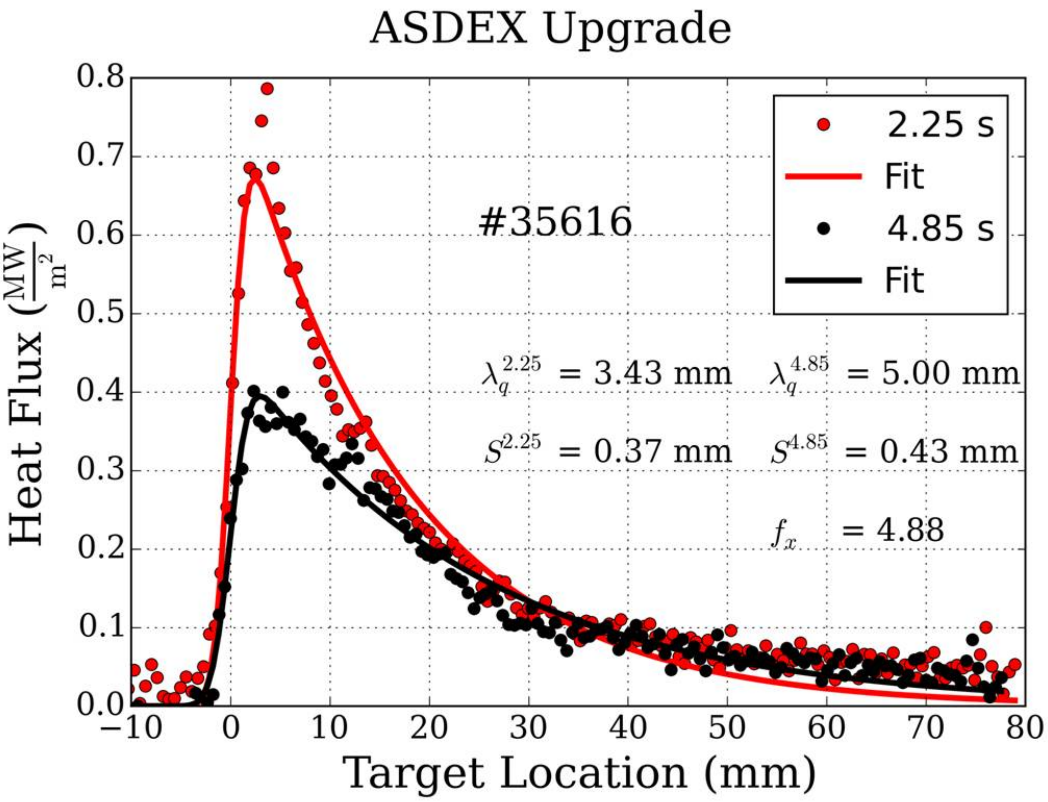

Figure 3.32: Scan of heat flux in divertor region of AUG during the discharge no. 35616. The scan runs in poloidal direction. Plot was provided by Karl Krieger, IPP.

magnetic field lines enter at the surface of divertor at shallow angles, ≈ 60°. Since the charged particles are guided along these lines the expected angle is close to 60°. However, the stray fields close to the surfaces can alter the trajectories of individual particles. Consequently we end up with a distribution of impact angles in OSP which are hard to predict and can only be modelled to a certain degree.

3.4.1 Experimental Set-up in AUG

The samples were mounted in AUG-DIM-II tiles (DIM tiles), blocks of W roughly 20 × 8 cm^2 in size [23], featuring two rows of grooves for hosting six sample tiles, of AUG geometry shown in Figure 3.8. When DIM tiles are mounted in the divertor of AUG the rows are parallel to the poloidal direction of AUG. For roughness erosion experiment we were allowed to fill two rows with our tiles, one per each DIM tiles, while the other two rows were filed with Au marker samples, to study net erosion and deposition patterns in the divertor region. As the positioning of OSP in AUG is quite precise, we decided to mount samples with different surface roughness on both sides of OSP. The samples at positions 2 and 3 on DIM tile were closest to OSP. One pair contain samples with $R_a \approx 5$ nm and $R_a \approx 2$–3 µm, and the other pair $R_a \approx 110$ nm and $R_a \approx 280$ nm. Also the position 4 in DIM tile was filled with surface roughness samples, while positions 1, 5 and 6 were filled with dummy tiles. As dummy tiles we used the same graphite substrate as for samples with $R_a \approx 5$ nm, except that the Mo coating was made with magnetron sputtering, which gave us less control on the thickness of coating and surface morphology. In Figure 3.33, the schematic positioning of tiles in DIM tiles is given, with naming of the samples in Table 3.1. The photograph of mounted tiles is shown in Figure 3.34. The photo was taken before and after the exposure in AUG tokamak plasma. In figure 3.34 we can clearly see the discolouration of gold spots on the marker samples. This discolouration is due to W deposition, to be discussed in the result section.

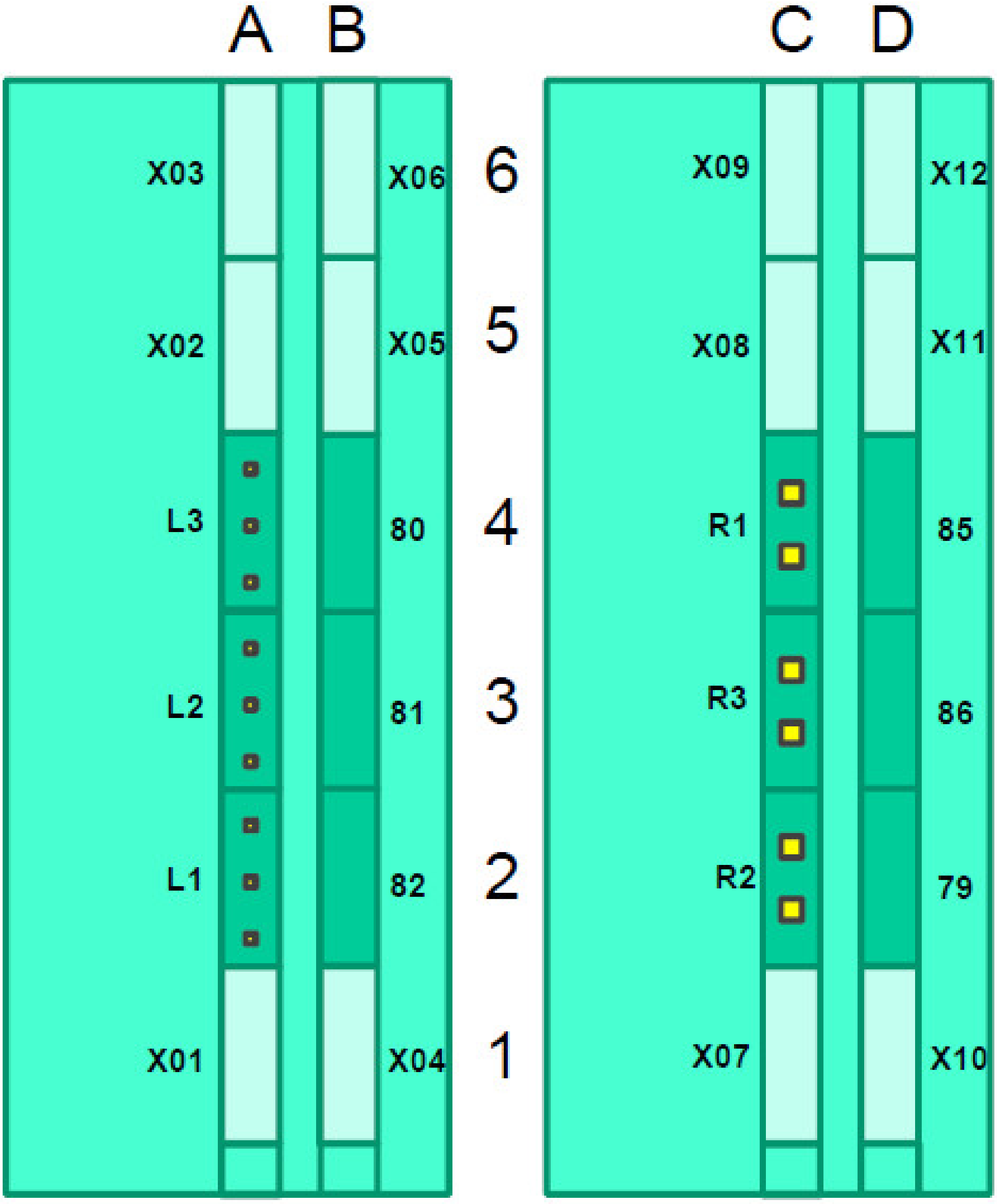

Figure 3.33: Positioning of sample tiles into DIM-II tiles. Figure was provided by Karl Krieger, IPP.

Position	Row	Name	Surface roughness R_a
6	B	X06	Dummy
5	B	X05	Dummy
4	B	Mo 80	110 nm
3	B	Mo 81	110 nm
2	B	Mo 82	280 nm
1	B	X04	Dummy
6	D	X12	Dummy
5	D	X11	Dummy
4	D	Mo 85	2–3 µm
3	D	Mo 86	2–3 µm
2	D	Mo 79	5 nm
1	D	X109	Dummy

Table 3.1: Naming and positing of roughness samples into DIM-II tiles of AUG experiment.

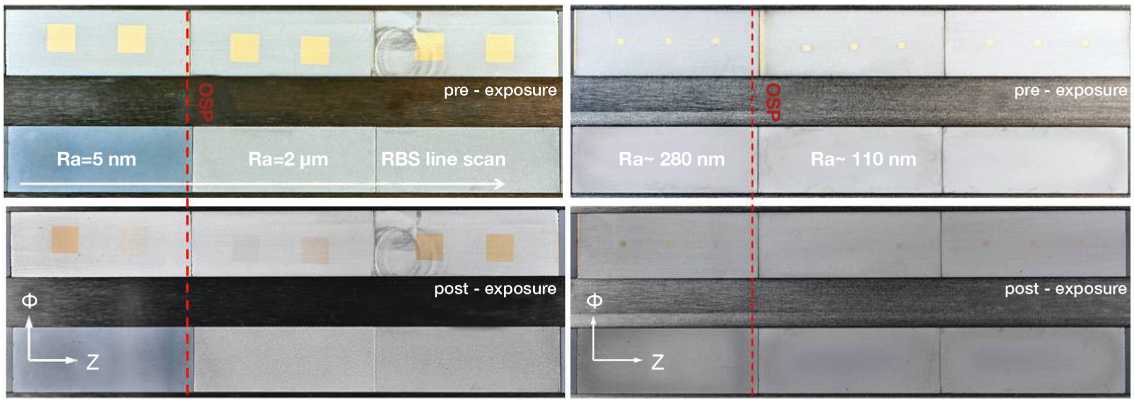

Figure 3.34: The photographs of mounted sample tiles, in the vicinity of OSP, before and after exposure to AUG plasma. Picture was provided by Karl Krieger, IPP.

3.5 SDTrimSP Simulations

Nowadays computer simulations are valuable tool in understanding the process in complex physical systems. In the past 50 years or so, many codes have been developed to describe interactions of ion bombardment with targets [79]. One of the more developed codes is SDTrimSP [79]. The SDTrimSP is based on two older codes TRIM [80], for static calculation and TRIDYN [81], [82], for dynamic calculations. The codes are performing Monte-Carlo calculation in binary collision approximation. This means that ion collides with nuclei of target atoms and is recoiled. In this collision the momentum and energy of both particles are conserved. After the collision the ion travels in a straight path to the next nucleus. During this travel the ion losses energy due to electronic stopping power. Nowadays codes also follow the recoil atom from the collision which is used for defect and crystal lattice damage calculations. The latest version SDTrimSP is version 6.0, currently maintained by Andreas Mutzke, Max Planck-Institut für Plasmaphysik, Greifswald, Germany. SDTrimSP is a complex code, with vast array of calculation possibility. However, majority of them are not used in sputter yield calculation. Therefore we will only describe here some basic concepts that are needed in understanding of the sputter yield calculation.

3.5.1 Principles of Calculation

All computer codes are merely an approximation of real physical processes describing the physical world with more or less simplifications. One of the starting assumptions in SDTrimSP is that target is amorphous, infinite lateral size and at 0 K. This means that all the atoms in the target have well defined positions and initial velocity $v = 0$. In the first order approximation the interaction between ion and target nucleus is Coulomb interaction. However, this turns out as a poor approximation, as surrounding electrons significantly change the interaction potential. While there are loads of different models that describe this interaction, the goal of all is to provide a tool for calculating the scattering angle of the moving ion and the recoil angle of the target atom [79]. SDTrimSP comes with a vast library of tabulated target and ion parameters which are important parameters in calculation. The parameters include atomic numbers and masses of involved elements and their density in all states of matter. In damage calculations the important parameter is the displacement energy of an atom in the target, which is not to be confused with surface binding energy E_s, the energy required to knock atom off the surface. Thus, the E_s is one of the most important parameters in calculating the sputter yields [38]. SDTrimSP is a numerical calculation method which tracks the history of events, as schematically represented in Figure 3.35. In the input file you have to define the integration method, how far to follow the recoils, frequency of data output writing ... All this is chosen on what type of calculation is performed and what computer hardware is available for calculation. Due to relatively simple computational operations SDTrimSP can be run with sufficient speed on most personal computers.

This simplified description is given for the core of SDTrimSP code, which runs in 1D model. In this model we cannot take into account the surface features, which can affect net erosion of the surface, directly influencing the calculated sputter yield as defined in the theoretical part. To this end in latest years a development of 2D [83] and 3D [84] code has been under way. While the core and physical approximations are still the same as in 1D code the expansions are able to take into account the surface morphologies of the simulated surfaces.

The first simulation of Mo sputter yield were performed with 1D code, which is easy to use and can be run on every personal computer. It was expected that 1D would describe the sputter yield sufficiently well for smooth samples ($R_\mathrm{a} \approx 5$ nm). It turned out that

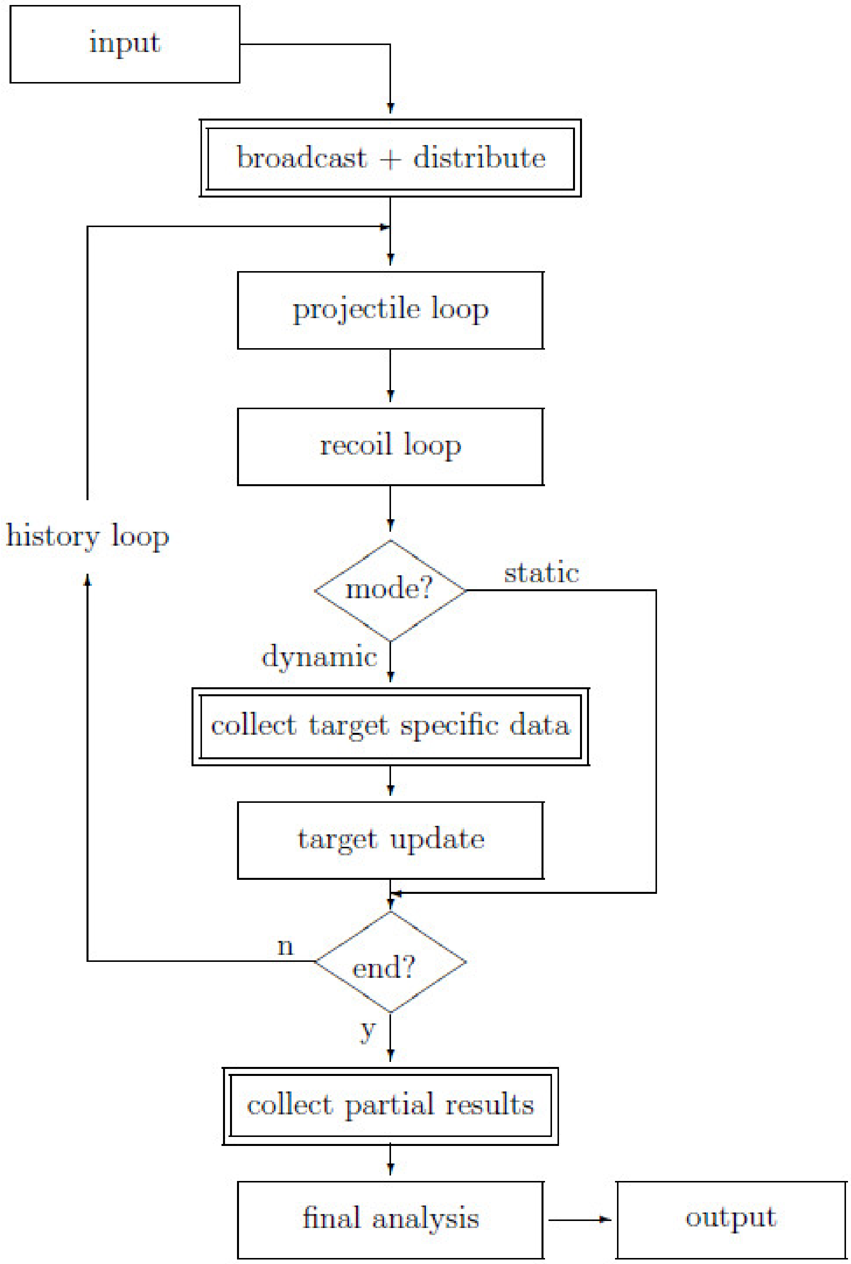

Figure 3.35: Main block flow chart of the SDTrimSP code. Taken from IPP 2019-02 [79] .

when dealing with realistic macro samples the 1D approximation does not provide good agreement with experiment. In spite of its limitations the exploration with 1D code still provided an important insight on angular behaviour of sputter yields. This was later utilised in simulation with SDTrimSP 3D code. As it is a complex code for use, and in addition the cluster computational power is required, we asked the developer of SDTrimSP 3D code Andeas Mutzke, to help with the calculation. All the details of calculation are described and discussed in the results chapter in section 4.4.

Chapter 4

Results and Discussion

In the following chapter we describe the results obtained in the study, divided into three sections. In the first section the focus is on the laboratory part of the study, where a detailed description of the obtained results is given, with a short discussion. In the second part the results from the experiments performed in ASDEX Upgrade tokamak are presented, with the discussion and comparison to the laboratory results. In the third part the results from simulation with SDTrimSP are presented. A detailed comparison to the laboratory results is also given.

The results from all three parts of the study are complementary. At the end of the chapter, a summary and a detailed comparison of all results is given.

4.1 Laboratory Experiment

Samples presented in section 3.2 were exposed to the ion beam with energy of 1 keV/D at 300 K. They were irradiated with maximal deuterium fluence at the exposure spot ranging from 0.85 to 3.29×10^{23} m^{-2} at different impact angles of $0° - 70°$. A detailed list of individual parameters for each individual sample is given in Table 4.1.

There is some evidence of fluence dependent sputter yield, for iron under D ion irradiation [85], but this is only noticeable at fluence below 10^{22} ions/m^2, contributed to the oxide formation on the surfaces. For pure elemental surfaces the threshold fluence should be even lower, as shown for the pure iron targets [86]. For this reason, we believe the difference in exposure fluence applied in our experiment on different samples should not affect the obtained sputter yield values. The crieria of 1/10 of erosion of Mo layer is still sufficient to reach more than 10^{22} ions/m^2 fluence on samples, avoiding concerns of fluence dependent sputter yield. For each set with different surfaces roughness, we exposed four samples at different incident angles: 0°, 40°, 60° and 70°. The angles were chosen on the basis of literature reports for different material and SDTrimSP simulations [19], both of which predict increase of sputter yield at the angles $> 60°$ with some indication for rougher surfaces even for angles below 60° [37], [84].

4.1.1 RBS Measurements

The main tool for determining the thickness of Mo layer before and after the exposure to D ions was RBS. Our samples consisted of bulk carbon substrate with approximately 115 nm thick layer of Mo. An example of the measured spectrum is shown in Figure 4.1, where a clear difference of Mo signal before and after D ion irradiation can be observed.

The spectra were analysed with SIMNRA 7.5 software [87], by modelling of the RBS spectra. For laboratory samples a two-layer target was sufficient to describe the measured

Sample	Treatment	R_a [nm]	Angle [°]	Max. Fluence [$\cdot 10^{23}$ $1/m^2$]	Exposure [h:min]
Mo061	Polishing	≈ 5	0	2.67	10:15
Mo062	Polishing	≈ 5	40	3.19	9:00
Mo063	Polishing	≈ 5	60	2.53	11:17
Mo064	Polishing	≈ 5	70	1.39	9:03
Mo065	Plasma etching	≈ 110	0	2.46	4:00
Mo066	Plasma etching	≈ 110	40	1.84	4:00
Mo067	Plasma etching	≈ 110	60	1.27	4:00
Mo068	Plasma etching	≈ 110	70	0.86	4:00
Mo070	Plasma etching	≈ 280	0	2.46	4:00
Mo071	Plasma etching	≈ 280	40	1.76	4:00
Mo072	Plasma etching	≈ 280	60	1.32	4:00
Mo073	Plasma etching	≈ 280	70	0.89	4:00
Mo076	Sand blasting	2–3 µm	0	0.85	7:00
Mo075	Sand blasting	2–3 µm	40	1.25	7:00
Mo074	Sand blasting	2–3 µm	60	1.92	7:00
Mo059	Sand blasting	2–3 µm	70	2.5	7:00

Table 4.1: Exposure parameters for each individual sample. All samples were exposed to D ion beam with energy of 1 keV/D at 300 K. Listed are the sample name, treatment of the substrate surface, estimated surface roughness, angle of incidence of D beam, the maximal fluence over the sample irradiated area and the time of exposure.

spectra with great accuracy, while for AUG samples additional structures had to be introduced in order to describe the RBS spectra obtained on the samples after the exposure. This will be discussed in detail in AUG result section.

The surface roughness affects the shape of the isolated Mo peak. It is addressed in SIMNRA fit with a layer roughness model [88]. The actual value of surface roughness was selected to get the best fit of the Mo peak for the virgin sample. The same value was then used to fit the sample after the D ion exposure. The effect of roughness is visible in Figure 4.2. The Mo peak gets an increasing low energy tail with increasing surface roughness. The peak height is decreased, while the peak integral remains the same.

4.1.2 RBS Measurements Results

The first RBS measurements were made on virgin samples i.e. before exposure to the D ion beam. The objective of these measurements was to check the uniformity of Mo layer thickness. The layer thickness was measured at five points along the z axis of the sample. The profiles of the Mo layer are shown in Figure 4.3 of samples for the different surface roughness.

The thickness of the virgin Mo layer is within 10 % of the nominal thickness of 7.4×10^{17} 1/cm^2, which can be transformed into thickness of 115 nm taking Mo density of 10.210 g/cm^3 [87]. This value is given as an orientation since the samples do have some variance in thickness and a gradient along the sample, as seen in Figure 4.3.

After the exposure to D ions the RBS measurements are repeated. This allowed us to obtain the profile of the erosion crater, for each individual sample. One example is shown in Figure 4.4 in the vertical profile scan of the nominal Mo layer thickness before and after the D ion exposure as measured by RBS. In addition to the RBS measurement, a Gaussian

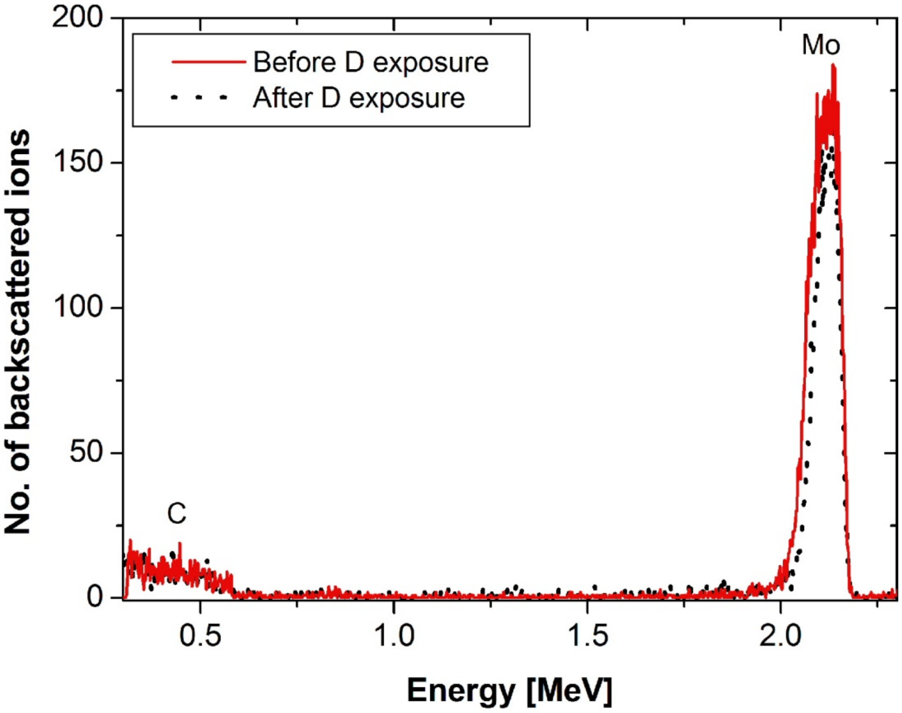

Figure 4.1: Typical RBS spectrum measured on the sample before (red) and after (black) D ion exposure.

approximation of the beam profile is also shown in Figure 4.4. The minimal nominal layer thickness after the D ion exposure coincides with the maximum of the beam.

Due to the construction of the sample holder for RBS measurements samples had to be remounted for post D ion exposure measurements. Even though we tried to realign the positions, the precise 1 to 1 correspondence before and after measurements could not be achieved. As the initial thickness taken for the sputter yield calculations we took the value measured at the midpoint of the sample with the variation from neighbouring points. Only when the measurements at the edge points were far from the average, these were neglected. In some cases we observed some decrease in the Mo layer thickness outside the centre of the beam. This can be contributed to D ion beam halo, which can be observed also on eroded a-C:H film, Figure 3.25 in section 3.3.3.

The difference between the Mo area density n_{Mo}(before) of the initial layer and the area density n_{Mo}(after) of the irradiated surface gives us the amount of eroded Mo atoms. Sputter yield can now be calculated as:

$$Y_{Mo} = \frac{n_{\mathrm{Mo}}(\mathrm{before}) - n_{\mathrm{Mo}}(\mathrm{after})}{F_{\mathrm{max}}}, \tag{4.1}$$

n_{Mo}(before) was taken as stated above, while n_{Mo}(after) was taken at the minimum Mo thickness measured at the bottom of the erosion crater (see Figure 4.4). In the centre of the sputtering crater we have also estimated the maximum D ion fluence, marked as F_{max}. The value was calculated by multiplying the time-averaged D ion fluence as measured during individual sample exposure, by the ratio of 2.7. The values were obtained from D ion beam calibration measurements described in section 3.3.3.

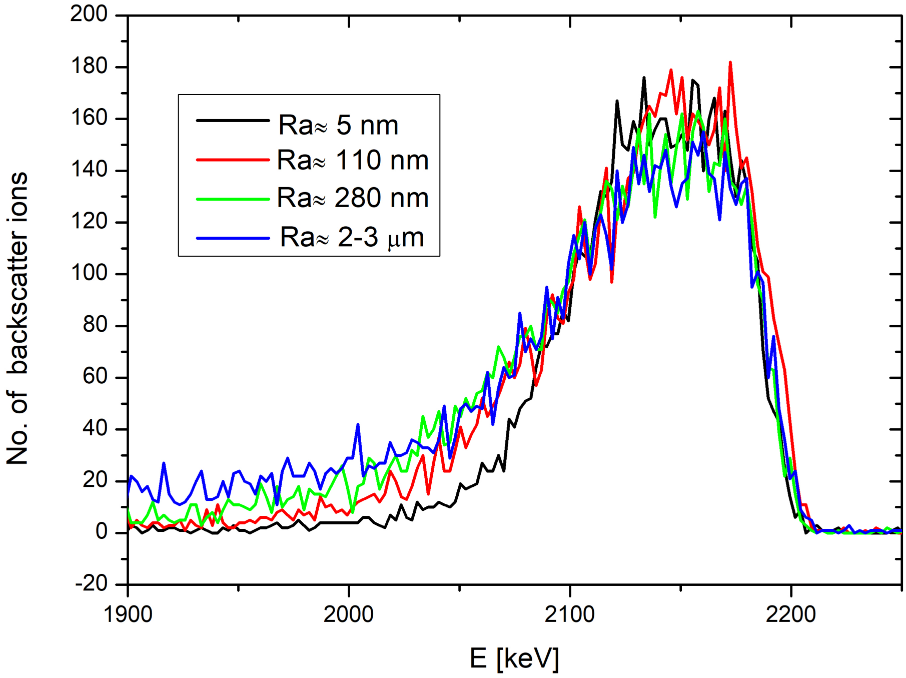

Figure 4.2: RBS signal of Mo for different surface roughness's measured on the virgin samples.

D irradiation and RBS analysis had to be conducted with two different sample holders inside the INSIBA chamber. The samples had to be transferred from one holder to the other, which could result in the worst case to a mismatch of measuring position for ≈ 1 mm, i.e., the maximum of the erosion crater is missed by 1 mm, while the maximum of the D ion flux is still used for calculating the sputter yield. This corresponds to an overestimation of F_{max} by 15 %, which leads to underestimation of the sputtering yield by 15 % at 0° impact angle and up to 30 % at high impact angles. This estimated mismatch gives the dominant contribution to the error bars for absolute values of the sputtering yields. Smaller contribution to the errors is due to the RBS measurements statistics and the discrepancy between the measurements and the simulation in the SIMNRA software, adding additional 5 % error to the calculated sputter yield. The dose measurement is not included in the error since it is a systematic error and is estimated to 5–10 %.

From the calculated eroded Mo layer thickness and applied F_{max} we can finally obtain the sputter yield as a function of impact angle for all groups of surface roughness. The experimental results are presented in Figure 4.5, which shows the sputter yield as a function of impact angle for the specific surface roughness. For all the surfaces we observe a strong angular dependence of the sputter yield. For $R_{\mathrm{a}} \approx 5$ nm we observe the increase of sputter yield for about factor of 2.5 from 0° to 60°, while for 70° we observe a four times increase from to 0°. Groups with intermediate surface roughness $R_{\mathrm{a}} \approx 110$ nm and $R_{\mathrm{a}} \approx 280$ nm, show an increase of the sputter yield with the angle by a factor of approximately five, reaching similar values as $R_{\mathrm{a}} \approx 5$ nm. For the smooth surface with $R_{\mathrm{a}} \approx 5$ nm and $R_{\mathrm{a}} \approx$ 110 nm, there is no maximum observed in the analysed angle range and the yield increases up to the highest measured impact angle of 70°. For the surface roughness of $R_{\mathrm{a}} \approx 280$

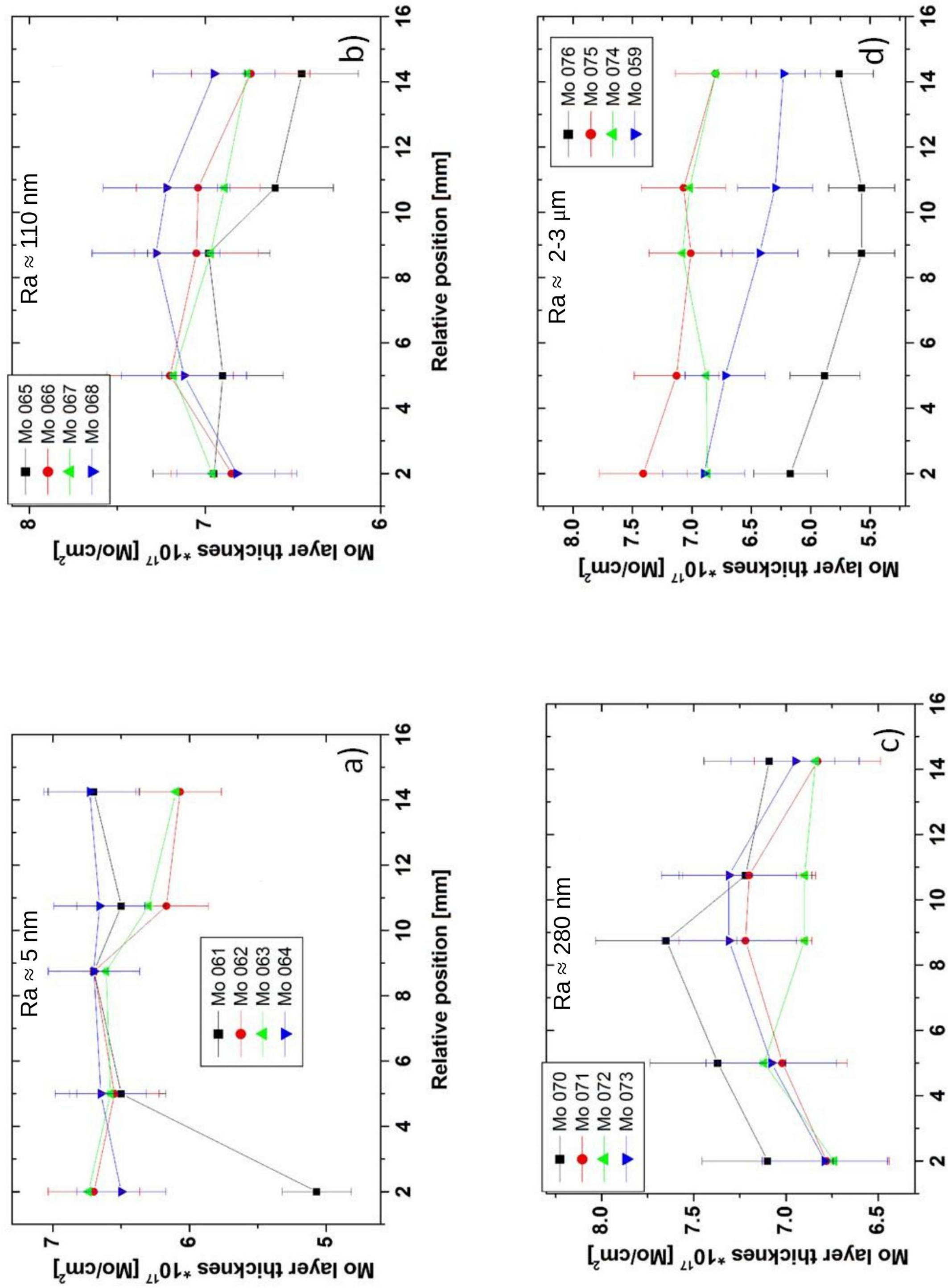

Figure 4.3: RBS measurements of the Mo layer thickness for virgin samples before D ion irradiation: Samples with surface roughness of a) thickness of Mo for $R_\mathrm{a} \approx 5$ nm, b) thickness of Mo for $R_\mathrm{a} \approx 110$ nm, c) thickness of Mo for $R_\mathrm{a} \approx 280$ nm and d) thickness of Mo for $R_\mathrm{a} \approx 2$–3 µm.

nm, the maximum of the sputter yield is observed at 60°. For $R_\mathrm{a} \approx 2$–3 µm there is no increase of sputter yield for large angles but it attains its maximum at 0°.

The sputter yield at 0° shows an increase with surface roughness from 0.5×10^{-2} Mo/D

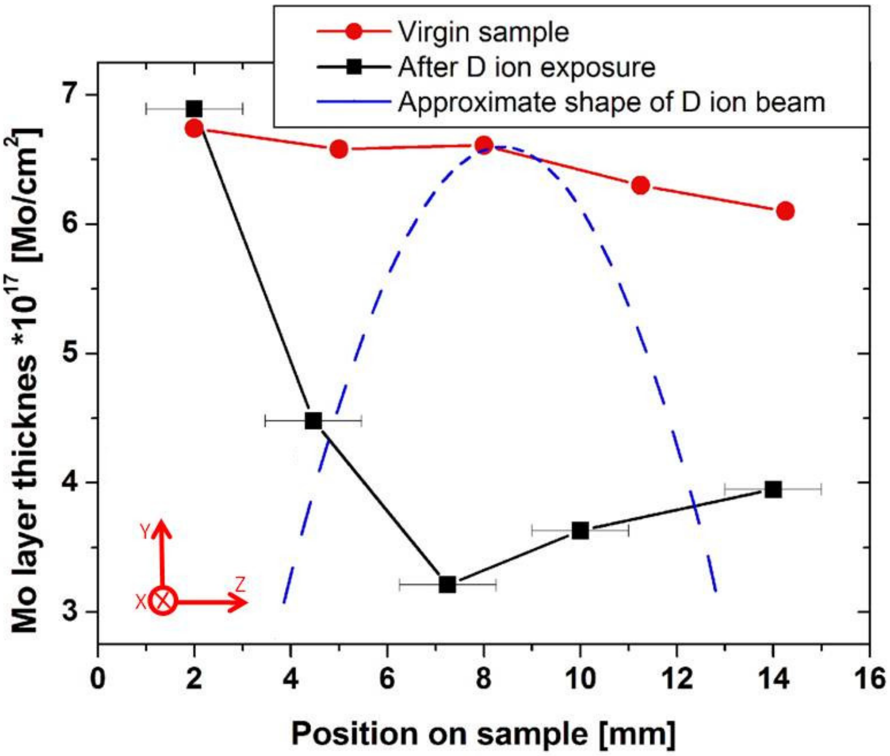

Figure 4.4: Thickness of the Mo layer as measured by RBS, before and after the exposure to 1 keV D ions at 40° impact angle on the smooth sample with Ra∼ 5 nm. The dashed line represents the envelope of the D ion beam, approximated by a Gaussian fit of the Faraday cup beam profile measurements. The error bars on individual positions represent the error of position before and after exposure RBS measurement.

for the low values of Ra to 1.3×10^{-2} Mo/D for the roughest surface. The sputter yield at large angles, e.g. at 60°, increases with the surface roughness except for the case of highest roughness studied, where it attains the lowest value. The final values of the sputter yields obtained for all surface roughness and all angles, studied in the experiment, are collected in Table 4.2.

4.1.3 Discussion on Laboratory Results

Obtained data show a clear effect of both surface roughness and angle of incidence on the value of the sputter yield. It is expected that in general the sputter yield increases with increasing angle of incidence [34]. This is observed for samples with low and intermediate values of Ra. From data shown in Figure 4.5 we observe that surface roughness affects the sputter yield differently at small and large impact angles. At large incidence angles for the polished samples and samples of intermediate roughness, we can see an increase of the sputter yield with increasing impact angle, dominantly for angles above 40°. As for angles between 0° and 40° we have no data, it would only be a speculation how sputter yields behave in this range. The increase of the sputter yield with higher impact angles can be easily explained by the fact that more momentum is transferred to target atoms in the forward direction in primary collision with D ion, before the D ion is recoiled in the collision cascade, which increases probability of atoms escaping from the surface at larger

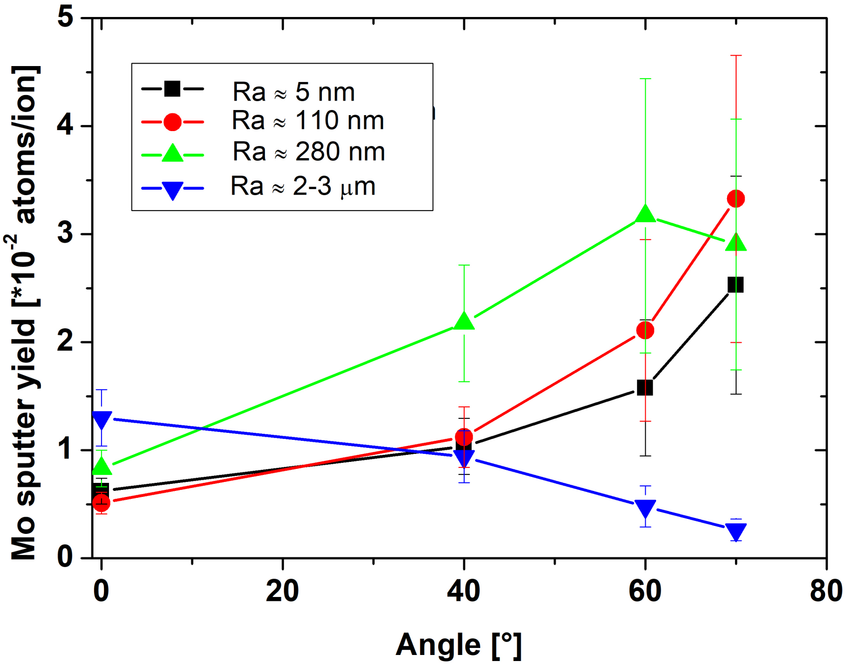

Figure 4.5: Angular dependence of Mo sputter yield obtained in laboratory set-up.

impact angles. With such a model the maximum sputter yield at angles approaching 90° is achieved, which is also supported by the theoretical prediction of Eckstein formula, or Eq. (2.16), valid for mirror polished surfaces. The calculated prediction for Mo is shown in Figure 4.6, where parameters in Eq. (2.16) were f=1.66, b=0.328, c=1.015, $Y(E_0, 0)$=0.015. The parameters were extrapolated from Table 20 in R. Behrisch and W. Eckstein [19], as there are no parameters for a D ion energy of 1 keV on Mo. In the same figure also the results of SDTrimSP 1D and 3D are shown, calculated with E_s = 8.45 eV. As can be observed the shape of the angle dependence of the calculated sputter yield agrees well with the experiential data but not in the absolute values.

As the surface roughness increases, more surface elements are exposed at effectively larger angles (90°). This can be observed for data obtained at 0° incidence angle, presented in Figure 4.7, where the sputter yield dependence on surface roughness for 0° incidence angle obtained from measurements is shown. A distinct increase of sputter yield with increased value of the surface roughness is observed. Additionally, the steepness of the sputter yield with impact angles is decreased on rough surfaces. This decrease is observed only for intermediate values of Ra, up to 280 nm. With a large value of surface roughness, two additional processes start to affect the sputtering process. The first process is a local redeposition of sputtered atoms on the nearby surfaces. This increases the probability of a sputtered atom remaining on the surface, which decreases the measured sputter yield. From the design of the experiment, we can only detect the atoms sputtered away from the target and none of the sputtered atoms that are promptly redeposited at the surface. The second process is that the increase of surface roughness also leads to shadowing effects, which are more pronounced at higher impact angles. Less sample surface is exposed to the irradiating D ion beam, which leads to a corresponding decrease of the sputter yield. An illustration of these two processes is schematically shown in Figure 4.8. The results

Sample	Ra [nm]	Angle [°]	Mo sputter yield [10^{-2}]
Mo061	≈ 5	0	0.6 ± 0.2
Mo062	≈ 5	40	1.0 ± 0.3
Mo063	≈ 5	60	1.6 ± 0.6
Mo064	≈ 5	70	2.5 ± 1.0
Mo065	≈ 110	0	0.5 ± 0.1
Mo066	≈ 110	40	1.1 ± 0.3
Mo067	≈ 110	60	2.1 ± 0.8
Mo068	≈ 110	70	3.3 ± 1.3
Mo070	≈ 280	0	0.8 ± 0.2
Mo071	≈ 280	40	2.2 ± 0.5
Mo072	≈ 280	60	3.2 ± 1.3
Mo073	≈ 280	70	2.9 ± 1.2
Mo076	22–3 µm	0	1.3 ± 0.3
Mo075	2–3 µm	40	0.95 ± 0.2
Mo074	2–3 µm	60	0.5 ± 0.2
Mo059	2–3 µm	70	0.3 ± 0.1

Table 4.2: Calculated sputter yields for molybdenum sputtered by 1 keV D ions for all the samples used in laboratory experiments.

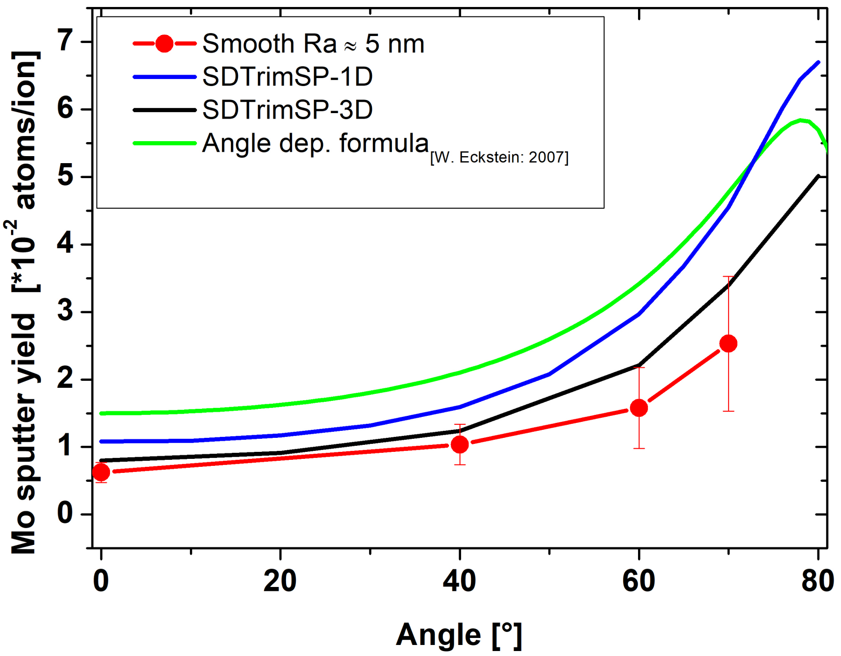

Figure 4.6: Angular dependence of the Mo sputter yield for 1 keV D particles for samples with $R_a \approx 5$ nm. Additional to the experimental values, the yields obtained with SDTrimSP 6.0 code and with SDTrimSP-3D as well as the ones from a calculation using the Eckstein angular formula for ideal smooth surfaces are given.

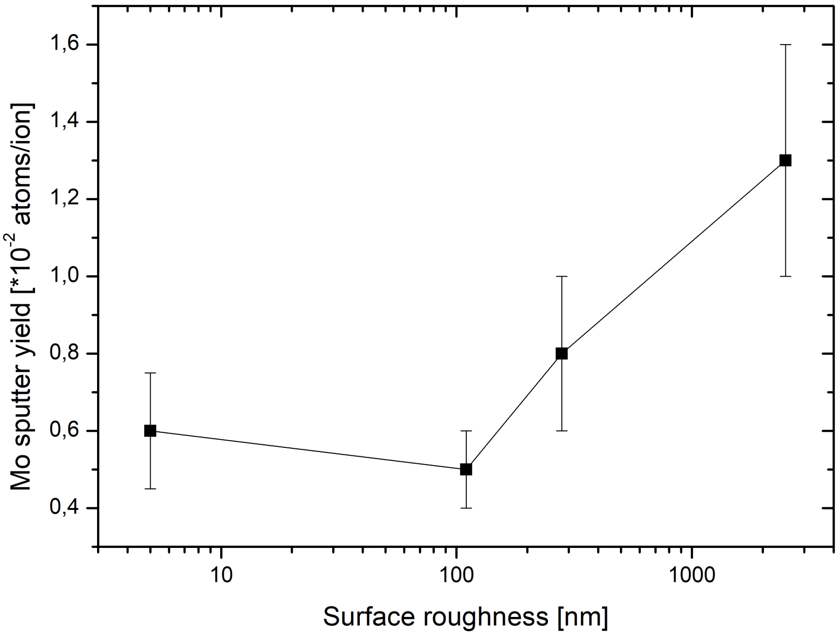

Figure 4.7: Sputter yield dependence on the surface roughness of Mo at 0° impact angle. The line plotted is to guide the eye.

lead to the assumption that these two effects are most pronounced for the samples with the highest surface roughness (2–3 µm). To make a clear conclusion, more intermediate roughness values should be investigated. The main conclusion, however, is that the sputter yield is significantly decreased for higher impact angles for rough samples.

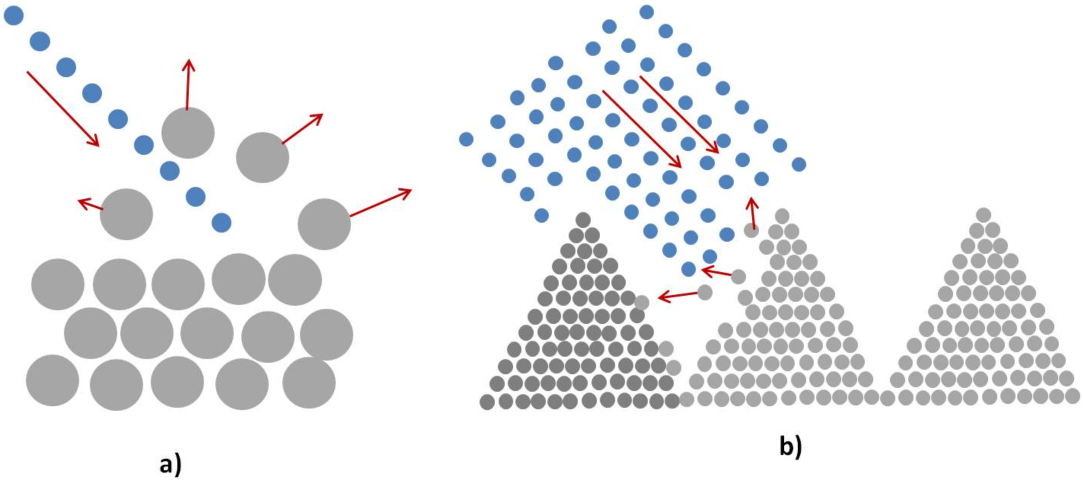

Figure 4.8: Schematic representations of the processes competing and providing the angular and roughness dependence of the sputter yield. a) Transfer of momentum in lateral direction at higher impact angles for smooth surfaces. b) Rough surfaces increase redeposition of sputter atoms and shadowing of surfaces.

4.2 ASDEX Upgrade Experiment

In the following section we will describe RBS analysis of samples exposed in the ASDEX Upgrade, as presented in section 3.4 of the study. The specific RBS measurement set-up and the interpretation of RBS measurements will be given and discussed. Contrary to the laboratory study, in the AUG it is hard to determine the exact particle flux at a specific point of the sample tile. Thus the quantification in terms of sputter yield was not possible. A relative comparison between surface roughness, however, was still possible.

4.2.1 RBS Measurements Set-up

Samples used in AUG experiment were analysed in RKS experimental station at Max-Planck-Institut für Plasmaphysik (IPP) in Garching accelerator laboratory [89], and some additional pre-characterisation analyses were also performed there. RKS experimental chamber is coupled with a 3 MV tandem accelerator. For RBS measurements PIPS detector was used, with square aperture of 5×1 mm^2 covering the solid angle of 1.10 msrad positioned at $\Theta = 165°$ scattering angle and tilted from parallel plane for $-15°$ in Cornell geometry. The ^4He ion dose was controlled with ion current measurement on the sample. To suppress secondary electrons, the sample was screened with double Faraday-screen and grounded with the inner shield biased to –240 V. The sample holder is biased to + 240 V and the current is measured with a charge integrator on the sample. The top view of RKS chamber is shown in Figure 4.9.

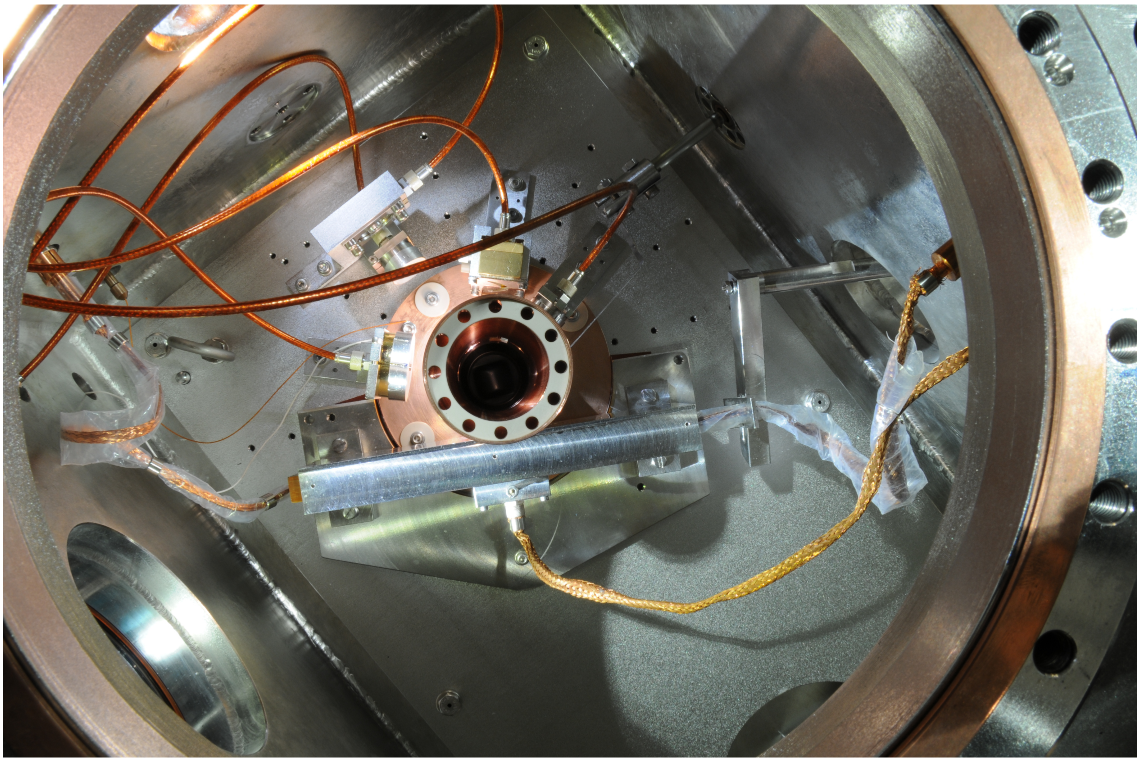

Figure 4.9: Top view of RKS chamber used for RBS analysis of samples exposed in ASDEX Upgrade tokamak.

Samples were mounted on a specially designed sample holder which could accommodate the specific geometry of samples used for the AUG experiments. There, two sample tiles can be mounted simultaneously. In the pre-exposure characterisation phase five points per sample tile were measured. With this approach the average thickness of Mo coating was determined, similarly as in the procedure in laboratory part of the study. The special feature of this holder is that it can host two tiles in the same configuration as they have been mounted in AUG-DIM-II tile [23]. For the analysis a probing ^{4}He ion beam with dimensions of 1×1 mm^2 and $E = 2.0$ MeV was used. A check of uniformity of the Mo coating on the tiles was performed before exposure. For post-mortem analysis a new strategy of measurements and data analysis was implemented, to be discussed in detail.

The first step after the finished exposure in AUG was to analyse the entire DIM-II tiles assembly in the SEM. Only after that the tiles were dismantled and individual sample tiles were removed. The tiles were then mounted on the sample holder of RKS chamber where RBS measurements were performed.

4.2.2 RBS Measurement Results and Discussion

For virgin samples the RBS measurements were performed on tiles in the 5 mm steps, as the purpose was to check the uniformity of Mo coating. The RBS peak integral for some virgin samples is plotted in Figure 4.10. Due to the larger size of the tiles, we did not obtain such a uniform thickness of Mo layer as the one used in the laboratory part of the experiment. The observed thickness deviates up to 15 % at the edge of samples, from the values in the middle. The deviation is more pronounced at higher surface roughness.

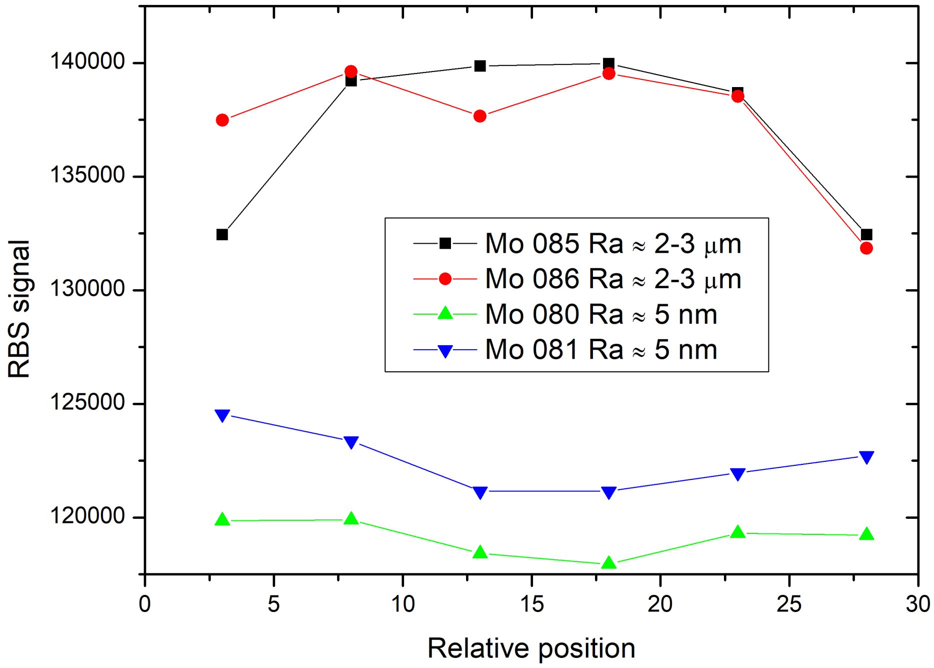

Figure 4.10: Integral of Mo peak in RBS spectra for AUG samples with $R_\mathrm{a} \approx 5$ nm and $R_\mathrm{a} \approx 2$–3 µm.

Due to the thickness variation and the fact that ion flux in the vicinity of OSP is not uniform, the RBS measurements on the exposed samples had to be performed with higher spatial resolution. The post-mortem scans were made in 1mm steps and 1×1 mm^2 ion beam size, in the vicinity of OSP. In the regions that were further away from OSP larger steps were made. With such an approach a more detailed insight to erosion profile was achieved.

The detailed scan of RBS measuring points in the poloidal direction in vicinity of OSP gives an information on the amount of Mo atoms removed from the surface. Simultaneously with erosion some deposition of W from other parts of AUG plasma chamber occurred. This is clearly visible in Figure 4.11, where two RBS spectra are shown, one before and another one after the exposure in AUG. In higher channels one can clearly observe an additional peak, that corresponds to W. The deposition on the surface makes fitting of RBS spectra significantly more complex.

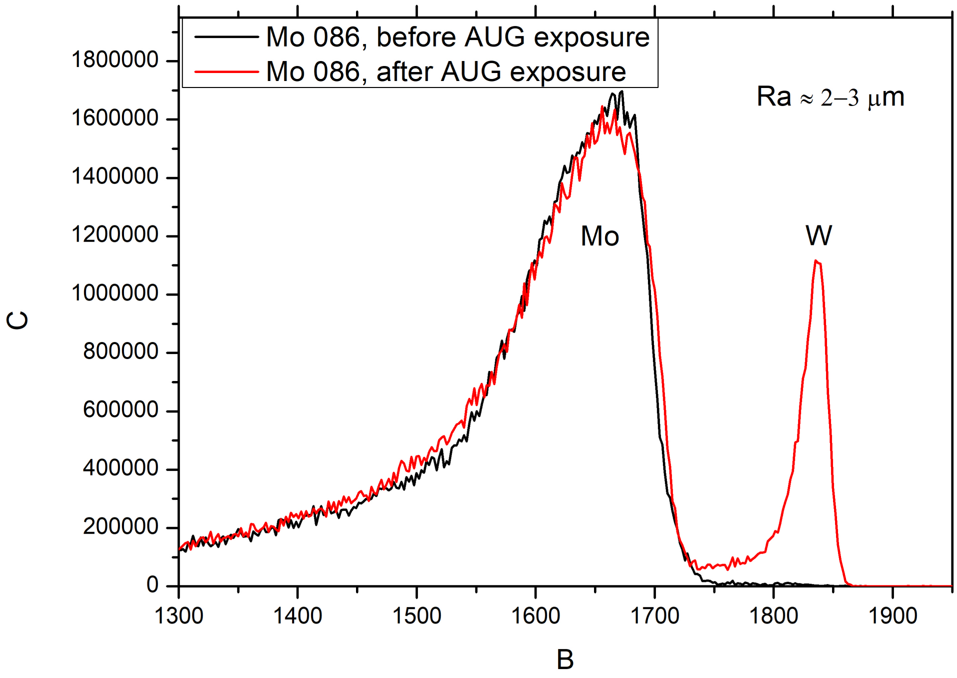

Figure 4.11: RBS spectra measured on a tile before and after exposure in ASDEX Upgrade. A peak of W deposition is clearly visible.

The interpretation of the measured data is further complicated by some mixing of Mo and W. Thus, the fitting of spectra, with models provided in SIMNRA was not possible. Due to the non-zero signal between Mo and W peaks we could not find a unique solution to fit the spectra. The W peak is sufficiently isolated that the quantification of W deposition can be made. As for Mo thickness, the integrals over the same energy region of spectra were compared. Additionally, the fluence at a specific point could only be estimated with low precision. Thus, the quantification of erosion in terms of sputter yield was not possible. However, a qualitative comparison could still be made. The measure used was the amount of eroded Mo. This was estimated by comparing the integral fit of Mo peak in the RBS spectra, before and after the exposure in AUG. For the points that were not measured on the virgin samples, a linear extrapolation from neighbouring points was taken as the virgin layer thickness.

The main erosion activity, with the highest ion flux, was concentrated around OSP which was also located in the vicinity of sample borders in the set-up used. To this end the representation of erosion is simple. In Figure 4.12 the border for samples of $R_a \approx 5$ nm and $R_a \approx 2$–3 µm is shown, with Mo erosion profile and W deposition in the vicinity of OSP. In the figure we can observe peak of the erosion in the vicinity of OSP.

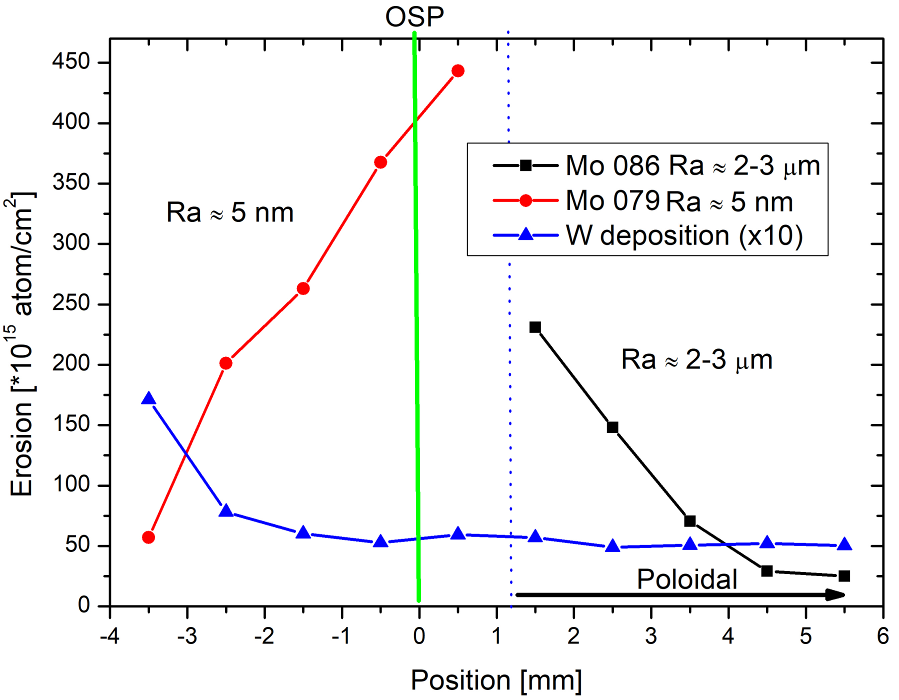

Figure 4.12: Quantitative RBS data for erosion of Mo and deposition of W for samples with $R_a \approx 5$ nm and $R_a \approx 2$–3 µm.

The first conclusion that can be made from Figure 4.12 is that the erosion profile is similar to the ion flux distribution, shown in Figure 3.31. This is expected, as the sputter yield is independent of fluence in the conditions of tokamak plasma. This means that the maximum of erosion is located near the location of OSP, where the maximal particle flux in AUG is achieved. The calculated position of OSP is marked with a green line in Figure 4.12. The dashed line marks the border between the two samples in the vicinity of OSP. The amount of eroded Mo drops significantly with increasing distance from OSP. There is a marked difference between the eroded amount of Mo in samples with $R_a \approx 5$ nm and $R_a \approx 2$–3 µm. From the measured data we find that sample with $R_a \approx 5$ nm experienced roughly two times higher erosion than the sample with $R_a \approx 2$–3 µm. Erosion of Mo is strongly affected by surface roughness, but can not be said for W deposition. At least in the vicinity of OSP the deposition of W seems uniform.

A similar behaviour was observed for other combination of the samples, which had surface roughness values of $R_a \approx 110$ nm and $R_a \approx 280$ nm. The data of this pair of samples are shown in Figure 4.13. There is no significant effect of surface roughness on deposition profile of W. It looks like decrease of W deposition on the lover part of OSP, but this can be explained with vertical offset in the alignment of sample tiles inside the DIM-II sample tile. This leads to creation of shaded areas on the borders of the samples.

If the measured erosion profile is compared with the calculated position of OSP, marked green in Figure 4.13, the observed maximum of erosion seems to be shifted by about 3 mm.

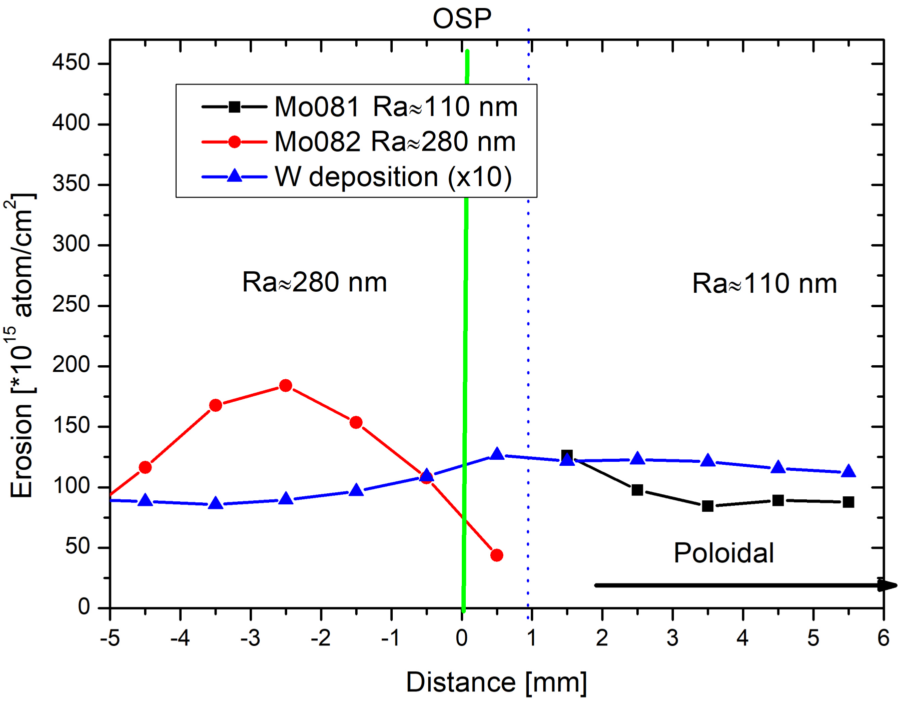

Figure 4.13: Quantitative RBS data for erosion of Mo and deposition of W for samples with $R_\mathrm{a} \approx 110$ nm and $R_\mathrm{a} \approx 280$ nm.

Despite that OSP in AUG can be precisely manipulated, such tolerances are still expected. After taking this into account the erosion profile again follows the flux distribution in AUG. The samples surface roughness in this case is quite similar, and the erosion seems similar for both samples. The observed minimum in the erosion of sample Mo82 ($R_\mathrm{a} \approx$ 280 nm) at the position of the calculated OSP is modified by vertical misalignment of both samples. This creates the geometrically shaded area at which the plasma flux is reduced, and consequently the net erosion is reduced.

4.3 Comparison of Laboratory and ASDEX Upgrade Results

A direct quantitative comparison of results obtained in the laboratory experiment and in AUG is difficult. The first reason is that inside AUG OSP we experience significant variation of the ion flux in the poloidal direction, due to its exponential distribution, as seen in Figure 3.31. In addition, the transfer of samples from DIM-II tile to RBS measurements introduce an alignment error which prevents a precise determination of the ion fluence at a specific point of the sample.

An additional complication in providing quantitative data for samples exposed in AUG is the creation of a mixed layer of Mo and W on the surface, observed as non-zero signal between Mo and W peak in RBS spectra, in Figure 4.11. Despite these limitations some qualitative comparison of the data can be made.

In the laboratory data for surfaces with $R_{\mathrm{a}} \approx 5$ nm and $R_{\mathrm{a}} \approx 2$–3 µm at 60° a significant difference in absolute sputter yield for both surfaces is observed. This angle is expected average angel of impact in AUG [40]. In the laboratory set-up the sputter yield for Ra∼5 nm was found about three time higher than for the $R_{\mathrm{a}} \approx 2$–3 µm. In the samples exposed in AUG there is also a significantly higher erosion on the smoother sample than on the rough one for the points away from OSP, on the flatter part of the exponential distribution of ion flux. The observed difference in erosion is still significant, amounting to a factor of two. However in samples with intermediate roughness, $R_{\mathrm{a}} \approx 110$ nm and $R_{\mathrm{a}} \approx 280$ nm, a large difference in erosion is not observed, as also expected from the laboratory experiment. Both values of sputter yield agree within error bars. The reduced difference in the case of$R_{\mathrm{a}} \approx 5$ nm and $R_{\mathrm{a}} \approx 2$–3 µm as compared to laboratory experiment could be influenced by two effects. Firstly, the angle of impact in AUG is roughly 60°, but this is only an estimate and should be simulated for each plasma scenario independently, while in the laboratory this angle was fixed. In addition, the angular spread in the AUG is not precisely known. It is expected to be much larger than in the laboratory case, where it was around 1°. If the impact angle is $< 60°$, in laboratory results the difference in sputter yield is decreased. Its values are almost equal at 40°. The second strong effect influencing the measured erosion in AUG samples is the creation of mixed layer of Mo and W. This layer was not taken into account in fitting the thickness of Mo layers in RBS spectra in the post-mortem analysis of AUG samples. The layer was ignored as we do not know how strongly the W layer is deposited on the surface and how closely it can mimic the surface morphology of the sample beneath. The layer is described with two free parameters in the fitting procedure of RBS spectra, the surface roughness of layer and its thickness. The behaviour of this mixed layer with regard to surface morphology is yet unknown and could form a subject of future analysis of these samples with different techniques.

Despite the quantification problems the combined results from the laboratory experiment and the exposure in ASDEX Upgrade tokamak point to the same trend. It is that the surfaces with roughness in the µm range suffer less erosion than the polished ones. However, the erosion of plasma-facing components is not the only limiting factor in their lifetime estimation. Another is the impurity retention which will be briefly discussed in the next chapter where the effect of surface roughness on impurities retention will be presented.

4.4 SDTrimSP Simulation Results

In this section we describe the results of SDTrimSP 6.0 simulations. The parameters important for calculating the sputter yield are discussed in detail. At the end a comparison of the calculated sputter yields to the ones obtained in laboratory experiment is given.

4.4.1 Parameters and Results of 1D Simulation

Calculation of sputter yields is one of applications of SDTrimSP code. In simple case of 1 keV D ions on Mo, the static regime of calculation was sufficient. With this step, the target calculation and update step were avoided [79], to spare some computer power. As an integration method the Gauss-Legendre procedure with eight pivots was chosen [79] on the basis of past experience, and the same for the Krypton-Carbon (KrC) interaction potential selection to describe the nuclear stopping power [90]. The simulations were performed with 10^6 D particles, run in the mode of angle of incidence variance. This is a build-in-routine in SDTrimSP, the seed parameter was to perform 19 different angle calculation between 0° and 90° in nonequidistant slices [79]. More details can be found in the copy of tri.inp file in Appendix A, where specific input parameters are commented. The simulations were run on laptop HP EliteBook 820, with an Intel CORE i5 4300u processor [91]. Calculation was performed in nonparallel mode of calculation and took less than 6 h. The SDTrimSP, at least in its 1D form, is a powerful tool in calculating the ion-matter interactions even on nonspecialised computer clusters. The tri.inp file in Appendix A looks complicated. However, most of additional input parameters were inserted to avoid unnecessary calculations in the bulk of the target, and thus reduce the computing time.

First runs were performed with tabulated data from SDTrimSP library. The assumption was that the tabulated parameters will describe the sputtering of Mo sufficiently well as in previous cases for W [84]. The output of this simulation is plotted in Figure 4.14, showing that the calculated values are three to four times higher than the measured ones. There are reports for SDTrimSP to overestimate the sputter yields for brittle material (such as Mo and W) [84]. However, the usual overestimation is less than a factor of two at low impact angles, while providing good agreement at high impact angles [84].

This led us to investigate the effect of one parameter on the calculation results. From past experience the main focus was on the binding energy E_s of atoms in target [38]. The heat of sublimation (ΔH_s) is usually taken as the first approximation for E_s, for Mo given in SDTrimSP as 6.810 eV. From past comparisons the argument arose that in some cases E_s is larger than the heat of sublimation. For Mo E_s is also dependent on surface crystal orientation, as seen in Table 4.3.

	E_s [eV]
ΔH_s	6.810
Mo (111)	7.380
Mo (110)	9.180
Mo (100)	8.780

Table 4.3: Values of surface binding energy E_s for different surface crystal orientations of Mo [38].

It was shown that for amorphous Mo targets under H, D, He and Ne irradiation, a good approximation is an average value of E_s over all crystal orientations [92], [93]. The surface energy dependence of the measured and calculated sputter yield of molybdenum

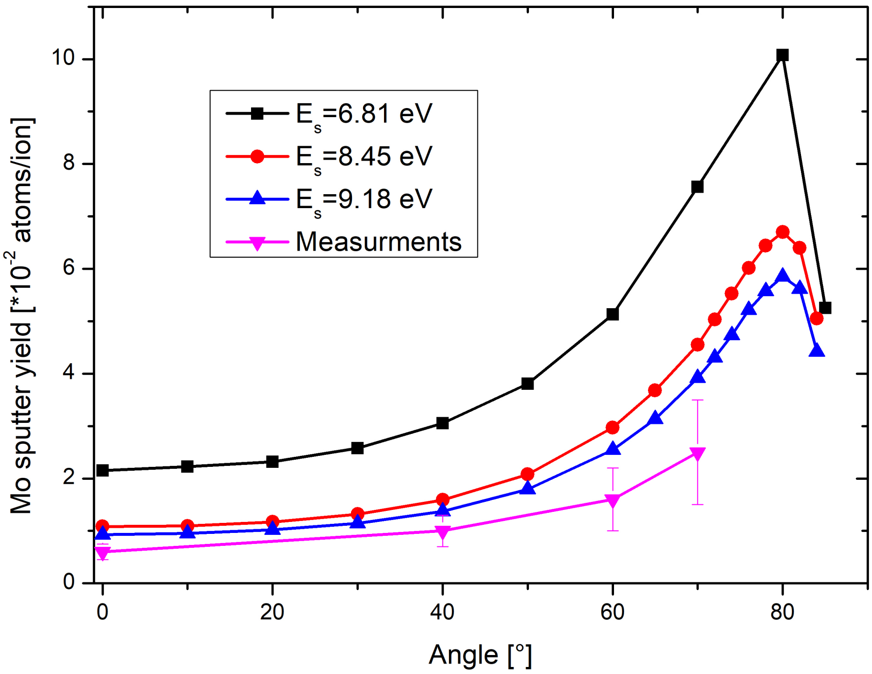

Figure 4.14: Simulation of Mo sputter yield for 1 keV D for different values of E_s and comparison to the measured values.

under neon irradiation is shown in Figure 4.15 for incident angle $\alpha = 0°$, where we see that applying the average value of E_s agrees better with measured data.

The value of E_s was calculated as the arithmetic average of all three values for three crystallographic orientation as

$$E_s = \frac{(7.380 + 9.180 + 8.780)\ \text{eV}}{3} = 8.45\ \text{eV}. \tag{4.2}$$

This value was used in the future calculations. Adjusting the value of E_s provides a better agreement with the measured data,but the calculated values still differ from measurements by roughly a factor of two. This was expected for low angles, yet the same discrepancies were still present at high angles. Results of 1D simulations are presented in Figure 4.14 where discrepancies in calculated sputter yield can be clearly visible. Changes in the value of E_s explain some deviation between calculation and the measurement,but the discrepancy remains. As our measurements of sputter yield were performed on mm scale, while SDTrimSP 1D simulations are taken at a single point, this leads to conclusion that the surface of samples affect the sputter yield in some way. From the SEM images of sample surface, holes on the surface of polished graphite tiles are seen, as shown in Figure 3.13. This was an indication that even for polished samples a simulation with the 3D code is needed.

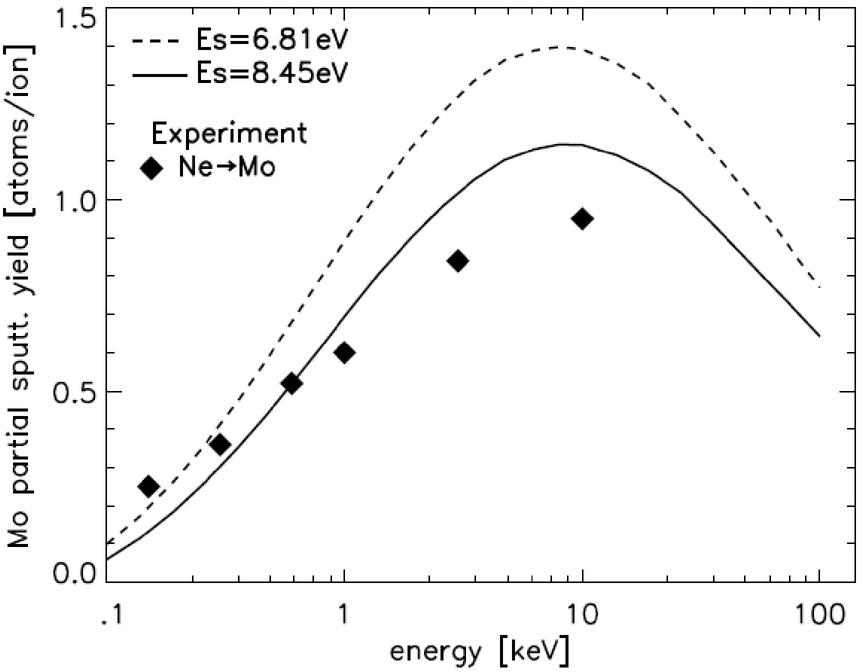

Figure 4.15: Comparison ofmeasured and calculated sputter yield as a function of impact energy of Ne on Mo. Calculated data for different values of E_s are shown for incident angle of $\alpha = 0°$. Image taken from J. Roth et al. [93].

4.4.2 Extension to 3D Simulation and Comparison to Laboratory Experiment

SDTrimSP 3D is a complex code, so we have closely collaborated with Andreas Mutzke (Planck-Institut für Plasmaphysik, Greifswald, Germany). With our suggestions and discussions he prepared input data for SDTrimSP 3D simulations and ran them on computer clusters at IPP Greifswald.

Due to the complexity of the calculation only five discrete impact angles for each surface roughness, namely $0°, 40°, 60°, 70°$ and $80°$, were simulated. The main additional input for 3D code is the representation of sample surface. This was an easy task for samples of intermediate and high roughness where we used AFM or Confocal Laser Scaning microscope (CLSM) [94] topography measurements. For surfaces with intermediate roughness (110 nm and 280 nm) AFM measurements on 10×10 µm^2 grid with lateral resolution of 39 nm were used. For the roughest samples we opted for CLSM microscope on 650×650 µm^2 grid with lateral resolution of 625 nm. Both of these techniques are sensitive to small changes of the surface height, but they are not suitable for describing the smooth sample with a large depression on the surface as on our samples with $R_a \approx 5$ nm. Therefore the construction of an artificial input surface was required. It was constructed as a cubic depression in centre of 10×10 µm^2 flat surface. Different sizes of the depression were investigated, estimated from SEM images. The cubic holes were chosen to simulate sharp edges that are observed in SEM images on the sample surfaces. The simulation was run with two sizes of cube, 2.5 µm and 5 µm. Results of the simulations are plotted in Figure 4.16 .

As seen from figure 4.16 a better fit to the experimental data was achieved, after introducing the holes. Also there is no significant change in absolute value of the sputter yield going from holes with 2.5 µm size to 5 µm size. The simulation with $E_s = 9.18$

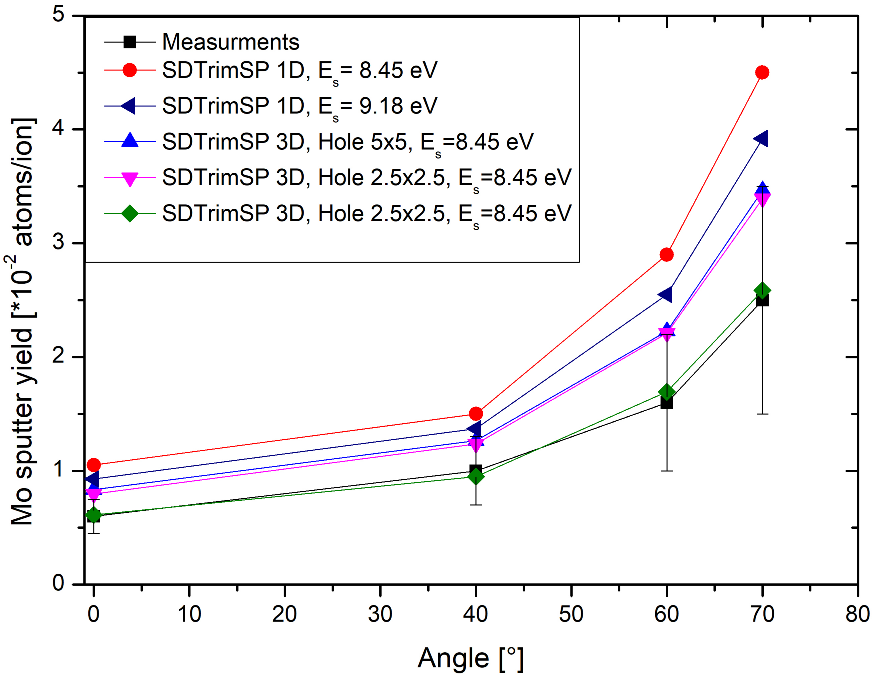

Figure 4.16: SDTrimSP simulation for smooth surfaces with different parameters. 1D simulations and model surface with cubic depression in centre, with different E_s.

eV and 2.5 µm hole was performed, as there is some indication from studies with W that during pulsed laser deposition of thin layer formation there is a tendency to form a crystallographically oriented surface in (110) direction. Even though we do not have any proof that this is the case also for Mo, the good agreement with the experiment indicates that this may be true also for Mo. However, this remains a speculation as no technique sensitive to crystal orientation was used on these samples. The analysis of parameters for samples with $R_\mathrm{a} \approx 5$ nm helped us to proceed with reasonable simulations on rougher samples using height measurements as an input. Calculated data are presented in Figure 4.17: for easier comparison they are plotted together with measured data from laboratory part of the study.

Comparison of the SDTrimSP-3D simulated data with measured data in Figure 4.17 shows that simulations give slightly higher values of sputter yields, but are still within the experimental error bars. For intermediate surface roughness, no micron-size holes as seen on polished samples were observed. Therefore, additional hole structures in calculations for other surface roughness were not included. We are suspecting that plasma etching procedure smoothes out the holes to some extent. Which is suported, by he results for $R_\mathrm{a} \approx 110$ nm, as trends agree with simulations. In the case of $R_\mathrm{a} \approx 280$ nm surface roughness, the simulation does not show any peak of sputter yield at 60° as is observed in experimental data but just an increase with angle as for the other two cases before. The simulation for the roughest surface of $R_\mathrm{a} \approx 2$–3 µm predicts an increase of the sputter yield by a factor of 1.5 at the largest angle, while the experimental data show a decrease of the sputter yield by a factor of five. The absolute values of the simulated sputter yield at 0° are in all cases higher than in the experiment except for the roughest case.

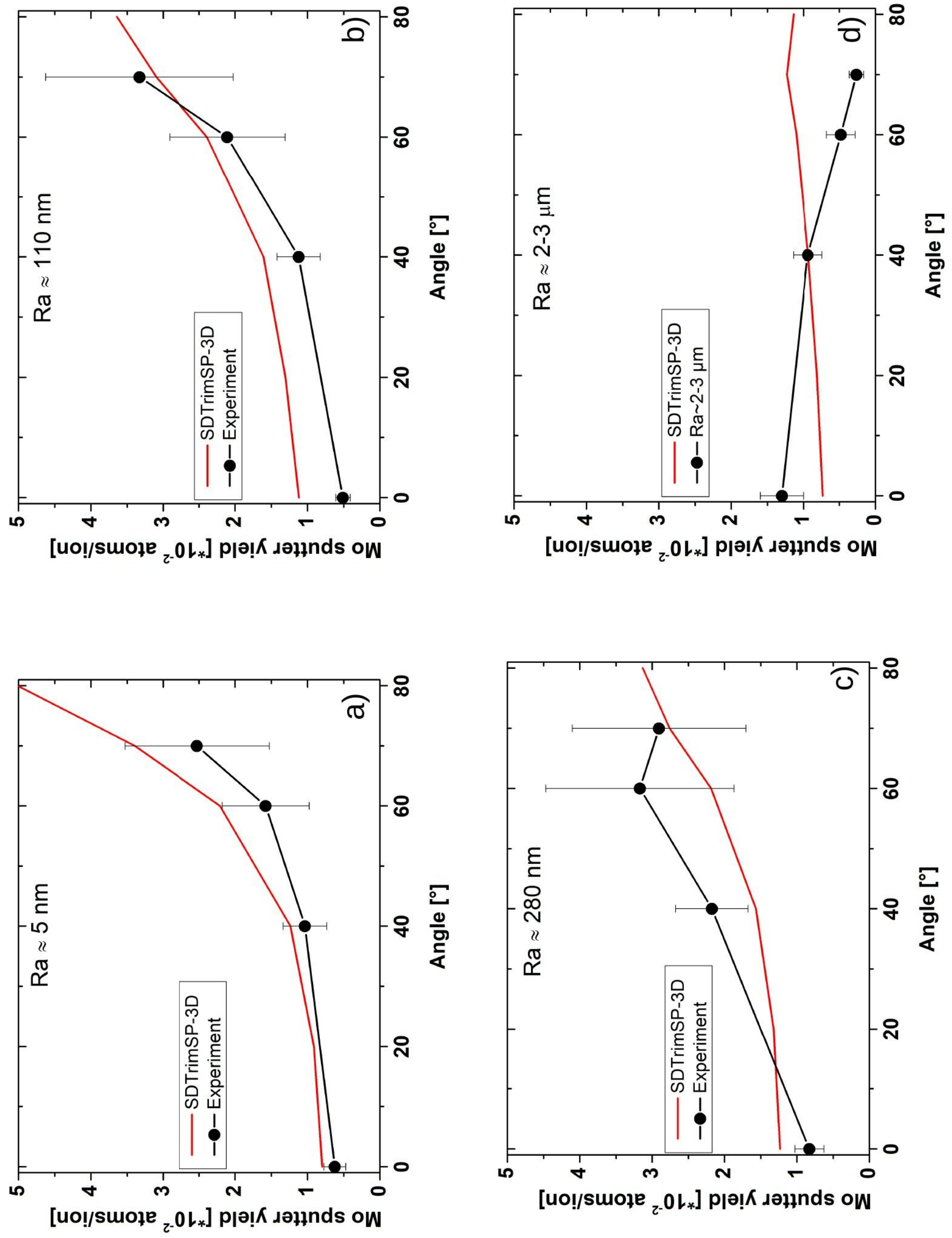

Figure 4.17: The experimental sputter yield and the SDTrimSP-3D simulation results as a function of angle for 1 keV D on Mo for the four different studied surface roughness with Ra a) $R_\mathrm{a} \approx 5$ nm, b) $R_\mathrm{a} \approx 110$ nm, c) $R_\mathrm{a} \approx 280$ nm and d) $R_\mathrm{a} \approx 2$–3 µm.

4.5 Summary and Discussion of the Results

In the previous section we have described in detail the work done with each specific work package, here we summarise the results obtained and discuss the complementarity of each package towards better understanding of the sputtering processes on plasma facing surfaces in fusion devices.

The basis of this study represents the investigation of sputtering of thin Mo layers under D ion irradiation. Polished graphite tiles were coated with 115 nm of Mo using a pulsed laser deposition. This allowed us to mimic the substrate surface while still having uniform coating. This was important, as substrates with well defined surface roughness were needed. Roughness ranged from 5 nm up to 2–3 µm. The thickness of Mo layer on each sample was measured with RBS before and after D ion exposure, which in combination with known ion dose enabled the calculation of the sputter yield for Mo at various angle of incidence and for different surface roughness. For all surfaces in the laboratory study a strong angular dependence of sputter yield was observed. Intermediate surface roughnesses, i.e. $R_\mathrm{a} \approx 110$ nm and $R_\mathrm{a} \approx 280$ nm, show an increase of the sputter yield with the angle by a factor of approximately five compared to 0°, reaching similar values as $R_\mathrm{a} \approx 5$ nm. For the surfaces with $R_\mathrm{a} \approx 5$ nm and $R_\mathrm{a} \approx 110$ nm, there is no maximum observed in the analysed angle range and the yield increases up to the highest measured impact angle of 70°. For the surface roughness of $R_\mathrm{a} \approx 280$ nm, the maximum of the sputter yield is observed at 60°. For $R_\mathrm{a} \approx 2$–3 µm there is no increase of sputter yield for large angles, it retains its maximum at 0°. The sputter yield at 0° shows an increase with surface roughness from 0.5×10^{-2} Mo/D for the low values of R_a to 1.3×10^{-2} Mo/D for the roughest surface. The sputter yield at large angles, e.g. at 60°, increases with the surface roughness except for the case of the highest roughness studied, where it retains the lowest value. The overview of this data is presented in Figure 4.5.

In parallel with the laboratory study, samples of the same composition were exposed to the plasma discharges in ASDEX Upgrade tokamak. Samples were mounted in the vicinity of OSP on the DIM-II mounting tile. With this set-up we were able to insert and retrieve samples from tokamak quickly, therefore exposing them to only few plasma discharges. This set of samples was exposed to eight L-mode discharges of deuterium plasma, each 6 s in duration. Samples were positioned in pairs below and above OSP to provide as close as possible comparison of erosion. Since in tokamak the precise ion dose deposition is hard to estimate, we are not able to get quantitative data of sputter yield on Mo under these conditions. To make additional complications, the discharges contained some amount of ^{15}N, for parallel experiment on AUG at this time, with unknown contribution to the sputtering. Also a weak deposition of W occurred during discharges making the analysis of RBS spectra non-trivial. Nevertheless, one parameter is well controlled: the impact angle of particles on the samples. In the case of AUG in L-mode discharges it is around 60°. However, some conclusions about the sputtering in the tokamak can be made. In figure 4.12 a lack of erosion on the tile with $R_\mathrm{a} \approx 2$–3 µm compared to 5 nm, can be observed in the points close to the OSP. For the other pair of the samples the results are plotted in Figure 4.13 where a similar amount of erosion for both $R_\mathrm{a} \approx 110$ nm and $R_\mathrm{a} \approx 280$ nm can be observed.

The results can be complemented with the results from the laboratory study where similar sputter yields for samples with intermediate surface roughness at 60° impact angle are measured, while for polished samples roughly three times higher sputtering than in those with $R_\mathrm{a} \approx 2$–3 µm is found; a similar difference is also observed in Figure 4.12.

In the third package we simulated the laboratory sputtering results with the SDTrimSP 6.0 software. We began the calculation with 1D model, with investigation of the right parameters for the input in the calculation. As it turned out, one of the most important parameters in calculation is surface binding energy. At the end 8.45 eV was chosen, higher than the tabulated value in the SDTrimSP. The value was obtained as the arithmetic average for three crystallographic orientations of Mo lattice. The 1D is not sufficient to describe the effects of surface roughness on the sputter yields, so we extended the calculations to 3D version of the software. SDTrimSP 3D takes one additional input in the simulation, some topographical representation of the sample surface. For this we used height measurements either from AFM or CLSM. In the end we achieved a good agreement between simulations and measurements, as seen in Figure 4.17.

However, in general the SDTrimSP-3D calculations give larger values than measured. For the samples with $R_\mathrm{a} \approx 2$–3 µm, larger discrepancies between the calculated and the measured data can be noticed. As shown for the case of SDTrimSP-3D for smooth surfaces, we needed to introduce the surface with holes. As compared to the 1D model, the introduction of holes significantly decreased the sputter yield. The surfaces for the roughest samples also show some deep depressions in the surface morphology and these were fed in SDTrimSP-3D as input. This was one of possible reasons to obtain lower values of sputter yield. Additionally, SDTrimSP-3D does not take into account spikes smaller than the lateral resolution of the input data. In our case this means no additional features smaller than 650 nm. From SEM images, seen in Figure 3.13, we observe structures with smaller Ra on top of the rough surfaces. The erosion of these spike-like structures can explain the larger values measured at 0° impact angle compared to simulations. In addition, these structures increase the active surface of the sample. This leads to a larger prompt deposition rate at higher impact angles, which is experimentally observed as a decrease of the sputter yield. From SDTrimSP data we can estimate that this prompt deposition can occur for up to 25 % of sputtered atoms. However, the exact value is strongly dependent on surface roughness and impact angle. Despite this, the SDTrimSP-3D can still be a useful tool to predict the behaviour of the sputter yield. However, we need to be aware of its limitations posed by the quality of the provided input data, provided with CLSM.

Now let us discuss the discrepancy in the sputter yield between the measured and the simulated values at low impact angle where we also measured a small increase for surface rougnesses of $R_\mathrm{a} \approx 280$ nm and $R_\mathrm{a} \approx 2$–3 µm. A similar trend of the absolute sputter yield values compared to SDTrimSP simulations for different surface roughness was observed by Arredondo et al. [84]. They also report an increase of the sputter yield at low impact angles ($< 40°$) with increasing surface roughness and a decrease at high impact angles ($> 40°$). It should be stressed that the rough surfaces prepared in that experiment had a much wider angular distribution of surface angles than the samples in our study, although they still had a Ra value of 20 nm. This angular distribution in case of Arredondo et al. [84] is assumed to be the origin of the lower sputtering yield at 60° impact angle compared to the smooth surface, despite the low Ra value. We observe an increase of the sputtering yields for intermediate roughness. One of the most important issues raised by R. Arredondo et al. [84] is the observed discrepancy of calculated sputter yields with SDTrimSP for D on W, where SDTrimSP overestimated the sputter yield approximately by a factor of two. The explanation given by Arredondo et al. [84] is that the binary collision approximation, on which SDTrimSP code is based, is not strictly satisfied for brittle materials (W, Mo), in contrast to ductile ones (Ni, Au). We observe a similar overestimation for D on Mo, where the simulated data here and in Ref. [19] exceed the measured sputter yield. The agreement between experimental data and SDTrimSP-3D simulations was improved by choosing a higher surface binding energy and appropriate surface morphology. With this the simulations achieved better agreement with the measured data.

Chapter 5

Effects of the Surface Roughness on Impurity Retention

In the previous chapter the focus was on the discussion of the effect of the surface roughness on sputtering. However, in tokamak additional plasma surface interactions are taking place which can also be affected by the surface roughness. One of the more important processes is the retention of fuel and other impurities in the first wall material. This is a broad topic in productive research in the last years. To present the main idea how the surface roughness affects the impurity retention a short overview of two articles will be given, reporting on studies done in ASDEX Upgrade tokamak and PSI linear plasma device, where samples with different surface roughness were exposed different plasma conditions. First paper is titled *Micro-NRA and micro-3HIXE with* ^{3}*He microbeam on samples exposed in ASDEX Upgrade and Pilot-PSI machines* [95] and *Study of lateral distribution of impurities on samples exposed in the ASDEX Upgrade using microbeam of* ^{3}*He and* ^{1}*H* [96].

In both studies a variety of different samples were used. In one of the study graphite substrate samples were used, similar to those in the previously described AUG experiment. Instead of Mo coating, a thin tungsten layer was used. The first evidences of roughness dependent sputter yield in fusion environment was presented.

In the second study a more complex set of samples with varying surface roughness were analysed. The main focus was on studying retention of impurities, D, B and N, depending on surface roughness of the samples.

The analysis in the studies was performed using a micro-beam experimental station. It gives an even more detailed insight onto the erosion and impurity deposition, with the results still comparable to broad-beam experiments [97].

Measurements with micro-beam were performed using the 2 MV tandem accelerator at the Jožef Stefan Institute. The micro-beam line is located at −10° from the exit of the accelerator [97]. The end station, presented in Figure 5.1 is equipped with a 5-axes manipulator and a microscope with a camera for samples positioning in the focal plane of the ion beam. In front of the end station a triplet of Oxford microbeam quadrupole magnetic lenses [98] is used for focusing the ion beam and with deflection coils for manipulation of the beam in a raster pattern on the sample.

The micro-beam end station is connected with the accelerator and coupled with a high brightness multicusp ion source, as is primarily used for micro-PIXE with protons. In this configuration proton beam can be focused to dimensions of 500×500 nm^{2} [99], [100]. For NRA measurements we used a ^{3}He ion beam. Negative ^{3}He ion beam is formed in combination of a duoplasmatron ion source and a Li-charge exchange canal, involving a setup for ^{3}He and ^{4}He gas mixing within the duoplasmatron housing to spare the precious ^{3}He gas. Positive He ions with initial energy of 20 keV are directed through a charge

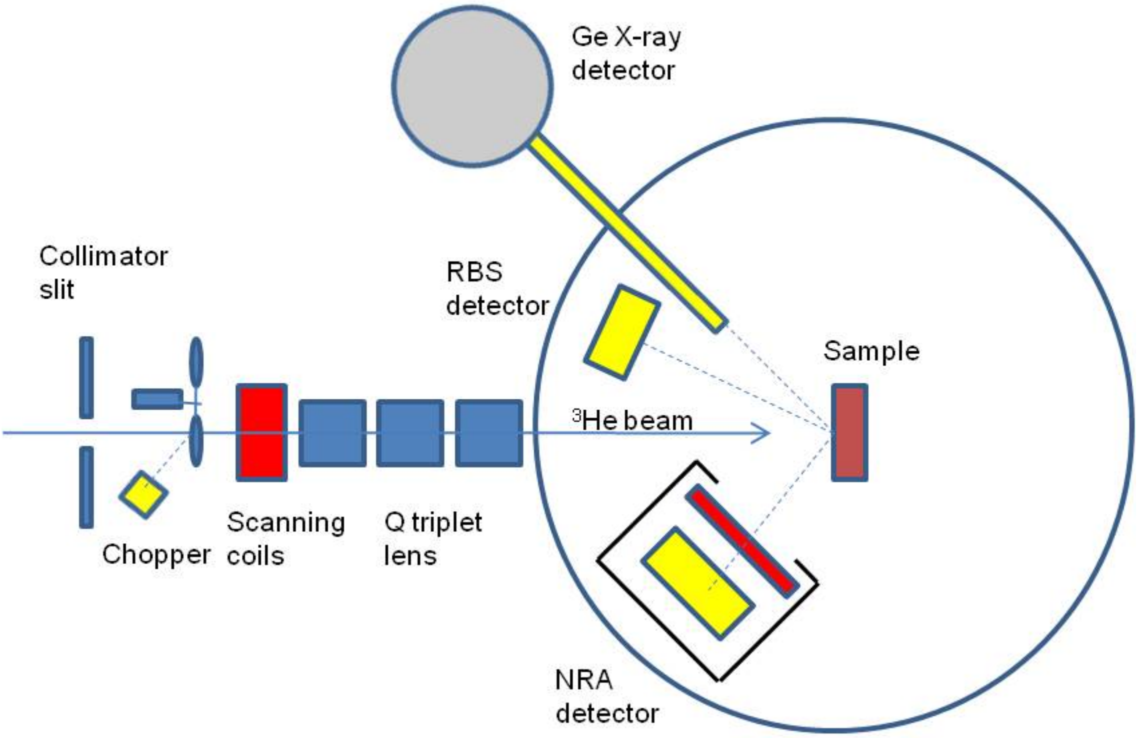

Figure 5.1: Schematic drawing of experimental set-up at micro-beam end station with added NRA detector.

exchange channel, where in collisions with Li vapour short-living He^- ions are created. The ions are accelerated with a tandem accelerator to a desired energy of a few MeV. Under such conditions, a rectangular He ion beam with a size of 10×10 µm^2 is produced on the target position. Due to low brightness of the beam both object and collimating slits at the microprobe have to be widely open in order to provide a particle current of 300 pA [95]. The dimensions of the beam are optimised with a knife edge method on a copper grid [101], using induced K_α X-ray emission and i-Ge X-ray detector.

With the existing hardware, we are able to scan across an area of 2.2×2.2 mm^2, to produce elemental maps with a resolution of 256 × 256 pixels. A beam chopper combined with an RBS detector is used for beam dose normalization: it is positioned behind the collimating slits and in front of the scanning coils, cutting a fraction of the ion flux that is directed onto the sample [102]. In this way we ensure, the proportionality of the dose of backscattering ions from the chopper blades detected by a partially implanted passivated silicon (PIPS) detector and the primary ion dose deposited on the sample. A high-purity germanium X-ray detector is positioned at 135° with respect to the beam direction. It is used to register the concentrations and distribution of various metallic impurities in the samples through particle induced X-ray emission by ^{3}He ion beam (3HIXE) measurements.

To determine concentrations of marker elements and their depth profiles as well as to study a possible layered structure of the analysed samples, a PIPS-type RBS detector with a 300 µm thick depletion layer is positioned at 135°, covering a solid angle of 5.6 msrad. It is equipped with an 800 nm thick Al foil serving as a light block filter. For fuel retention and deposition investigations, an NRA detector was added to the standard detector configuration of the micro-beam end station (see Figure 5.1). For the detection of the fast protons from nuclear reaction, we used a PIPS detector with a 1000 µm thick depletion layer and an active area of 300 mm^2. This detector detector had a solid angle of 0.14 srad and was positioned at 135° scattering angle. To separate back-scattered primary ions from protons produced in nuclear reactions as well as to partly stop the protons and shield the detector against visible light, a combination of aluminium and kapton foil was inserted in front of the detector. The thickness of the foils depended on the energy of the products from the nuclear reaction.

We also used i-Ge detector for emitted x-rays or PIXE. The detector was positioned at 135° and shielded with 125 µm kapton foil, so that it was only sensitive for x-rays with $E > 2.5$ keV, used to detect small amounts of metal elements such as Fe and Ni. The amounts of these elements are negligible in comparison to other impurities. However, the large PIXE signal for W was useful in determining the position on the sample: also some surface topography could be deduced from PIXE 2D maps.

To quantify the amount of D, the D(^{3}He,p)α nuclear reaction was used [60]. The 3.3 MeV ^{3}He ion beam was used, focused down to 10×10 µm^2 in a high current mode of 300 pA. The NRA detector was shielded with 6 µm Al foil and 125 µm thick kapton foil. For measurements of ^{11}B and ^{15}N, which were quantified by the nuclear reactions ^{11}B(p, α)^{8}Be [103], [104] and ^{15}N(p,α)^{12}C [105], we used a focused proton beam at energies of 2.6 MeV and 1 MeV, respectively. Both beams were focused down to 1.5×1.5 µm^2 in the high current mode. For the quantification of the measurement data of ^{11}B and ^{15}N, we used the cross sections available for these two nuclear reactions and compared the simulated signals to the experimental ones obtained from the calibrated boron and nitrogen standards [103]–[105]. For B, an amorphous boron hydride (a-B:H, with B amount of 3×10^{18} cm^{-2} and H amount of $8\times^{17}$ cm^{-2}) was used as a standard while for the ^{15}N standard, a sample with 3×10^{16} cm^{-2} of ^{15}N implanted into W was used. For B and N measurements the NRA detector was only shielded with 3 µm thick Al foil.

5.1 Results of the Study

As stated in the section above the results of two studies are reported. In the first study the samples of fine grain graphite as a base were coated with 25 nm W. W was deposited on either polished or non-polished graphite substrate. The exact Ra value for these samples was not measured, but from a similar well-defined manufacturing process we can conclude that:

- polished graphite was similar to the Mo samples with $R_\mathrm{a} \approx 5$ nm.
- the unpolished graphite, similar to $R_\mathrm{a} \approx$ 1–2 µm samples.

As the argument runs that the polishing process was very similar to the ones for Mo samples, as graphite for samples was substrate was prepared at IPP, for both cases. The main difference was the cleaning procedure after polishing, by which graphite aggregates were removed from the surface in the case of Mo samples. For samples used for this study, these aggregates are clearly visible in Figure 5.2, marked with red circles. The polishing process of fine grain graphite partially fills the holes in the surface, discussed in the Mo sample preparation section, but some holes remain unfilled. These holes of few µm in size can, after cutting of graphite provide a measure of surface roughness. In Figure 5.2 the SEM secondary electron images of both surfaces are shown, polished and unpolished graphite coated with W, which can be compared with SEM images of Mo samples in Figure 3.13.

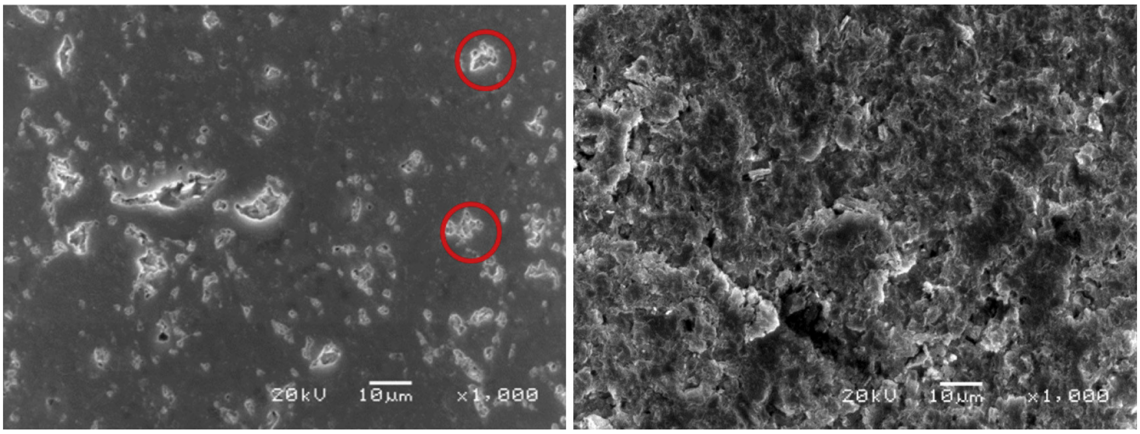

Figure 5.2: Images with secondary electrons from scanning electron microscope (SEM) of W coated graphite samples. On the left is the image of polished sample with W deposited on carbon aggregates, some marked with red circles as examples. On the right is an image of the surface of W deposited on unpolished graphite.

The main result of the study was the lateral distribution of W and D in the poloidal direction of AUG. The lateral profiles of W and D amounts are shown in Figure 5.3.

The analysis of one small tile from the vicinity of the strike point, does not provide data on the dynamics in the whole divertor region. However, two main conclusions about the effect of surface roughness can be made.

The first conclusion concerns the thickness of W layer. As evident from the data in Figure 5.3, the unpolished surface acts like deposition site for W, as a significant increase of W layer thickness was measured. Meanwhile the polished surface suffers a significant erosion. If we attribute the effect in the data only to erosion, there is less erosion on the

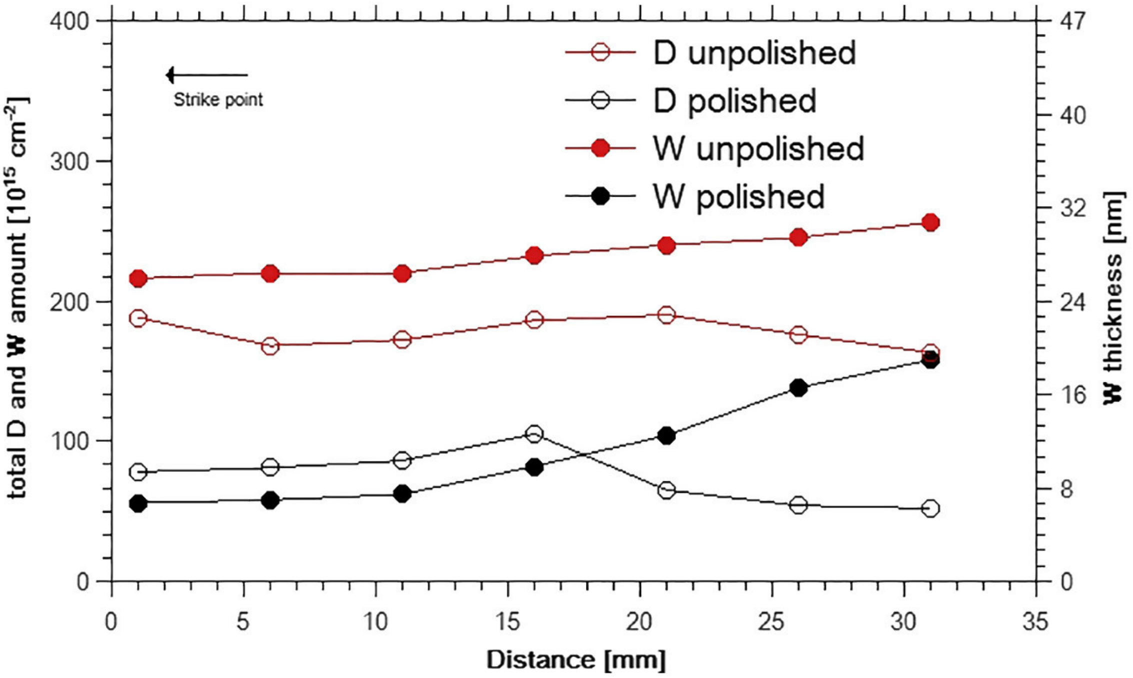

Figure 5.3: Lateral profile of total amounts of D and W plotted in poloidal direction of AUG.

rough surface than on the polished one, in a agreement with results presented in section 4.2.2.

The second conclusion is about the D retention in the samples. The measurements show that in unpolished samples we get roughly a factor of two more retained D, compared to the polished one.

In the second study nine samples from two sets were investigated. One set of six samples was exposed to L-mode D discharges and the other set of three samples was exposed to H-mode He discharges in AUG. Their detailed description is in Table 5.1 containing specific important parameters of each sample and surface roughness ranging from less than 100 nm up to more than 1 µm. For majority of the samples the preparation procedure was similar to that described previously.

The first batch of 6 samples was exposed to 5 L-mode discharges in D, the plasma was also seeded with ^{15}N gas. Samples were mounted on DIM-II manipulator tiles, as shown in Figure 5.4, where the positions of analysis on specific samples are marked. From the boronization process of AUG preparation we found trace amounts of B in the plasma chamber during the discharges, also deposited on the samples. All these elements can be measured with NRA, categorised as impurities in the wall material. In NRA analysis only isotopes can be detected, so the measurements were performed for D, ^{11}B and ^{15}N. The lateral profiles in the poloidal direction of the isotopes are present in Figures 5.5 and 5.6, respectively. As in the boronization of AUG the natural mixture of B isotopes is used, the total amount of B in the sample can be deduced from ^{11}B amount. It is shown in Figure 5.7.

D amounts, on average, to $80 - 90 \times 10^{15}$ cm^{-2} for milled graphite (M) samples, $30 - 40 \times 10^{15}$ cm^{-2} for polished (P) graphite samples and $10 - 15 \times 10^{15}$ cm^{-2} for W bulk sample. There is a clear trend of D retention to increase with increasing surface roughness. We also observed a small dependence of D retention on the analysing position, obtaining the largest retention on both sides (below and above) near the OSP, the location of highest

Sample	Composition	Surface roughness	Exposure in AUG mode and plasma	Seeding ^{15}N atoms
M 2/3	Milled graphite 100 nm of W	$\sim$ 1 μm	5 L-mode in D	5.3×10^{21}
P 2/3	Polished graphite 100 nm of W	$\sim$ 0.3 μm	5 L-mode in D	5.3×10^{21}
W 2/3	Bulk polished W	< 0.1 μm	5 L-mode in D	5.3×10^{21}
T#3	Bulk W, exposed to 1×10^{24} m^{-2} of 37 keV He atoms in GLADIS	> 1 μm	9 H-mode in H and He	Non seeded
M#2	Milled graphite 20 nm of W	~ 1 μm	9 H-mode in H and He	Non seeded
W#2	Bulk polished W	< 0.1 μm	9 H-mode in H and He	Non seeded

Table 5.1: Summary of sample types and exposures in AUG. The number of the sample name corresponds to the location on the AUG manipulator arm during the exposure, same as in Figure 3.33.

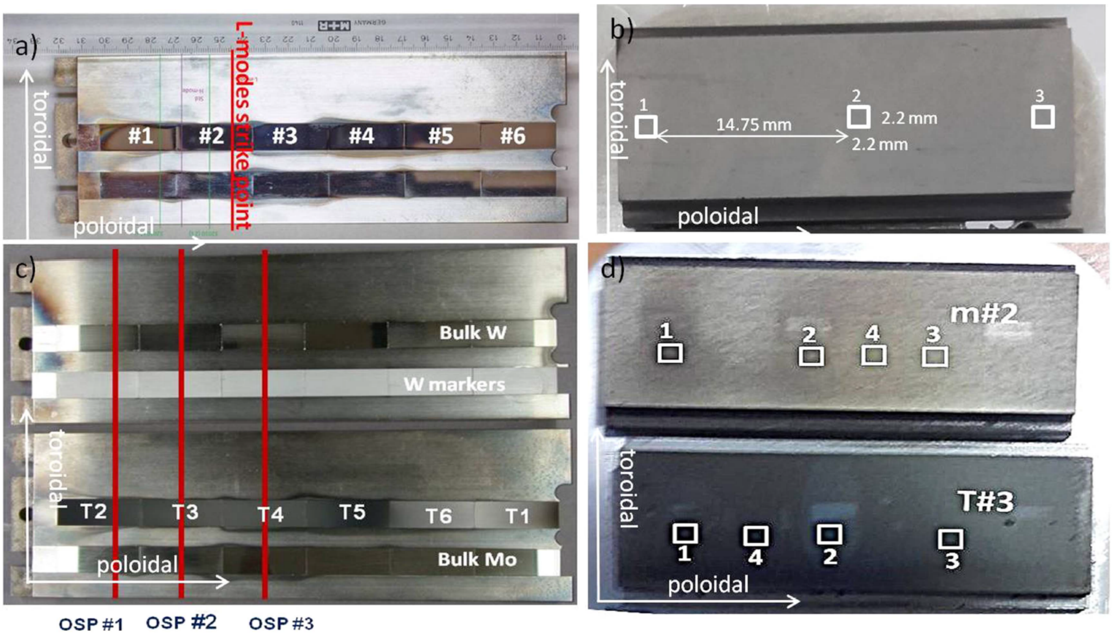

Figure 5.4: A photo of: a) the samples mounted on the divertor manipulator arm in the ^{15}N experiment in AUG. b) one of the exposed samples with marked regions (white rectangles) of the performed analysis using ion beam technique by microbeam. c) the samples mounted on the divertor manipulator arm in the He experiment in AUG. d) two of the exposed samples where the regions of analysis using microbeam technique are marked by white rectangles.

impinging ion and impurity flux. The B amount is between 20×10^{15} Bcm^{-2} and 30×10^{15} cm^{-2} for the three types of samples. As observed for the deuterium retention, the largest ^{15}N content is also obtained for the milled graphite sample. On bulk W samples the ^{15}N retention is the lowest, $3 - 7 \times 10^{15}$ cm^{-2}.

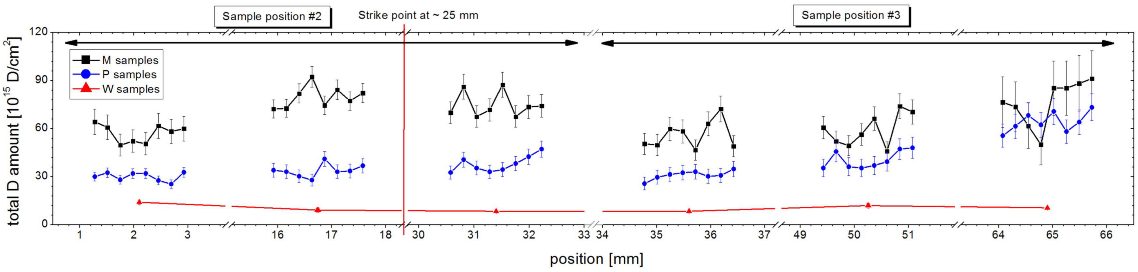

Figure 5.5: Lateral profiles of D amount in the poloidal direction of AUG.

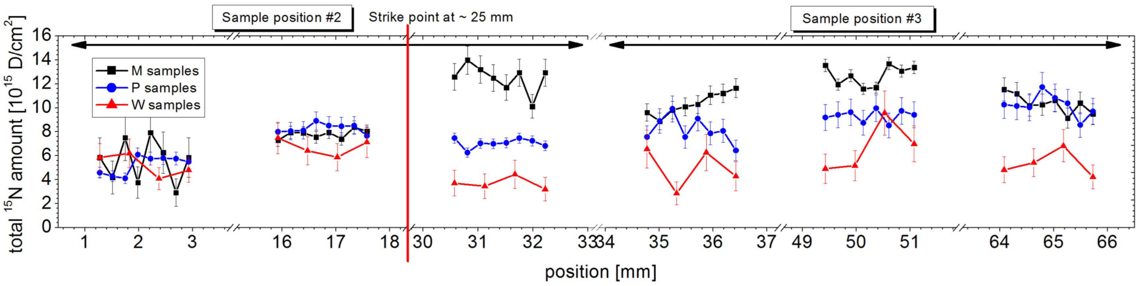

Figure 5.6: Lateral profile of ^{15}N amount in the poloidal direction of AUG.

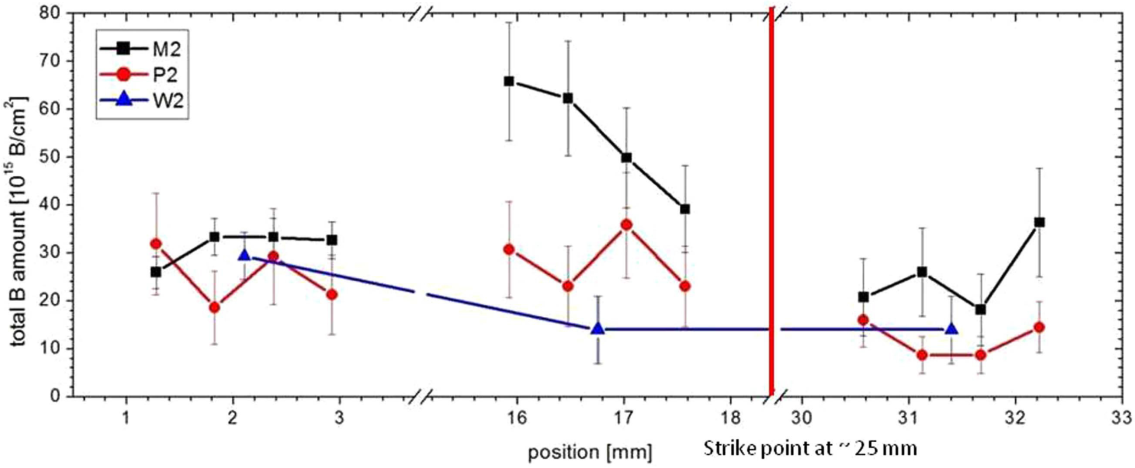

Figure 5.7: Lateral profile of B amount in the poloidal direction of AUG.

The presented data leads to the conclusion, that samples with the highest surface roughness M exhibit the highest retention of D, N and B, and polished tungsten W exhibits the lowest one. Although the direct comparison is not possible as one type of samples is the milled or polished graphite with W coating and the other one being bulk W. This is especially important for D retention. However, a similar behaviour can be observed for the other two elements, B and N.

Three samples from H-mode exposure were analysed in the second part of the study, two of them being bulk W samples. The surface of one was exposed to 37 keV ions in GLADIS [106], to create W fuzz [96], with the surface roughness exceeding 1 µm and its fuzzines is visible on the SEM image, shown in Figure 5.8. The other was polished W and the third was milled graphite with W coating. All the samples were then exposed to nine H-mode discharges in a mixture of H and He plasma. This meant that only B can be measured with applied NRA as an impurity. The results of the measurement are shown in Figure 5.9, where total B amount in the poloidal direction of AUG is plotted. From the data the effect of the surface roughness on B retention is recognized, with the retention for the fuzzy sample 10 times higher than for the polished W sample.

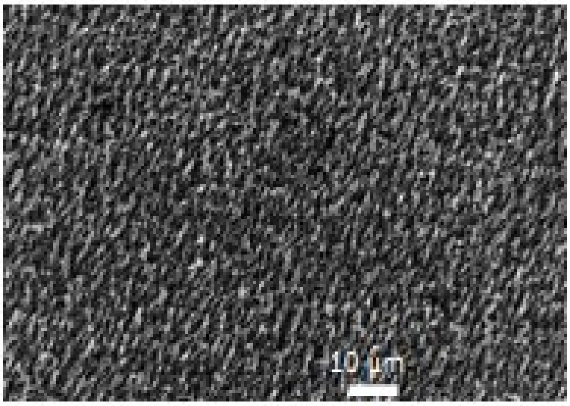

Figure 5.8: SEM image of T#3 sample fuzzy surface.

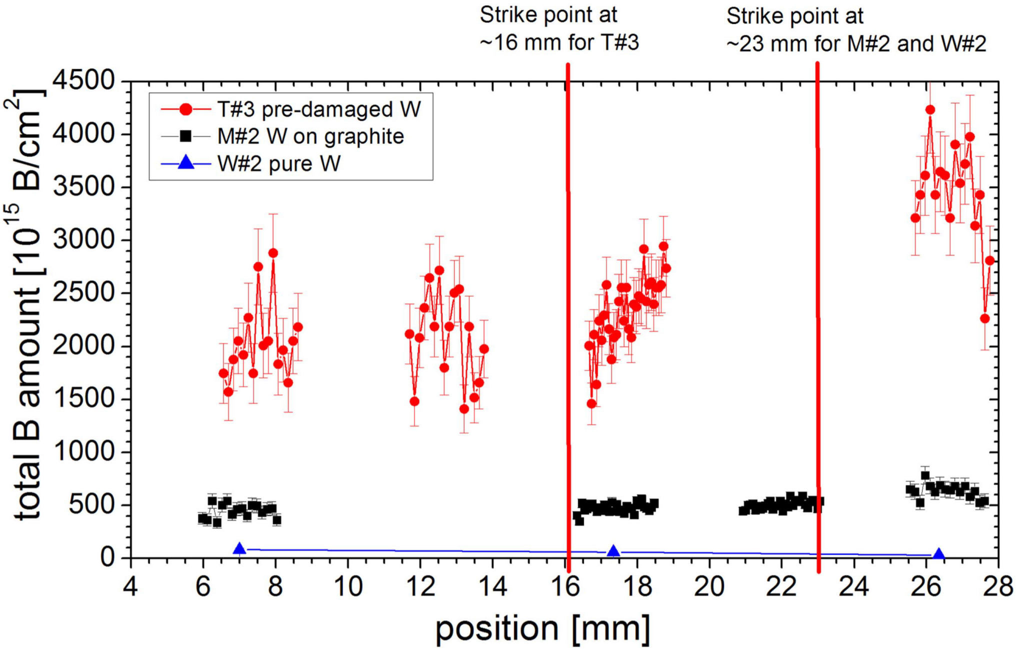

Figure 5.9: Lateral profile of total amount of B poloidal direction of AUG, for samples exposed in H-mode H/He plasma.

From the presented data we can conclude how the surface roughness affects the impurity retention in materials exposed in the divertor region of tokamak: the higher the surface roughness, the more retention is present. This is logical as the main retention takes place at the surfaces, and with increasing surface roughness there is more of effective surface to trap the impurities. However, with the increasing time of operation of the tokamak the diffusion process drives the impurities into the bulk of the material. The problem is the retention of hydrogen isotopes, seen as a fuel loss in the fuel inventory of the tokamak. A He retention, which we were unable to detect, is even more problematic as it forms bubbles in the material and thus affects its mechanical properties [107].

Chapter 6

Conclusions

In this work we presented an elaborate study of material sputtering process relevant for the fusion application. Sputtering inside the fusion reactors causes the erosion of first wall material, which contributes to shortening of the lifetime of the components. In the most promising concept of fusion reactors, for future power plants with tokamak geometry, the region with the most pronounced sputtering is the divertor. In there materials experience high particle flux up to 5×10^{23} m^{-2} s^{-1}, corresponding to thermal loads up to 20 MW/m^2. This leads to additional stress to the material. In addition to sputtering another important restriction of the components life time is accumulation of hydrogen isotopes in the bulk of the material, from the fuel in the fusion reactor.

Both processes have a long history of investigation, yet most of the investigations were performed with the laboratory-prepared surfaces with mirror-like polish. In the future application in the tokamak reactors production of large scale components with such surface finish will not be practical. Therefore, the need arose to study the effects of surface roughness on both processes. In this manner we present results of two complementary studies where surface roughness was the main parameter in the experiment. At first, we present detailed study of sputtering under the conditions similar to those in a tokamak and compare them to a real tokamak experiment. In the second, we investigated briefly the retention of impurities on the samples exposed to plasma in the tokamak. To obtain quantitative data on the samples various techniques were employed. For sample surface topography characterization, the scanning electron microscopy, atom force microscopy, and confocal laser scanning microscopy were used. The changes in sample composition were studied with the particle induced x-ray emission and a Nuclear reaction analysis. Moreover, the changes in coating thickness were measured with Rutherford backscattering spectroscopy.

First we take a short overview of the sputtering part of the work, divided into three work packages. In the first one we investigated the effect of the surface roughness on sputter yield, while in the second and the third packages we compared the results obtained from laboratory experiment with the results obtained in real size tokamak device and with computer simulations in SDTrimSP 6.0 software. The predictions were tested in ASDEX Upgrade tokamak - AUG, so the use of tungsten for erosion was not possible in view of W contamination from plasma chamber. Molybdenum was chosen as the surrogate material. Earlier studies show, that main contribution to erosion is from D ions in the keV energy range. After this conclusion the construction of Low Energy Ion Sputtering Apparatus - LEISA was undertaken, involving a vacuum chamber, electron cyclotron resonance ion gun and sample mounting stage. With LEISA we were able to expose samples to well defined and characterised 1 keV/D ions under arbitrary angles. The samples of various surface roughness were exposed at the angles of 0°, 40°, 60° and 70°. The samples were made from graphite substrate coated with roughly 115 nm of Mo, produced by pulsed laser deposition. The surface roughness of 5 nm, 110 nm, 280 nm and 2–3 µm were included and were exposed in LEISA to D ion fluencies ranging from 0.89 to 3.19×10^{23} 1/m^2. The obtained data reveal that there is a clear influence of the incidence angle and surface roughness on the sputter yield of Mo. On the polished surfaces sputter yield increases at higher impact angles, as predicted by theory. With increasing surface roughness, the sputter yield increases at 0° impact angle. For higher impact angle surfaces two different behaviours are observed: if the surface roughness is in the medium range (a few hundreds of nm), the dominant effect is that more and more surface is exposed at higher impact angles leading to correspondingly increasing sputter yield. However, for the very rough surfaces a decrease of the sputter yield at high impact angles was observed which we explained by redeposition and shadowing effects of the rough surface. In the presented cases, this decrease was only observed on surfaces with the highest surface roughness of 2–3 µm.

In parallel with the laboratory part of the study, samples of the same composition were exposed to plasma discharges in ASDEX Upgrade tokamak. Samples were mounted on DIM-II manipulator and exposed at outer strike point - OSP where the impact angle of the particles from plasma is around 60°. A similar effect of surface roughness on sputtering, as in the laboratory, was observed. We found a significant decrease of sputtering for highest surface roughness of 2–3 µm as compared to the the 5 nm. However, for samples of intermediate roughness a similar amount of sputtering was observed. Precise value of sputtering cannot be determined, due to the broad ion flux distribution in AUG, but qualitative results shows similar trends as in laboratory study.

In the third part of this work SDTRimSP in 1D and 3D was used, to calculate the sputter yield for Mo in the laboratory experiment. In general, the calculation with SDTrimSP-3D qualitatively produced good agreement with the measured angular and roughness dependence of the sputter yield. However, there are discrepancies between the absolute calculated values of sputter yield. A possible reason is the lack of necessary detail in surface reproduction which is accessible with current methods but is a necessary input for SDTrimSP-3D. For now, it is more advisable to take experimental data for plasma-facing components design works on surfaces as they more closely resemble the real components. Still, the obtained data serve as a valuable guideline for the design of plasma-facing component surfaces in tokamaks and for assessing their lifetime. Strictly from the erosion point of view, the components with high value of R_a will last longer than smooth ones. The SDTrimSP results together with the laboratory part of the study have already been published by Kelemen et al. [108].

To summarise the results of the sputtering studies, we can conclude that the angle of impact and surface roughness have profound effect on sputtering. The optimistic conclusion can be made for the future fusion reactors. There the impact angles are around 60° which means high erosion in the case of polished surfaces. A large scale production of mirror polished surfaces is not economical for large scale fusion devices, therefore it is expected that commercial components will have surface roughness in the ranges above $>$ 1 µm. For such surface roughness we have shown that sputtering is suppressed. The suppressed sputtering leads to less erosion of components and therefore to prolonging their lifetime.

On the surface of plasma facing components not only sputtering process can take place. The impurities, released from the surface, can contaminate the core plasma, contributing to less efficient operation of a reactor. The retention of hydrogen isotopes is also very important due to fuel cycle and safety restrictions as tritium is radioactive and therefore materials with retained tritium are treated as radioactive waste. To study the effect of surface roughness on the this process, impurity retention on samples with varying surface roughness exposed to different plasmas in the ASDEX Upgrade tokamak was examined.

Sample tiles exposed in the divertor region were investigated using ion beam analytical methods. Nuclear reaction analysis was used for measuring B, N and D, while trace contamination of elements like Fe and Ni, was done with particle induced x-ray emission. In general the results of the study show that with increased surface roughness the amount of retained impurities is increased. This can be easily explained by the fact that with large surface roughness the effective surface on which the impurities can be bound, is increased. The short conclusion is that contrary to sputtering process, the increased surface roughness is not beneficial regarding to the impurity retention.

At the beginning of this work we stated two hypotheses:

1. Well defined laboratory measurements can predict erosion behaviour of first wall materials inside of thermonuclear fusion reactors in tokamak configuration.
2. Ion beam analysis methods can provide useful information in post-mortem analysis of erosion in materials exposed to plasma in tokamak reactors.

This was the drive in the design of experiment and provided rough guidelines for the proceeding work. The first hypothesis was confirmed in entirety, as we have shown an excellent agreement between laboratory results and experiments performed in tokamak, not only for Mo targets, but the same behaviour was observed also in the targets not primarily designed for the erosion studies, like the W tiles in AUG. With combination of improved algorithms for calculating the sputtering in the SDTrimSP software, we show how the realistic targets can be included in tokamak behaviour modelling by preparation of more realistic sputtering input parameters for more complex models.

Ion beam methods have been extensively used for confirming the first hypothesis. Moreover, during the analysis of samples exposed in tokamak we extended the use of ion beam techniques. Thus we obtained additional information on the effect of surface roughness not only to erosion, but also to the impurity retention. With this we recommend ion beam techniques as a powerful tool in post-mortem analysis of materials exposed in tokamaks. However, as shown in the case of erosion study of Mo layers in AUG we had some difficulties in quantification of the measurements. Nevertheless, we still can regard the second hypothesis as confirmed. However, there is a need for the development of data analysis procedures for rough surfaces.

Appendix A

SDTrimSP Calculation Input File tri.inp

The copy of tri.inp file that was used in SDTrimSP 1D calculation of sputter yield. Comments of specific input lines are written after %, to be easily distinguished from the input code. The input file is divided in five blocs, which are separated with text line for easy identification. Each block is used for a specific purpose as follows:

1. The first block is used to specify the chemical elements used in the calculation.
2. The second block is used to run the angle variation routine automatically .
3. The third we specify the characteristic of the ion beam used.
4. Fourth block is important for the efficiency of calculation and describes the numerical methods part of simulation.
5. In the last or fifth block we specify the target parameter.

For detailed description of all the options on specific function is best to look into SDTrimSP manual [79].

```
   D −> Mo
&TRI_INP
text=’--elemements--’
ncp = 2 % number of elements in the calculation
symbol = "D", "Mo" % elements used in calculation


   text=’--beam--serie’
number_calc = 19 % number of angular slices in batch calculations


   text=’--beam--’
case_e0 = 0 % fixed energy of projectile
e0 = 1000, 0.00 , % ion beam energy in eV
qubeam = 1.000, 0.000, % definition which element is beam
case_alpha = 5 % routine that makes variation of angle in calculations
alpha0 = 0.00, 0.00 % angle of incidence, angle of tilted target
```

```
   text='--control--'
flc = 1 % fluence *10^6 ions
nh = 100 % number of histories
nr_pproj = 10000 % number of projectiles between two target updates
idout = 100 % write outputs at the end and in the middle of calculation
idrel = 1 % static type of calculation
ipot = 1 % interaction potential 1=KrC
iintegral = 2 % integration method 2=Gauss-Legendre
ipivot=8 % number of pivots


   text='--target--'
ttemp = 293.15 % temperature of target in K
ttarget = 5000 % target thickness in Å
nqx = 500, % number of layers in the target
isbv = 1 % surface binding model
inel0 = 4 ,1 % inelastic loss model
qu = 0.0 , 1.0, % homogeneity of the target
e_cutoff = 1.0, 1.0, % cut-off energy of recoils/ions when stop calculating
e_surfb = 1.1000 , 8.45 % surface binding energy
qu_int= .true.  % linear interpolation of atomic fractions between the depth
intervals
irc0 = 1 % bounding of subthreshold recoils atom
/
```

References

[1] A. Eddington, “On the radiative equilibrium of the stars,” *Monthly Notices of the Royal Astronomical Society*, vol. 77, pp. 16–35, 1916.

[2] A. Eddington, “The Internal Constitution of the Stars,” *Science*, vol. 52, pp. 233–240, 1920.

[3] M. Salaris and S. Cassisi, *Evolution of stars and stellar populations.* John Wiley & Sons, 2005.

[4] “Proton-proton fusion.” (2022), [Online]. Available: `https://en.wikipedia.org/wiki/File:Fusion_in_the_Sun.svg` (visited on 05/05/2022).

[5] W. M. Stacey, *Fusion: An introduction to the physics and technology of magnetic confinement fusion.* John Wiley & Sons, 2010.

[6] D. Petkow, G. Herdrich, and H.-P. Laufer R. andRoser, “Key Technologies for Fusion-based Space Propulsion: A Case Study,” 2007.

[7] “D-T fusion.” (2022), [Online]. Available: `https://en.wikipedia.org/wiki/Fusion%5C_power%5C#/media/File:Deuterium-tritium%5C_fusion.svg` (visited on 05/05/2022).

[8] “ITER.” (2022), [Online]. Available: `https://www.iter.org/` (visited on 07/10/2022).

[9] “Tokamak.” (2022), [Online]. Available: `https://en.wikipedia.org/wiki/Tokamak` (visited on 07/07/2022).

[10] D. R. Nicholson and D. R. Nicholson, *Introduction to plasma theory.* Wiley New York, 1983, vol. 582.

[11] “W7X.” (2022), [Online]. Available: `https://www.ipp.mpg.de/w7x` (visited on 05/07/2022).

[12] “Tokamak.” (2023), [Online]. Available: `https://www.ipp.mpg.de/14869/tokamak` (visited on 04/28/2023).

[13] “AUG.” (2022), [Online]. Available: `https://www.ipp.mpg.de/16195/asdex` (visited on 01/08/2022).

[14] R. Tivey, T. Ando, A. Antipenkov, *et al.*, “ITER divertor, design issues and research and development,” *Fusion engineering and design*, vol. 46, no. 2-4, pp. 207–220, 1999.

[15] G. Federici, W. Biel, M. Gilbert, R. Kemp, N. Taylor, and R. Wenninger, “European DEMO design strategy and consequences for materials,” *Nuclear Fusion*, vol. 57, no. 9, p. 092 002, 2017.

[16] R. Pitts, X. Bonnin, F. Escourbiac, *et al.*, “Physics basis for the first ITER tungsten divertor,” *Nuclear Materials and Energy*, vol. 20, p. 100 696, 2019.

[17] S. Brezinsek, J. Coenen, T. Schwarz-Selinger, *et al.*, “Plasma–wall interaction studies within the EUROfusion consortium: Progress on plasma-facing components development and qualification,” *Nuclear fusion*, vol. 57, no. 11, p. 116 041, 2017.

[18] M. Rubel, “Fusion neutrons: Tritium breeding and impact on wall materials and components of diagnostic systems,” *Journal of Fusion Energy*, vol. 38, no. 3, pp. 315–329, 2019.

[19] R. Behrisch and W. Eckstein, *Sputtering by particle bombardment: experiments and computer calculations from threshold to MeV energies.* Springer Science & Business Media, 2007, vol. 110.

[20] M. Keilhacker, A. Team, *et al.*, “The ASDEX divertor tokamak,” *Nuclear fusion*, vol. 25, no. 9, p. 1045, 1985.

[21] A. Herrmann, I. Zammuto, M. Balden, *et al.*, “Experiences with a solid tungsten divertor in ASDEX Upgrade,” *Nuclear Materials and Energy*, vol. 12, pp. 205–209, 2017.

[22] “AUG tehnical data.” (2022), [Online]. Available: `https://www.ipp.mpg.de/16208/einfuehrung` (visited on 01/08/2022).

[23] A. Herrmann, N. Jaksic, P. Leitenstern, *et al.*, “A large divertor manipulator for ASDEX Upgrade,” *Fusion Engineering and Design*, vol. 98, pp. 1496–1499, 2015.

[24] P. Sigmund, “Theory of sputtering. I. Sputtering yield of amorphous and polycrystalline targets,” *Physical review*, vol. 184, no. 2, p. 383, 1969.

[25] P. Sigmund, “Sputtering by ion bombardment theoretical concepts,” *Sputtering by particle bombardment I*, pp. 9–71, 1981.

[26] H. H. Andersen and L. Bay, *Sputtering by Particle Bombardment I, Top. Appl. Phys. 47.* Springer, 1981.

[27] W. Möller, “Fundamentals of ion-solid interaction. A compact introduction,” Helmholtz-Zentrum Dresden-Rossendorf eV, Tech. Rep., 2017.

[28] “The stopping and range of ions in matter-SRIM.” (2011), [Online]. Available: `http://www.%20srim.%20org` (visited on 02/11/2018).

[29] U. Von Toussaint, A. Mutzke, and A. Manhard, “Sputtering of rough surfaces: A 3D simulation study,” *Physica Scripta*, vol. 2017, no. T170, p. 014 056, 2017.

[30] Y. Wang and M. Nastasi, “Handbook of modern ion beam materials analysis,” *MRS BULLETIN*, vol. 36, 2011.

[31] J. F. Ziegler, *Ion implantation science and technology.* Elsevier, 2012.

[32] S. Sze, *VLSI technology.* McGraw-Hill, 1983.

[33] J. Biersack and W. Eckstein, “Sputtering studies with the Monte Carlo program TRIM. SP,” *Applied Physics A*, vol. 34, no. 2, pp. 73–94, 1984.

[34] W. Eckstein and R. Preuss, “New fit formulae for the sputtering yield,” *Journal of Nuclear Materials*, vol. 320, no. 3, pp. 209–213, 2003.

[35] E. G. Hatam, P. Pelicon, M. Lamehi-Rachti, *et al.*, “Surface topography reconstruction by stereo-PIXE,” *Journal of Analytical Atomic Spectrometry*, vol. 27, no. 5, pp. 834–840, 2012.

[36] D. Rugar and P. Hansma, “Atomic force microscopy,” *Physics today*, vol. 43, no. 10, pp. 23–30, 1990.

[37] M. Küstner, W. Eckstein, E. Hechtl, and J. Roth, “Angular dependence of the sputtering yield of rough beryllium surfaces,” *Journal of nuclear materials*, vol. 265, no. 1-2, pp. 22–27, 1999.

[38] W. Eckstein, *Computer simulation of ion-solid interactions.* Springer Science & Business Media, 2013, vol. 10.

[39] E. Gibney, “Fuel for world’s largest fusion reactor ITER is set for test run.,” *Nature*, vol. 591, pp. 15–16, 2021.

[40] R. Chodura, “Numerical analysis of plasma-wall interaction for an oblique magnetic field,” *Journal of Nuclear Materials*, vol. 111, pp. 420–423, 1982.

[41] “POLIMI.” (2022), [Online]. Available: `https://www.polimi.it/en` (visited on 10/05/2022).

[42] S. Markelj, T. Schwarz-Selinger, M. Pečovnik, *et al.*, “Displacement damage stabilization by hydrogen presence under simultaneous W ion damage and D ion exposure,” *Nuclear Fusion*, vol. 59, no. 8, p. 086 050, 2019.

[43] Ž. Šmit, *Spektroskopske metode s pospešenimi ioni.* DMFA-založništvo, 2003.

[44] W. R. Leo, *Techniques for nuclear and particle physics experiments: a how-to approach.* Springer Science & Business Media, 2012.

[45] M. Mayer, “Rutherford backscattering spectrometry (RBS),” in *Workshop on Nuclear Data for Science and Technology: Materials Analysis*, vol. 34, Abdus Salam International Centre for Theoretical Physics, 2003.

[46] M. Nastasi and T. J. R., “Handbook of modern ion beam materials analysis,” *Materials Research Society, Pittsburgh, Pa*, 1995.

[47] J. L’Ecuyer, J. Davies, and N. Matsunami, “How accurate are absolute rutherford backscattering yields,” *Nuclear Instruments and Methods*, vol. 160, no. 2, pp. 337–346, 1979, ISSN: 0029-554X.

[48] H. H. Andersen, F. Besenbacher, P. Loftager, and W. Möller, “Large-angle scattering of light ions in the weakly screened Rutherford region,” *Phys. Rev. A*, vol. 21, pp. 1891–1901, 6 Jun. 1980.

[49] “IBANDL Ion Beam Analysis Nuclear Data Library.” (2022), [Online]. Available: `https://www-nds.iaea.org` (visited on 01/11/2022).

[50] M. Bozoian, K. M. Hubbard, and M. Nastasi, “Deviations from Rutherford-scattering cross sections,” *Nuclear Instruments and Methods in Physics Research Section B: Beam Interactions with Materials and Atoms*, vol. 51, no. 4, pp. 311–319, 1990, ISSN: 0168-583X.

[51] M. Bozoian, “Deviations from Rutherford backscattering for Z = 1, 2 projectiles,” *Nuclear Instruments and Methods in Physics Research Section B: Beam Interactions with Materials and Atoms*, vol. 58, no. 2, pp. 127–131, 1991, ISSN: 0168-583X.

[52] M. Bozoian, “A useful formula for departures from Rutherford backscattering,” *Nuclear Instruments and Methods in Physics Research Section B: Beam Interactions with Materials and Atoms*, vol. 82, no. 4, pp. 602–603, 1993, ISSN: 0168-583X.

[53] M. Mayer. “SIMNRA.” (2019), [Online]. Available: `https://www.ipp.mpg.de/17301/garching` (visited on 05/10/2019).

[54] T. Calligaro, J.-C. Dran, and J. Salomon, “Ion beam microanalysis,” in *Comprehensive Analytical Chemistry*, vol. 42, Elsevier, 2004, pp. 227–276.

[55] F. H. Attix, *Introduction to radiological physics and radiation dosimetry.* John Wiley & Sons, 2008.

[56] G. F. Knoll, *Radiation detection and measurement.* John Wiley & Sons, 2010.

[57] J. Campbell, D. Cureatz, E. Flannigan, *et al.*, "The Guelph PIXE Software Package V," *Nuclear Instruments and Methods in Physics Research Section B: Beam Interactions with Materials and Atoms*, vol. 499, pp. 77–88, 2021. [Online]. Available: `https://www.sciencedirect.com/science/article/pii/S0168583X21001646`.

[58] J. Maxwell, W. Teesdale, and J. Campbell, "The Guelph Pixe software package II," *Nuclear Instruments and Methods in Physics Research Section B: Beam Interactions with Materials and Atoms*, vol. 95, no. 3, pp. 407–421, 1995.

[59] C. Ryan, J. Laird, L. Fisher, R. Kirkham, and G. Moorhead, "Improved Dynamic Analysis method for quantitative PIXE and SXRF element imaging of complex materials," *Nuclear Instruments and Methods in Physics Research Section B: Beam Interactions with Materials and Atoms*, vol. 363, pp. 42–47, 2015.

[60] V. K. Alimov, M. Mayer, and J. Roth, "Differential cross-section of the D (3He, p) 4He nuclear reaction and depth profiling of deuterium up to large depths," *Nuclear Instruments and Methods in Physics Research Section B: Beam Interactions with Materials and Atoms*, vol. 234, no. 3, pp. 169–175, 2005.

[61] M. Mayer, E. Gauthier, K. Sugiyama, and U. Von Toussaint, "Quantitative depth profiling of deuterium up to very large depths," *Nuclear Instruments and Methods in Physics Research Section B: Beam Interactions with Materials and Atoms*, vol. 267, no. 3, pp. 506–512, 2009.

[62] M. Mihovilovič, "Določanje globinske porazdelitve devterija z jedrsko reakcijo D(^3He, p)α," University Ljubljana, Seminar, 2008.

[63] W. Möller and F. Besenbacher, "A note on the 3He+ D nuclear-reaction cross section," *Nuclear Instruments and methods*, vol. 168, no. 1-3, pp. 111–114, 1980.

[64] B. Wielunska, M. Mayer, T. Schwarz-Selinger, U. Von Toussaint, and J. Bauer, "Cross section data for the D (3He, p) 4He nuclear reaction from 0.25 to 6 MeV," *Nuclear Instruments and Methods in Physics Research Section B: Beam Interactions with Materials and Atoms*, vol. 371, pp. 41–45, 2016.

[65] "IPP." (2022), [Online]. Available: `https://www.ipp.mpg.de/17301/garching` (visited on 10/05/2022).

[66] "ISTP." (2022), [Online]. Available: `https://www.cnr.it/en/institute/126` (visited on 10/05/2022).

[67] E. Vassallo, M. Pedroni, S. M. Pietralunga, *et al.*, "Black-silicon production process by CF4/H2 plasma," *Thin Solid Films*, vol. 603, pp. 173–179, 2016.

[68] A. Maffini, A. Pazzaglia, D. Dellasega, V. Russo, and M. Passoni, "Growth dynamics of pulsed laser deposited nanofoams," *Phys. Rev. Mater.*, vol. 3, p. 083 404, 8 Aug. 2019.

[69] K. Vernon-Parry, "Scanning electron microscopy: An introduction," *III-Vs Review*, vol. 13, no. 4, pp. 40–44, 2000.

[70] S. Markelj, T. Schwarz-Selinger, A. Založnik, *et al.*, "Deuterium retention in tungsten simultaneously damaged by high energy W ions and loaded by D atoms," *Nuclear Materials and Energy*, vol. 12, pp. 169–174, 2017.

[71] "Pfeifer turbo pump." (2022), [Online]. Available: `https://www.idealvac.com/files/manualsII/Operating%5C_Instructions%5C_TMH%5C_TMU%5C_521P.pdf` (visited on 01/11/2022).

[72] "Kashiyama pump." (2022), [Online]. Available: `https://synsysco.com/products/dry-vacuum-pumps/air-cooled-inert-gas/kashiyama-neodry-multilobe-dry-pumps/kashiyama-neodry-15e-multilobe-dry-vacuum-pump` (visited on 01/11/2022).

[73] "Tectra." (2022), [Online]. Available: `https://tectra.de/` (visited on 05/11/2022).

[74] "Keithley 2000 multimether." (2022), [Online]. Available: `https://download.tek.com/datasheet/2000-DMM-Data-Sheet-1KW612970.pdf` (visited on 10/11/2022).

[75] "LabView." (2022), [Online]. Available: `https://www.ni.com/sl-si/shop/labview.html` (visited on 11/15/2022).

[76] "Ionetch." (2022), [Online]. Available: `https://tectra.de/wp-content/uploads/2017/03/IonEtch.pdf` (visited on 05/26/2022).

[77] I. Bizyukov and K. Krieger, "Dual beam experiment for simultaneous irradiation of surfaces with ion species of gaseous and solid-state elements," *Review of scientific instruments*, vol. 77, no. 4, p. 043 501, 2006.

[78] F. Hitzler, "Radiative Cooling of the Divertor Plasma with Argon and Nitrogen Seeding in the ASDEX Upgrade Tokamak," Ph.D. dissertation, Technische Universität Münche, Mnax-Planck-Institut für Plasmaphysik, München, Germany, 2020.

[79] A. Mutzke, R. Schneider, W. Eckstein, *et al.*, "SDTrimSP Version 6.00," 2019.

[80] J. Biersack and W. Eckstein, "Sputtering studies with the Monte Carlo program TRIM. SP," *Applied Physics A*, vol. 34, no. 2, pp. 73–94, 1984.

[81] W. Möller, W. Eckstein, and J. Biersack, "Tridyn-binary collision simulation of atomic collisions and dynamic composition changes in solids," *Computer Physics Communications*, vol. 51, no. 3, pp. 355–368, 1988.

[82] W. Möller and W. Eckstein, "Tridyn—A TRIM simulation code including dynamic composition changes," *Nuclear Instruments and Methods in Physics Research Section B: Beam Interactions with Materials and Atoms*, vol. 2, no. 1-3, pp. 814–818, 1984.

[83] A. Mutzke, R. Schneider, and G. Bandelow, "SDTrimSP-2D: Simulation of Particles Bombarding on a Two Dimensional Target-Version 2.0," 2013.

[84] R. Arredondo, M. Oberkofler, T. Schwarz-Selinger, *et al.*, "Angle-dependent sputter yield measurements of kev D ions on W and Fe and comparison with SDTrimSP and SDTrimSP-3D," *Nuclear Materials and Energy*, vol. 18, pp. 72–76, 2019.

[85] R. Stadlmayr, P. Szabo, B. Berger, *et al.*, "Fluence dependent changes of surface morphology and sputtering yield of iron: Comparison of experiments with SDTrimSP-2D," *Nuclear Instruments and Methods in Physics Research Section B: Beam Interactions with Materials and Atoms*, vol. 430, pp. 42–46, 2018.

[86] B. M. Berger, R. Stadlmayr, D. Bloech, *et al.*, "Erosion of Fe-W model system under normal and oblige D ion irradiation," *Nuclear Materials and Energy*, vol. 12, pp. 468–471, 2017.

[87] M. Mayer, "Improved physics in SIMNRA 7," *Nuclear Instruments and Methods in Physics Research Section B: Beam Interactions with Materials and Atoms*, vol. 332, pp. 176–180, 2014.

[88] M. Mayer, “Ion beam analysis of rough thin films,” *Nuclear Instruments and Methods in Physics Research Section B: Beam Interactions with Materials and Atoms*, vol. 194, no. 2, pp. 177–186, 2002.

[89] T. Schwarz-Selinger, “Deuterium retention in MeV self-implanted tungsten: Influence of damaging dose rate,” *Nuclear Materials and Energy*, vol. 12, pp. 683–688, 2017.

[90] W. Wilson, L. Haggmark, and J. Biersack, “Calculations of nuclear stopping, ranges, and straggling in the low-energy region,” *Physical Review B*, vol. 15, no. 5, p. 2458, 1977.

[91] “HP EliteBook 820.” (2022), [Online]. Available: `https://support.hp.com/ie-en/document/c03955656` (visited on 11/26/2022).

[92] W. Eckstein, C. Garcia-Rosales, J. Roth, and W. Ottenberger, “Sputtering data,” 1993.

[93] J. Roth, J. Bohdansky, and W. Ottenberger, “Data on Low-Energy Light Ion Sputtering. IPP report 9/26,” 1979.

[94] S. W. Paddock, “Confocal laser scanning microscopy,” *Biotechniques*, vol. 27, no. 5, pp. 992–1004, 1999.

[95] M. Kelemen, A. Založnik, P. Vavpetič, *et al.*, “Micro-NRA and micro-3HIXE with 3He microbeam on samples exposed in ASDEX Upgrade and Pilot-PSI machines,” *Nuclear Instruments and Methods in Physics Research Section B: Beam Interactions with Materials and Atoms*, vol. 404, pp. 179–184, 2017.

[96] M. Kelemen, A. Založnik, P. Vavpetič, *et al.*, “Study of lateral distribution of impurities on samples exposed in the ASDEX Upgrade using microbeam of 3He and 1H,” *Physica Scripta*, vol. 2017, no. T170, p. 014 067, 2017.

[97] P. Pelicon, P. Vavpetič, N. Grlj, *et al.*, “Fuel retention study in fusion reactor walls by micro-NRA deuterium mapping,” *Nuclear Instruments and Methods in Physics Research Section B: Beam Interactions with Materials and Atoms*, vol. 269, no. 20, pp. 2317–2321, 2011.

[98] “Oxford Microbeams lenses.” (2022), [Online]. Available: `http://www.microbeams.co.uk/Products.html%5C#om150` (visited on 11/18/2022).

[99] P. Pelicon, N. C. Podaru, P. Vavpetič, *et al.*, “A high brightness proton injector for the Tandetron accelerator at Jožef Stefan Institute,” *Nuclear Instruments and Methods in Physics Research Section B: Beam Interactions with Materials and Atoms*, vol. 332, pp. 229–233, 2014.

[100] P. Vavpetič, M. Kelemen, B. Jenčič, and P. Pelicon, “Nuclear microprobe performance in high-current proton beam mode for micro-PIXE,” *Nuclear Instruments and Methods in Physics Research Section B: Beam Interactions with Materials and Atoms*, vol. 404, pp. 69–73, 2017.

[101] Y. Suzaki and A. Tachibana, “Measurement of the μm sized radius of gaussian laser beam using the scanning knife-edge,” *Applied optics*, vol. 14, no. 12, pp. 2809–2810, 1975.

[102] K. Vogel-Mikuš, P. Pelicon, P. Vavpetič, I. Kreft, and M. Regvar, “Elemental analysis of edible grains by micro-PIXE: Common buckwheat case study,” *Nuclear Instruments and Methods in Physics Research Section B: Beam Interactions with Materials and Atoms*, vol. 267, no. 17, pp. 2884–2889, 2009.

[103] M. Mayer, A. Annen, W. Jacob, and S. Grigull, "The 11B (p, α0) 8Be nuclear reaction and 11B (p, p) 11B backscattering cross sections for analytical purposes," *Nuclear Instruments and Methods in Physics Research Section B: Beam Interactions with Materials and Atoms*, vol. 143, no. 3, pp. 244–252, 1998.

[104] G. Korschinek, A. Bergmaier, T. Faestermann, *et al.*, "A new value for the half-life of 10be by heavy-ion elastic recoil detection and liquid scintillation counting," *Nuclear Instruments and Methods in Physics Research Section B: Beam Interactions with Materials and Atoms*, vol. 268, no. 2, pp. 187–191, 2010.

[105] F. B. Hagedorn and J. B. Marion, "Further investigation of $\mathrm{N}^{15}+p$ Reactions," *Phys. Rev.*, vol. 108, pp. 1015–1019, 4 Nov. 1957.

[106] H. Greuner, H. Bolt, B. Böswirth, *et al.*, "Design, performance and construction of a 2 MW ion beam test facility for plasma facing components," *Fusion engineering and design*, vol. 75, pp. 345–350, 2005.

[107] A. Šestan, L. Sreekala, S. Markelj, *et al.*, "Non-uniform He bubble formation in W/W2C composite: Experimental and ab-initio study," *Acta Materialia*, vol. 226, p. 117 608, 2022.

[108] M. Kelemen, T. Schwarz-Selinger, A. Mutzke, *et al.*, "Influence of surface roughness on the sputter yield of Mo under keV D ion irradiation," *Journal of Nuclear Materials*, vol. 555, p. 153 135, 2021.

Bibliography

Publications Related to the Thesis

M. Kelemen, T. Schwarz-Selinger, A. Mutzke, M. Balden, E. Vassalo, M. Pedroni, D. Dellasega, M. Passoni, F. Romeo, A. Hakola, P. Pelicon, R. Zaplotnik and S. Markelj, "Influence of surface roughness on the sputter yield of Mo under keV D ion irradiation", *Journal of Nuclear Materials*, vol. 555, p. 153 135, 2021

M. Kelemen, A. Založnik, P. Vavpetič, M. Pečovnik, P. Pelicon, A. Hakola, A. Lahtinen, J. Karhunen, K. Piip, P. Paris, M. Laan, K. Krieger, M. Oberkofler, ASDEX Upgrade team, H. Van der Meiden and S. Markelj, "Micro-NRA and micro-3HIXE with 3He microbeam on samples exposed in ASDEX Upgrade and Pilot-PSI machines", *Nuclear Instruments and Methods in Physics Research Section B: Beam Interactions with Materials and Atoms*, vol. 404, pp. 179-184, 2017.

M. Kelemen, A. Založnik, P. Vavpetič, P. Pelicon, A. Hakola, G. Meisl, M. Oberkofler, K. Krieger, S. Brezinsek, S. Markelj, the ASDEX Upgrade Team and EUROfusion MST1 Team, "Study of lateral distribution of impuritieson samples exposed in the ASDEX Upgrade using microbeam of 3He and 1H", *Physica Scripta*, vol. 2017, no. T170, p. 014 067, 2017.

Biography

The author of this thesis Mitja Kelemen was born on 28 September 1988 in Murska Sobota. He studied Physics at Faculty for Mathematics and Physics, University of Ljubljana. There he completed his Bachelor degree in 2012 and continued studies on Masters level. He obtained his Master's degree on 19 December 2014 by defending his masters thesis titled "Influence of high energy ion implantation on the magnetic properties of carbon." In 2015 he started to work as associate at Department of Low and Medium energy physics at Jožef Stefan Institute. Same year he also enrolled into PhD program Ecotechnologies at the Jožef Stefan international postgraduate school. He is an author or co-author of more than 40 original scientific papers which include use of Ion beam analytical (IBA) methods. The areas of IBA application ranges from plant philology, fusion, material science, protein science and medicine.